Politecnico di Torino | ScuDo
Scuola di Dottorato ~ Doctoral School
WHAT YOU ARE, TAKES YOU FAR

Doctoral Dissertation

Doctoral Program in Energy Engineering (36^{th}cycle)

Transmission of respiratory droplets in ventilated indoor environments using the Eulerian approach

By

Yi Feng
******

Supervisor(s):
Prof. Antonio Buffo, Supervisor
Prof. Gianluca Boccardo, Co-Supervisor

Doctoral Examination Committee:
Prof. Giorgio Besagni , Referee, Politecnico di Milano
Prof. Francesco Maluta, Referee, Università di Bologna
Prof. Alfredo Soldati, Technische Universität Wien
Prof. Ada Ferri, Politecnico di Torino
Prof. Luigi Manna, Politecnico di Torino

Politecnico di Torino
2024

Declaration

I hereby declare that, the contents and organization of this dissertation constitute my own original work and does not compromise in any way the rights of third parties, including those relating to the security of personal data.

<div align="right">

Yi Feng

2024

</div>

I would like to dedicate this thesis to my loving parents

Acknowledgements

There will be a long list to express my deepest gratitude because I accept so much help and kindness.

First of all, I am profoundly thankful to my supervisors, Prof. Antonio Buffo, Prof. Gianluca Boccardo, Prof. Marco Vanni, and Prof. Daniele Marchisio for their supervision throughout my research. They have profound expertise, leading me to the interesting and challenging field of multiphase flows and giving me insightful suggestions during my research. They have great patience to guide me to do research and write papers step by step. They constantly encourage me for my work, presentation, and paper, which builds my confidence to be a researcher. Their genuine care and concern make me feel warm when far away from home. Additionally, I would also like to extend my gratitude to Dr. Dongyue Li. He has extensive experience and is always so warm to help me during my research.

Secondly, I would like to express my great appreciation to our research group, which is such a warm family. The members, Francesco Maniscalco, Antonello Raponi, Andrea Querio, Mohsen Shiea, Alessio Lombardo Pontillo, Francesco De Roma, Nunzia Lauriello, Lorenzo Vasquez Giuliano, Agnese Marcato, and those not named, are always so kind and warmhearted to help me solve problems in study and life. I will always be grateful for the happy memories we have in daily life, in parties, and in interesting activities.

Thirdly, I would like to thank the Politecnico di Torino for providing an excellent platform and a scholarship to support my study. Moreover, I would like to express my acknowledgment to hpc@polito for providing the computational resources:

Finally, I would like to express my deepest thanks to my parents. I am really sorry that I left them and went abroad for my PhD in that hard time. They hid their worries and tried their best to support me. I owe a thousand of gratitude to them.

The past three years are hard due to the COVID-19 pandemic. I hope this work may be a little bit helpful in facing possible similar challenges in the future. However, I hope even more that this work will be useless because there will be no such thing anymore in the future.

Abstract

Infectious diseases, such as COVID-19, can be transmitted by the virus-laden respiratory droplets exhaled by an infected person. People spend most of their time in indoor environments. The indoor ventilation systems can dilute or remove such respiratory droplets making the knowledge of respiratory droplet transmission in these scenarios essential to control the infection.

Respiratory droplet transmission is a complex problem, characterized by multiphase flow, polydisperse droplet population, multi-component mass transfer, and evaporation. In the numerical methods, the dispersed droplets can be treated in an Eulerian or Lagrangian manner. The Eulerian approach treats the dispersed droplets as a continuum rather than tracing the movement of individual droplets as in the Lagrangian approach. Therefore, the Eulerian approach generally has lower computational costs, which makes it attractive. However, it has difficulty in dealing with the polydispersity and evaporation of the respiratory droplets.

In this dissertation, to exploit the cost-effectiveness and simplicity of the Eulerian approach, the population balance equation (PBE) is coupled with the Eulerian-Eulerian (E-E) approach to trace the transmission of the polydispersed evaporating respiratory droplets. Two PBE-solving methods, the sectional method (SM) and the quadrature method of moments (QMOM) are adopted and compared. Codes for the EE-PBE approach are developed based on the open-source software OpenFOAM and verified and validated using experimental and numerical data in the literature. Then, different Eulerian approaches, including the pseudo-single-phase model (PSPM), the two-fluid model (TFM), and the EE-PBE approach, are adopted to investigate respiratory droplet transmission in ventilated indoor environments.

The developed EE-PBE approach is systematically verified and validated with experimental and numerical data in the literature. This is performed by first assessing the different aspects of the transmission process, including evaporation, movement

of the respiratory jet (or puff), and particle transmission in ventilated environments. Finally, all features are collectively considered through the examination of the transmission of polydispersed evaporating cough droplets. Good agreements are obtained for all cases, indicating that the developed EE-PBE approach can tackle the key nature of respiratory droplets, especially evaporation and polydispersity. The two PBE-solving methods, SM and QBMM are compared and discussed. Furthermore, the results confirm the suspending trend of small droplets and the falling trend of large droplets.

The different Eulerian approaches are adopted to trace respiratory droplet transmission in ventilated indoor environments. Good agreements with experimental data in the literature are found. For the Eulerian approaches, the PSPM is suitable for the transmission of small-size droplets but a suitable diffusion coefficient is required. The TFM can provide accurate predictions for the transmission of monodispersed droplets. Meanwhile, the EE-PBE approach can trace the transmission and evaporation of polydispersed droplets. For ventilation systems, the stratum ventilation (SV) supplies fresh air to the breath zone directly may be a good choice to control indoor infection. The displacement ventilation (DV), transporting the droplets upwards and providing a stratified environment, can provide protection to some areas within the environment. The mixing ventilation (MV), distributing the droplets uniformly and providing a uniform environment, may not be suitable to control indoor infection.

In conclusion, the Eulerian approach provides reliable and efficient tools to deepen the understanding of respiratory droplet transmission and assess the performances of different ventilation systems.

Contents

List of Figures

List of Tables

Nomenclature

Latin symbols

$\mathscr{U}_k$	the kth order velocity moments	...
$\mathscr{V}_k$	the kth order relative velocity moments	...
$\mathbf{g}$	gravitational acceleration vector	$\mathrm{m\,s^{-2}}$
$\mathbf{I}$	identity tensor	-
$\mathbf{R}$	stress tensor	Pa
$\mathbf{S}$	strain rate tensor	$\mathrm{s^{-1}}$
$\mathbf{U}$	velocity vector	$\mathrm{m\,s^{-1}}$
a	thermal diffusivity	$\mathrm{m^2\,s^{-1}}$
D	mass diffusivity	$\mathrm{m^2\,s^{-1}}$
d	diameter	m
E	sensible internal energy per unit mass	$\mathrm{J\,kg^{-1}}$
K	kinetic energy per unit mass	$\mathrm{J\,kg^{-1}}$
k	turbulent kinetic energy	$\mathrm{m^2\,s^{-2}}$
M_k	the kth order moments	...
p	pressure	Pa
S	source term	$\mathrm{kg\,m^{-3}\,s^{-1}}$, $\mathrm{kg\,m^{-2}\,s^{-2}}$, or $\mathrm{kg\,m^{-1}\,s^{-3}}$

Y	mass fraction	-

Greek symbols

α	volume fraction	-
ε	turbulence dissipation rate	$\mathrm{m^2\,s^{-3}}$
μ	dynamic viscosity	$\mathrm{Pa\,s}$
ρ	density	$\mathrm{m^3\,kg^{-1}}$

Superscripts and subscripts

eff   effective, containing the laminar and the turbulent contribution

lam   laminar

t   turbulent

c the cth continuous phase

d the dth disperse phase

Acronyms

AC   air curtain

ACH   air changes per hour

CIJV   corner impinging jet ventilation

DNS   direct numerical simulation

DSD   droplet size distribution

DV   displacement ventilation

E-E   Eulerian-Eulerian

E-L   Eulerian-Lagrangian

ICV   interactive cascade ventilation

IJV   impinging jet ventilation

ISV   intermittent stratum ventilation

LES   large eddy simulation

LTR   low-temperature radiant

MFM   multi-fluid model

MUSIG   multiple size group

MV   mixing ventilation

N-S   Navier-Stokes

PBE   population balance equation

PISO   pressure-implicit with splitting of operators

PIV   particle image velocimetry

PSPM   pseudo-single-phase model

QMOM   quadrature method of moments

RANS   Reynolds-averaged Navier-Stokes

RH   relative humidity

SI   shadowgraph imaging

SIMPLE   semi-implicit method for pressure-linked equations

SM   sectional method

SOM   schlieren optical method

SV   stratum ventilation

TFM   two-fluid model

TGM   tracer gas method

TPM   tracer particle method

TVD   total variation diminishing

ZV   zone ventilation

Dimensionless numbers

Le   Lewis number $\kappa/\rho D C_{\mathrm{p}}$

Nu   Nusselt number hL/κ

Pr   Prandtl number $C_{\mathrm{p}}\mu/\kappa$

Re   Reynolds number UL/ν

Sc   Schmidt number $\mu/\rho D$

Sh   Sherwood number hD/L

Chapter 1

Introduction

The COVID-19 pandemic has spread widely around the world and changed many aspects of social life. It can be transmitted by the virus-laden respiratory droplets (> 5 μm) or aerosols (< 5 μm) exhaled by an infected person during respiratory activities[1, 2]. The virus carried by the droplets or aerosols may deposit on the body of the potential host [3], contaminate the objects and surfaces [4, 5], or be suspended in the air [5–8]. Depending on different conditions, they remain viable for a period ranging from several hours to several days [9–13]. A susceptible person may be infected by contacting or inhaling the virus. Additionally, people spend most of their time in indoor environments [14], such as offices, classrooms, and hospital wards. In these circumstances, different ventilation systems, providing different airflow patterns, are widely used to dilute or remove the virus [15]. Therefore, knowledge of the transmission of respiratory droplets and aerosols in ventilated indoor environments is of great importance for breaking the transmission chain and controlling the infection.

However, transmission of respiratory droplets is a complex process characterized by its multiphase, polydisperse, multi-component nature, and the phenomenon of evaporation [16]. As illustrated in Figure 1.1, during respiratory activities, such as breathing, speaking, coughing, or sneezing, the respiratory droplets will be expelled together with the exhaled puff from the mouth or nose. The droplets, including droplet nuclei in the solid phase and droplets in the liquid phase, are carried by and interact with the exhaled breath and surrounding air in the gaseous phase, resulting in a multiphase system. The liquid droplets have multiple components, consisting
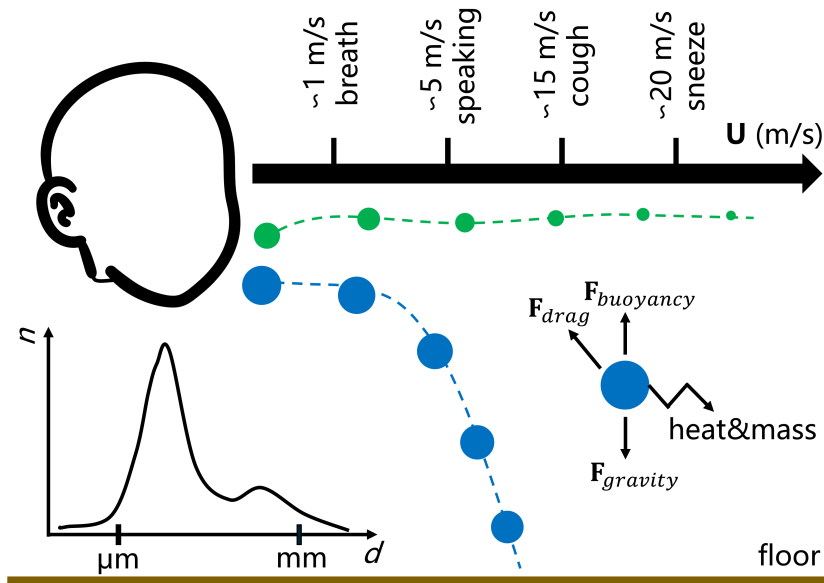
Fig. 1.1 The virus-laden droplets exhaled by an infected person during different respiratory activities.

of volatile and non-volatile substances [17], so they will partially evaporate or condensate along their trajectory. The changing sizes play an important role in their transmission [18]. Furthermore, as shown in Table 1.1, different respiratory activities generally produce puffs moving with different velocities. Obviously, the cough or sneeze droplets, possessing higher velocities, may be transported for larger ranges. Additionally, the sizes of the droplets generated during different respiratory activities vary significantly, ranging from micrometers to millimeters [19, 20]. The breath droplet size may mainly concentrate in the range of 0.1-10 µm [21–25]. Larger droplets of several hundred micrometers are found for speaking [26–29], cough [26–30], and sneeze [26, 31, 32], respectively. The sizes, affecting the rate of mass, momentum, and heat transfer between the droplets and the surrounding air, can significantly affect the behavior of droplets. The size of 100 μm is widely regarded as an important threshold in the literature [18, 33]. The larger droplets (> 100 µm) usually cannot fully evaporate, so they settle on the ground within a certain distance due to gravity. The smaller droplets (< 100 µm), on the contrary, quickly evaporating into nuclei, can be suspended in the air for longer times and transported for longer distances.

Table 1.1 Measurement of airflow velocity of respiratory activities.

Author	Method	Value	Breath (m s^{-1})	Speaking (m s^{-1})	Cough (m s^{-1})	Sneeze (m s^{-1})
Gupta et al. [34]	spirometer	peak	5.93 [1]	8.89 [1]	-	-
Tang et al. [35]	SI [4]	max, m / f [2]	-	-	3.2-14 / 2.2-5	-
Tang et al. [36]	SI	max	1.3	-	-	4.5
Xu et al. [37]	anemometer	peak, m / f	0.81 / 1.03	-	-	-
Xu et al. [38]	anemometer	peak, m / f	1.08-1.56 / 1.53-1.64	-	-	-
Fabian et al. [39]	exhalair	peak	1.98-2.97 [3]	-	-	-
Chao et al. [28]	PIV [4]	max, m / f	-	4.6 / 3.6	13.2 / 10.2	-
Tang et al. [40]	SOM [4]	max	-	-	>8	-
Kwon et al. [41]	PIV	max, m / f	-	4.07 / 2.31	15.3 / 10.6	-
Giovanni et al. [42]	image	ave	-	0.28-1.8	-	-
Tan et al. [43]	PIV	max	-	4.5-18	19.9	-
Han et al. [44]	PIV	max	-	6.25	-	15.9
Zhu et al. [45]	PIV	ave	-	-	11.2	-
Gupta et al. [46]	spirometer	peak	-	-	16.3 [1]	-
Han et al. [47]	PIV	max, m / f	-	-	15.2 / 13.1	-
VanSciver et al. [48]	PIV	ave max	-	-	10.2	-
Bahramian et al. [32]	SI, PIV	max	-	-	-	27
Scharfman et al. [49]	image	max	-	-	-	14
Nishimura et al. [50]	image	max	-	-	-	>6

[1] the peak flow rate and mouth opening for breath, speaking and cough are: 0.7 L s^{-1} and 1.18 cm^2, 1.6 L s^{-1} and 1.8 cm^2, 6 L s^{-1} and 3.685 cm^2, respectively.

[2] m denotes male, and f denotes female.

[3] the airflow rate is 14-21 L min^{-1}, and the mouth opening is assumed to be 1.18 cm^2 from Gupta et al. [34].

[4] SI: shadowgraph imaging; PIV: particle image velocimetry; SOM: schlieren optical method.

Furthermore, the ventilation systems also make a huge difference in indoor respiratory droplet transmission [51]. On the one hand, the ventilation systems supply fresh air to the indoor environments, which will change the ambient conditions, such as relative humidity and temperature. The changing ambient conditions affect the movement of the exhaled puff and the evaporation of the respiratory droplets, finally affecting the transmission of these droplets [52, 53]. On the other hand, different ventilation systems are characterized by different indoor airflow patterns. The supply air interacts with the droplet-laden exhaled puff directly, which can significantly change the trajectories of respiratory droplets. This will dilute or remove the virus-laden droplets and reduce the risk of infection. Consequently, ventilation systems are widely used to control indoor infection. However, operating under different mechanisms, they present different performances in removing the virus. Their performances are also affected by operation parameters [54], such as inlet and outlet layouts, airflow rate, temperature, and relative humidity of the supplied air. Moreover, the layouts of the indoor environments and the positions and postures of individuals within these spaces remarkably impact the indoor airflow pattern, further influencing the performance of ventilation systems. Thus, gaining a comprehensive understanding of respiratory droplet transmission in indoor environments under different ventilation systems is essential for efficient indoor infection control.

There are various methods to investigate respiratory droplet transmission. Direct experimental methods measure the transmission of droplets generated during actual respiratory activities of human volunteers and provide information on droplet velocity and size distribution. For example, Zhu et al. [45] used particle image velocimetry (PIV) to study droplet transport during cough. They found that the droplets were expelled at a velocity up to 22 m and could travel further than 2 m. Bahramian and Ahmadi [55] measured the velocity and droplet size distribution of sneeze. They found that the maximum velocity was up to $25.1 \mathrm{~m\,s^{-1}}$. The droplets ranging from 0.1 μm to 708 μm traveled more than 2.64 m at 0.6 s. Coldrick et al. [56] investigated the transmission of droplets produced during a series of real activities in an unventilated chamber. The results showed a great deposition of droplets within 1 m of the subject and a substantial number of suspending aerosols. The direct measurement can track the transmission of actual respiratory droplets. However, considering the health and safety of the volunteers and the costs and feasibility of the experiment, the surrogate methods are more widely used.

The surrogate methods, adopting tracer particles or tracer gas as surrogates of the respiratory droplets [57], are widely used to trace the transmission of respiratory droplets within ventilated environments. In the tracer particle method (TPM), the monodispersed [58–60] or polydispersed [61–63] particles generated by the particle generator are used to provide a good approximation of the respiratory droplets. Zhou et al. [64] measured the concentration of particles from 0.1 μm to 10 μm to investigate aerosol transmission in a ventilated fever clinic. They found that the occupant locations would affect the aerosol removal effectiveness. Liu et al. [65] experimentally investigated the performance of mixing ventilation (MV) and displacement ventilation (DV) using particles from 0.3 μm to 2 μm, and they found that DV presented a vertical stratification of the particle concentration, providing better air quality than MV. Li et al. [66] investigated the effect of different inlet/outlet setups of MV, stratum ventilation (SV), and interactive cascade ventilation (ICV) on the transmission of cough and sneeze aerosols (1 μm). The ICV was found to present better cross-infection control performance than SV and MV. Furthermore, to mimic the evaporation of the respiratory droplets, tracer droplets consisting of pure water or salt water are also adopted. Xu et al. [67] used the evaporating salt-water droplets (0.3 μm to 10 μm) to experimentally investigate the effectiveness of three personalized ventilation systems. Wang et al. [68] measured the concentration and size distribution of evaporation droplets (0.3 μm to 10 μm) in a negative-pressure isolation ward under MV. They found that the small droplets evaporated into nuclei very quickly, resulting in similar size distributions at different locations in the ward.

Small-size respiratory droplets (respiratory aerosols), tend to completely follow the airflow behaving like gaseous pollutants. Therefore, a tracer gas, such as CO_2 [69–71], N_2O [72–75], or SF_6 [76–78], can be adopted as a surrogate to trace the transmission of respiratory aerosols [79–81]. Studies indicate that the tracer gas method (TGM) is reasonable for the droplets of around 1 μm (0.7 μm [82], 0.8 μm [83], 1.0 μm [84], 2.5 μm [85], 3.2 μm [86], 3.5 μm [80]). Tian et al. [87] adopted CO_2 to investigate the performance of MV, DV, and SV in a small office. They found that the CO_2 source locations could affect the CO_2 removal effectiveness, and SV removed the CO_2 more effectively than MV and DV. Ameen et al. [88] compared the measured tracer gas (SF_6) decay of a novel ventilation system, corner impinging jet ventilation (CIJV), with MV and DV. It was found that the CIJV presented better air change effectiveness. Kong et al. applied CO_2 as the tracer gas in the experimental study on the coupling of the low-temperature radiant floor

and the intermittent stratum ventilation (LTR-ISV) [89], and ICV [90]. These novel ventilation systems presented a better performance in reducing infection risk.

The above experimental studies reveal the performance of different ventilation systems in removing respiratory aerosols or droplets. However, because of the limited number of measuring points, the experimental study might not fully capture the non-uniform distribution of the respiratory droplets caused by the complex indoor airflow under different ventilation systems [91]. To better control indoor infection, numerical methods are required to provide more detailed temporal evolution and spatial distribution of the respiratory droplets.

In the numerical methods, the dispersed respiratory droplets can be treated in a Lagrangian manner or an Eulerian manner. In the Lagrangian approach, the dispersed phase, the phase of the respiratory droplets, is represented by a number of individually tracked droplets [92]. Meanwhile, the continuous air phase is treated as a continuum by solving the Navier-Stokes (N-S) equations. For this reason, this approach is called the Eulerian-Lagrangian (E-L) approach. Since this approach tracks the movement and evaporation of individual droplets, it can easily tackle the features of polydispersity and evaporation of the respiratory droplets. Therefore, the E-L approach is the most widely used approach for respiratory droplet transmission. Some researchers adopted direct numerical simulation (DNS), for the continuous phase of the E-L approach to obtain more accurate descriptions of the droplet transmission [93–98]. However, most of the investigations performed so far have used the Reynolds-averaged Navier–Stokes (RANS) equations to perform studies concerning different scenarios, such as elevator [99], airplane cabin [100], car cabin [101, 102], classroom [103], restaurant [104], bus [105], and ship [106]. The factors influencing the droplet transmission, such as relative humidity [107, 108], evaporation [107, 109], wind speed [107–109], and movement of the source [110], were also explored.

In particular, the effect of ventilation systems on the transmission of polydispersed evaporating respiratory droplets was also investigated using the E-L approach [111–114]. Wang et al. [115] adopted particles ranging from 1 μm to 100 μm to investigate the performance of IJV and two forms of MV using the E-L approach. Ren et al. [116] used the E-L approach to trace the transmission of particles with different diameters (3, 6, 12, 20, 45, 175 μm) in a ventilated ward. Motamedi et al. [117] adopted the E-L approach to investigate the transmission of speaking

droplets (2 μm to 1000 μm) in confined space under different ventilation strategies, i.e. cross, single-side, no ventilation, and mechanical ventilation. In the work of Liu and Deng [118], the transmission of dry droplet nuclei (0.75 μm to 330 μm) in an elevator with MV was simulated using the E-L approach. In these studies, the E-L approach confirmed the effectiveness of different ventilation systems to dilute or remove respiratory droplets and accurately predicted the different fates of droplets of larger size ranges. Both simulations and experiments show similar results: large droplets deposit on the ground whereas small ones are removed by the ventilation systems.

Also, the evaporation of respiratory droplets can be easily modeled by using the E-L approach, Borro et al. [119] traced the dispersion of evaporating droplets ranging from 3 μm to 750 μm in a ventilated hospital room; Li and Feng [120] investigated the transmission of evaporating droplets (1 μm to 1500 μm) under air curtain (AC), MV, and DV; Lu and Lin [121] considered evaporation in their simulation of cough droplets dispersion in a ward under DV, SV, and MV. In particular, Zhang et al. [122] adopted large eddy simulation (LES) for the continuous phase and the Lagrangian approach for the disperse phase to investigate the droplet transmission during coughing and talking in a room equipped with MV and DV. The evaporation of droplets with initial sizes of 1, 10, 20, 50, and 100 μm was modeled. They found that in the case of DV, the 100 μm droplets showed a downward movement due to gravity at the beginning, which was different from the smaller droplets. With time going by, the 100 μm droplets evaporated into smaller sizes, and moved upwards because of the buoyant airflow of DV. These studies revealed the effect of evaporation on the trajectories of varied-size respiratory droplets and indicated the importance of considering evaporation in studies of respiratory droplet transmission.

These studies present the advantages of the E-L approach to easily dealing with the important characteristics of respiratory droplets, specifically, their polydispersity and evaporation. This approach can reveal the underlying mechanisms of respiratory droplet transmission in ventilated indoor environments and explore the influencing factors. However, considering the escalating complexity of indoor environments, the E-L approach may have disadvantages in computational costs [123], stability in non-uniform environments [124], and requirement on computational mesh [125]. Consequently, the pursuit of reliable and efficient numerical methods is still imperative.

The dispersed respiratory droplets can also be treated in an Eulerian manner, where the droplets are regarded either as a continuum in the same continuous phase with the air or as an additional continuum interpenetrating with the continuous air phase. The former is the pseudo-single-phase model (PSPM) and the latter is the Eulerian-Eulerian (E-E) approach. Such simplified treatments make the Eulerian approaches have relatively lower computational costs in comparison to the Lagrangian one [126].

The idea of the PSPM is similar to that of the tracer gas method, the small-size droplets tend to completely follow the airflow, presenting behaviors similar to that of a gaseous solute. Consequently, in the PSPM, the small-size droplets and the air are in the same gaseous phase, namely, the pseudo-single-phase. To trace the droplet transmission, one scalar transport equation for concentration [127] or species mass fraction [128], representing the local amount of droplets, is solved together with the N-S equations for this phase. Because of its simplicity, this approach is widely used in studies on ventilation systems [129–133]. Ren et al. [134] adopted the PSPM to investigate the performance of DV, MV, SV, and zone ventilation (ZV) in mitigating the spread of infectious diseases in an office. They found that SV provided the lowest infection risk, showing better performance in controlling infection than the other three ventilation systems. Wang et al. [135] coupled the Wells-Riley model with the PSPM to estimate the infection probability in a ventilated train. They found that the distribution of infectious aerosols is non-uniform and dependent on the setups of ventilation systems. Hatif et al. [136] solved the species transport equation to investigate the effect of furniture layout on exposure risk to respiratory droplet nuclei in an office served by MV and DV. It was found that placing a desk increased the exposure risk by 50% for DV and 22% for MV. Increasing the separation distance between occupants reduced the exposure risk. The PSPM is generally used for the transmission of monodispersed small-size respiratory droplets (~ 1 μm). For larger droplets that do not completely follow the airflow, the E-E approach is required.

The E-E approach treats the dispersed droplets as a continuum interpenetrating with the air phase. Two sets of N-S equations, containing interphase interaction terms, are solved for the continuous phase (air) and the dispersed phase (droplets), respectively. Thus, it can be called the two-fluid model (TFM). As the droplet velocity is determined by solving the governing equations, the droplet velocity, dependent on the interphase interactions, can be different from or the same as the air velocity. Consequently, compared with the PSPM, the E-E approach can be used

to track the transmission of not only small but also large droplets. However, the calculation of interphase interaction terms requires a single representative diameter. As a result, the E-E approach is more suitable for the transmission of monodispersed droplets. Some simplified E-E approaches have already been applied in particle-laden flows in indoor environments, such as the drift-flux model [137–141] and the mixture model [138]. In particular, Diwan et al. [142] adopted DNS to study the evolution of cough or sneeze flow without droplets. In their later works, they coupled the E-E approach with DNS to investigate the dispersion of small cough droplets (10 μm) [143] and the virus transmission during short conversations [144]. Furthermore, Yan et al. [145] compared the TFM with the E-L approach in their study on the transport of non-evaporating aerosols (0.2, 0.77 and 2.5 μm) in a ventilated room. It was found that the two approaches had similar accuracy in predicting the airflow field. They indicated that the E-E approach had advantages in providing a mechanistic description of the inter-phase interactions, while the E–L approach had an advantage in modeling particle–wall interactions. Pei et al. [146] compared the TFM with the PSPM in the study of aerosol transmission (1 μm and 10 μm) in a room equipped with DV and MV. The concentration distributions for the aerosols of 1 μm and 10 μm obtained using the TFM were different: the former was similar to the results of the PSPM while the latter exhibited lower concentration due to deposition. This finding confirmed the applicability range of the two methods, as previously mentioned.

It can be noted that the E-E approach is less adopted in respiratory droplet transmission in ventilated indoor environments because it has difficulty in dealing with the polydispersity and evaporation of the droplets. Nevertheless, given its cost-effectiveness and simplicity, the development of novel methodologies based on the E-E approach remains significant.

Therefore, the objective of this dissertation is to develop a flexible, robust, and computationally cheap tool based on the E-E approach to investigate the transmission of polydispersed evaporating respiratory droplets within ventilated indoor environments. To achieve this objective, the population balance equation (PBE) is introduced. The PBE is a continuity statement written in terms of the droplet size distribution (DSD), providing a comprehensive depiction of the dispersed phase dynamics [147]. In recent years, the PBE was coupled with TFM and applied in polydispersed bubble flows with [148] or without [149] interphase mass transfer and favorable performances were obtained. However, this coupled approach has not yet been employed in the investigation of respiratory droplet transport. Con-

sequently, the EE-PBE coupled approach capable of tracing the transmission and evaporation of polydispersed respiratory droplets will be developed and presented in this dissertation.

This dissertation is organized as follows:

- in Chapter 2, the different Eulerian approaches are introduced, including the PSPM, the MFM, the PBE, and the EE-PBE coupled approaches. The codes are developed based on the open-source software OpenFOAM and the solution algorithms are presented;

- in Chapter 3, the developed methods and codes are verified and validated with the experimental and numerical results in the literature. The abilities of the developed methods to deal with the problem of droplet evaporation, respiratory activity, particle-laden flows, and finally transmission of polydispersed evaporation droplets, are assessed;

- in Chapter 4, the developed methods and codes are applied in droplet transmission in ventilated indoor environments. Transmission of gaseous pollutants in an office under DV, SV, and MV, transmission of particles in an office under DV and MV, and transmission of evaporating droplets in a ward under MV are investigated using different Eulerian approaches and compared with the experimental data in the literature. The performances of different ventilation systems are discussed;

- in Chapter 5, some conclusions are presented.

Chapter 2

Methodology

The transmission of respiratory droplets in indoor environments is a complex multi-phase system, and it can be simulated using the Eulerian approach or the Lagrangian approach. In this chapter, different Eulerian approaches are presented and organized as: the pseudo-single-phase model (PSPM) in Section 2.1; the Eulerian-Eulerian model, namely, multi-fluid model (MFM) in Section 2.2; turbulent closures for Eulerian models are discussed in Section 2.3; finally, the population balance equation (PBE) that can be coupled to Eulerian models to predict the droplet size distribution is introduced in Section 2.4.
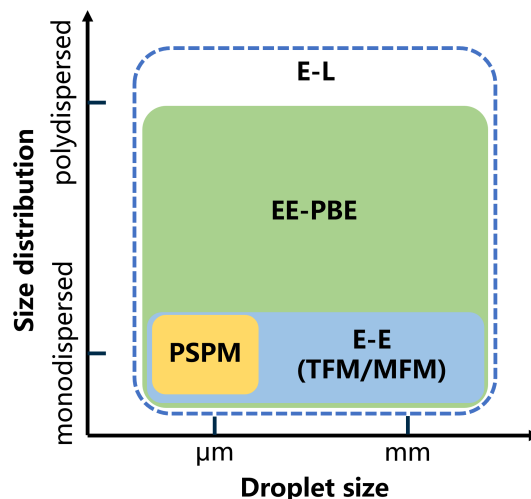
Fig. 2.1 The numerical methods for the transmission of respiratory droplets.

2.1 Pseudo-single-phase model

The smallest-size respiratory droplets or aerosols tend to completely follow the airflows because they generally have very small momentum response times [150]. Such aerosols, sharing the velocity of the airflow, can be regarded as belonging to the gaseous phase of the airflow. Therefore, the multiphase problem is reduced to a pseudo-single-phase problem, where the term pseudo is to stress the existence of the aerosols. In the pseudo-single-phase model (PSPM), the velocity of the aerosols can be obtained by solving the Reynolds-averaged Navier-Stokes (RANS) equations, where the continuity equation can be written as:

$$\frac{\partial \rho}{\partial t} + \nabla \cdot (\rho \mathbf{U}) = S_{\text{mass}}, \tag{2.1}$$

where ρ is the density; $\mathbf{U}$ is the velocity; and S_{mass} is the mass source term.

The momentum equation can be written as:

$$\frac{\partial}{\partial t}(\rho \mathbf{U}) + \nabla \cdot (\rho \mathbf{U} \otimes \mathbf{U}) = -\nabla p + \nabla \cdot \mathbf{R}_{\text{eff}} + \rho \mathbf{g} + S_{\text{momentum}}, \tag{2.2}$$

where p is the pressure; $\mathbf{g}$ is the gravity acceleration vector; S_{momentum} is the momentum source term; and $\mathbf{R}_{\text{eff}}$ is the effective stress tensor containing the molecular and turbulent contributions, so it can be expressed as:

$$\mathbf{R}_{\text{eff}} = 2\mu_{\text{eff}} \left[\mathbf{S} - \frac{1}{3}(\nabla \cdot \mathbf{U})\mathbf{I} \right], \tag{2.3}$$

where $\mu_{\text{eff}} = \mu + \mu_{\text{t}}$ is the effective dynamic viscosity; μ is the molecular dynamic viscosity; μ_{t} is the turbulent dynamic viscosity that can be obtained from the turbulence model; $\mathbf{S} = \frac{1}{2} \left[\nabla \mathbf{U} + (\nabla \mathbf{U})^{\text{T}} \right]$ is the strain rate tensor; and $\mathbf{I}$ is the identity tensor.

The energy equation can be written as:

$$\frac{\partial}{\partial t}(\rho E) + \nabla \cdot (\rho \mathbf{U} E) + \frac{\partial}{\partial t}(\rho K) + \nabla \cdot (\rho \mathbf{U} K) = -\nabla \cdot (p \mathbf{U}) + \nabla \cdot (a_{\text{eff}} \nabla E)$$
$$+ \rho \mathbf{g} \cdot \mathbf{U} + S_{\text{energy}}, \tag{2.4}$$

where E is the sensible internal energy; $K = \frac{1}{2}|\mathbf{U}|^2$ is the kinetic energy; $a_{\text{eff}} = \kappa_{\text{eff}}/(\rho C_{\text{p}})$ is the effective thermal diffusivity; and S_{energy} is the energy source

term. The equation neglects the contribution of radiation to energy transfer and, consequently, it should be used only when the temperature of the droplets does not differ too much from that of the surrounding walls.

Finally, the concentration of the aerosols is traced by a scalar transport equation, such as the transport equation for a dilute dissolved species:

$$\frac{\partial}{\partial t}(\rho Y_s) + \nabla \cdot (\rho \mathbf{U} Y_s) - \nabla \cdot (\rho D_{\mathrm{eff}} \nabla Y_s) = S_{\mathrm{specie},s}, \quad s = 1, 2, \dots, M-1 \quad (2.5)$$

where Y_s is the mass fraction of the sth species for the total of $M-1$ dissolved species, and $\sum_{s=1}^{M} Y_s = 1$ where M is the index of the main component; D_{eff} is the effective diffusion coefficient shared by all species, equal to the sum of the molecular contribution D_s and the turbulent contribution $D_{\mathrm{t}} = \mu_{\mathrm{t}}/(\rho \mathrm{Sc_t})$, and the default value for the turbulent Schmidt number $\mathrm{Sc_t}$ is 0.7; and $S_{\mathrm{specie},s}$ is the source term for the sth specie.

If neglecting the effect of changing gas composition, Eq. 2.5 becomes the concentration transport equation of the disperse phase, where the scalar concentration is passively transported by the airflow.

2.2   Multi-fluid model

The multiphase flow of transmission of respiratory droplets can also be solved using the multi-fluid model (MFM), one kind of E-E approach. In MFM, both the continuous phases and the dispersed phases are treated as interpenetrating continua. The concept of volume fraction, representing the space occupied by each phase, and denoted by α_i for the ith phase, is introduced.

For N phases, the volume fraction for the ith phase α_i is defined as:

$$\alpha_i = \frac{V_i}{\sum_{i=1}^{N} V_i}, \quad (2.6)$$

where V_i is the volume of phase i, and

$$\sum_{i=1}^{N} \alpha_i = 1. \quad (2.7)$$

2.2.1 Conservation equations of the multi-fluid model

With volume fractions, mass, momentum, and energy conservation equations similar to single-phase flows can be established for each phase. The continuity equation for the ith phase can be written as:

$$\frac{\partial}{\partial t}(\alpha_i \rho_i) + \nabla \cdot (\alpha_i \rho_i \mathbf{U}_i) = \sum_{j=1, j \neq i}^{N} (\dot{m}_{ji} - \dot{m}_{ij}), \qquad (2.8)$$

where the subscript i denotes the ith phase; the subscript j denotes the jth phase and $j \neq i$; so, ρ_i is the density of the ith phase and other variables are denoted in the same way; $\dot{m}_{ji}$ is the mass transfer rate from the jth phase to the ith phase; and $\dot{m}_{ij}$ is the mass transfer rate from the ith phase to the jth phase. The mass transfer is caused by the phase change, such as evaporation or condensation.

The momentum equation for the ith phase can be written as:

$$\frac{\partial}{\partial t}(\alpha_i \rho_i \mathbf{U}_i) + \nabla \cdot (\alpha_i \rho_i \mathbf{U}_i \otimes \mathbf{U}_i) = -\alpha_i \nabla p + \nabla \cdot (\alpha_i \mathbf{R}_{\text{eff},i}) + \alpha_i \rho_i \mathbf{g}$$
$$+ \sum_{j=1, j \neq i}^{N} (\mathbf{F}_{ij} + \dot{m}_{ji} \mathbf{U}_j - \dot{m}_{ij} \mathbf{U}_i), \qquad (2.9)$$

where $\mathbf{F}_{ij}$ is the interphase force term; $\dot{m}_{ji}\mathbf{U}_j$ and $\dot{m}_{ij}\mathbf{U}_i$ are the interphase momentum transfer rates caused by mass transfer. Additionally, it should be noted that all phases share the same pressure p.

The energy equation for the ith phase can be written as:

$$\frac{\partial}{\partial t}(\alpha_i \rho_i E_i) + \nabla \cdot (\alpha_i \rho_i \mathbf{U}_i E_i) + \frac{\partial}{\partial t}(\alpha_i \rho_i K_i) + \nabla \cdot (\alpha_i \rho_i \mathbf{U}_i K_i)$$
$$= -\alpha_i \nabla \cdot (p \mathbf{U}_i) + \nabla \cdot (\alpha_i a_{\text{eff},i} \nabla E_i) + \alpha_i \rho_i \mathbf{g} \cdot \mathbf{U}_i \quad (2.10)$$
$$+ \sum_{j=1, j \neq i}^{N} (\dot{Q}_{ji} + \dot{m}_{ji} K_j - \dot{m}_{ij} K_i),$$

where $\dot{Q}_{ji}$ is the interphase heat transfer term from the jth phase entering the ith phase; $\dot{m}_{ji}K_j$ and $\dot{m}_{ij}K_i$ are the interface kinetic energy transfer caused by mass transfer. Similar to the PSPM, this equation does not take the effect of radiation into account.

Additionally, when considering phase change, some phases might be multicomponent, namely containing M species, the species transport equations for the ith phase can be written as:

$$\frac{\partial}{\partial t}(\alpha_i \rho_i Y_{s,i}) + \nabla \cdot (\alpha_i \rho_i \mathbf{U}_i Y_{s,i}) - \nabla \cdot (\alpha_i D_{\text{eff},i} \nabla Y_{s,i}) = \sum_{j=1}^{N} \left(\dot{m}_{s,ji} - \dot{m}_{s,ij} \right), \quad (2.11)$$

where $\dot{m}_{s,ji}$ is the mass transfer rate of the sth specie from the jth phase to the ith phase; and $\dot{m}_{s,ij}$ is the mass transfer rate of the sth specie from the ith phase to the jth phase. It should be noted that:

$$\dot{m}_{ji} = \sum_{s=1}^{M} \dot{m}_{s,ji}, \quad (2.12)$$

and

$$\dot{m}_{ij} = \sum_{s=1}^{M} \dot{m}_{s,ij}. \quad (2.13)$$

In most cases of this dissertation, we will use only one continuous phase and one disperse phase, so that the MFM reduces to the two-fluid model (TFM), but sometimes, we will need to include in the model two disperse phases of different sizes, and solve a real MFM. In the latter case, however, we will neglect the interphase transfer terms (of mass, momentum, and heat) between the disperse phases and only include the terms between each single disperse phase and the continuous phase; indeed, the multiphase systems of the respiratory droplets transmission are quite dilute with no coalescence or breakup, and thus we can assume that all interphase transfer processes are mediated by the continuous phase.

The closures of the MFM are discussed in the following part. For clarity, the phase indicator i and j can be replaced by c and d, denoting the continuous phase and the dth disperse phase, respectively.

2.2.2 Closures of the multi-fluid model

Interphase force term

In MFM, depending on the feature of the multiphase flows to be simulated, different interphase forces, such as drag force, lift force, virtual mass force, and so on, should

be included [150]. For the multiphase system of respiratory droplet transport, the density of the dispersed droplets ($\rho_{\mathrm{droplets}} = 998.2\ \mathrm{kg\,m^{-3}}$) is much larger than the continuous air ($\rho_{\mathrm{air}} = 1.2\ \mathrm{kg\,m^{-3}}$), and the sizes of the droplets are relatively small. Therefore, the droplet weight and drag force are largely predominant over the other forces and are consequently included in most of the literature [151–155].

In this dissertation, the droplet weight is considered through the gravity term of Eq. (2.9), and the interphase force term includes only the drag interaction:

$$\mathbf{F}_{dc} = \mathbf{F}_{\mathrm{D},dc}, \tag{2.14}$$

where $\mathbf{F}_{\mathrm{D},dc}$ is the volumetric drag force between the continuous phase c and the dth disperse phase, and it can be calculated as follows [1]:

$$\mathbf{F}_{\mathrm{D},dc} = \frac{3}{4} C_{\mathrm{D}} \mathrm{Re}_{\mathrm{r}} \frac{\alpha_d \rho_c \nu_c}{d_d^2} (\mathbf{U}_c - \mathbf{U}_d), \tag{2.15}$$

where C_{D} is the drag coefficient, d_d is the dth disperse phase diameter; ν_c is the continuous phase kinematic viscosity; $\mathrm{Re}_{\mathrm{r}} = d_d |\mathbf{U}_c - \mathbf{U}_d| / \nu_c$ is the relative Reynolds number; the drag coefficient C_{D} can be calculated using the empirical relationship from Schiller and Naumann [156] as:

$$C_{\mathrm{D}} = \begin{cases} 24\left(1 + 0.15\mathrm{Re}_{\mathrm{r}}^{0.687}\right)/\mathrm{Re}_{\mathrm{r}}, & \mathrm{Re}_{\mathrm{r}} \leq 1000; \\ 0.44, & \mathrm{Re}_{\mathrm{r}} > 1000. \end{cases} \tag{2.16}$$

The above relationship is for an isolated droplet. Since the system of respiratory droplets in this dissertation is assumed to be dilute, the droplets can be regarded as isolated. Therefore, it is reasonable to adopt this model.

---

[1]The volumetric drag force, $\mathbf{F}_{\mathrm{D},dc}$, is obtained as the product of the drag force acting on a single droplet:

$$C_{\mathrm{D}} \left(\frac{\pi d_d^2}{4}\right) \rho_c \frac{|\mathbf{U}_c - \mathbf{U}_d|(\mathbf{U}_c - \mathbf{U}_d)}{2},$$

and the number of droplets per unit volume:

$$\frac{6\alpha_d}{\pi d_d^3}.$$

Finally, the interface force term for the continuous phase is obtained according to Newton's action and reaction law:

$$\mathbf{F}_{cd} = -\mathbf{F}_{dc} = -\mathbf{F}_{\text{D},dc}. \tag{2.17}$$

Interphase mass transfer

The phase changes will result in the mass transfer between different phases. For the respiratory droplets consisting of volatile and non-volatile substances, evaporation will happen. Therefore, the interphase mass transfer caused by evaporation or condensation will be considered in this dissertation.

Similar to most of the literature, water is regarded as the only evaporable substance in the system. As a result, the continuous phase, the phase of air, has two components, water vapor, and dry air, while the disperse phase, the phase of droplets, only consists of pure liquid water. During evaporation or condensation, the mass transfer of water happens, and the mass transfer rate of water per unit volume between the continuous phase and the dth disperse phase, $\dot{m}_d$, can be calculated as:

$$\dot{m}_d = \rho_c k_d (Y_{\text{f},d} - Y_{\text{H}_2\text{O}}), \tag{2.18}$$

where k_d is the volumetric mass transfer coefficient of the dth interface; $Y_{\text{f},d}$ and $Y_{\text{H}_2\text{O}}$ are the water vapor mass fraction of the dth interface and in the bulk gas phase, respectively. The former can be obtained by the saturation condition discussed below and the latter is obtained by solving the species transport equation, Eq. (2.11), for water vapor.

Since water is the only evaporable specie, when $\dot{m}_d \geq 0$, liquid water evaporates and thus $\dot{m}_{dc} = \dot{m}_d$ and $\dot{m}_{cd} = 0$. When $\dot{m}_d < 0$, water vapor undergoes condensation and thus $\dot{m}_{cd} = -\dot{m}_d$ and $\dot{m}_{dc} = 0$.

The volumetric mass transfer coefficient of the dth interface, k_d, can be calculated as [2]:

$$k_d = \frac{6\alpha_d \text{Sh} D_c}{d_d^2}, \tag{2.19}$$

---

[2]The volumetric mass transfer coefficient of the dth interface, k_d, is obtained as the product of the mass transfer coefficient per unit interfacial area k_d^* that is included in the Sherwood number and the volumetric interfacial area $\alpha_{\text{v},d} = 6\alpha_d/d_d$.

where D_c is the molecular diffusivity of water vapor in the continuous phase; and $\text{Sh} = k_d^* d_d / D_c$ is the Sherwood number, calculated using the Frössling equation [157] as:

$$\text{Sh} = 2 + 0.552\text{Re}_r^{1/2}(\text{LePr})^{1/3}, \qquad (2.20)$$

where $\text{Le} = a_c / D_c$ is the Lewis number [3] defined as the ratio of thermal diffusivity a_c to mass diffusivity D_c; and $\text{Pr} = v_c / a_c$ is the Prandtl number defined as the ratio of momentum diffusivity (kinetic viscosity) v_c to thermal diffusivity a_c. It should be noted that only the volumetric mass transfer coefficient on the continuous phase side is required because the disperse phase (droplets) is assumed to consist of pure water offering no resistance.

The mass fraction of vapor at the dth interface, $Y_{f,d}$, is obtained by prescribing saturation of the vapor at the interface:

$$Y_{f,d} = \frac{M_{H_2O}}{\bar{M}} \frac{p_{Sat,d}}{p}, \qquad (2.21)$$

where M_{H_2O} is the molecular weight of water, $\bar{M}$ is the average molecular weight of the mixture of water vapor and dry air in the continuous phase, and $p_{Sat,d}$ is the saturation pressure at the dth interface under interfacial temperature $T_{f,d}$. The following Antoine equation describes satisfactorily the saturation pressure of water vapor in the usual range of room temperatures and has been used for the simulations reported in the thesis:

$$p_{Sat,d} = \exp\left(A + \frac{B}{C + T_{f,d}}\right), \qquad (2.22)$$

where $A = 23.952$, $B = -4233.7$ and $C = -31.737$ [52, 158].

Interphase heat transfer

The interphase heat transfer has a close relationship with the interphase mass transfer: on the one hand, the phase changes are accompanied by absorbing or releasing heat; on the other hand, the mass fluxes will also result in heat fluxes. In order to better describe the heat transfer process and accurately obtain $T_{f,d}$, the two-resistance model, considering the different heat resistance of the continuous and dispersed phase, is adopted here.

---

[3]The product, LePr, in chemical engineering is referred to as Schmidt number, $\text{Sc} = v_c / D_c$.

At the dth interface, the heat flux entering the dth disperse phase $\dot{Q}_{cd}$ and the heat flux entering the continuous phase $\dot{Q}_{dc}$ can be written as:

$$\dot{Q}_{cd} = \dot{Q}_{\mathrm{f}d,d} + \dot{m}_{\mathrm{f}d,d} E_{\mathrm{f}d,d}, \tag{2.23}$$

$$\dot{Q}_{dc} = \dot{Q}_{\mathrm{f}c,d} + \dot{m}_{\mathrm{f}c,d} E_{\mathrm{f}c,d}, \tag{2.24}$$

where $\dot{Q}_{\mathrm{f}d,d}$ and $\dot{Q}_{\mathrm{f}c,d}$ are the convective heat fluxes from the dth interface entering the dth disperse phase and the continuous phase, respectively; $\dot{m}_{\mathrm{f}d,d}$ and $\dot{m}_{\mathrm{f}c,d}$ are the mass fluxes of water from the dth interface entering the dth disperse phase and the continuous phase, respectively; $E_{\mathrm{f}d,d}$ is the sensible internal energy of liquid water for the dispersed phase at the interface and $E_{\mathrm{f}c,d}$ is the sensible internal energy of gaseous water for the continuous phase at the interface.

The dth interface temperature, $T_{\mathrm{f},d}$, is assumed to be identical on both sides of the interface. Therefore, the convective heat flux $\dot{Q}_{\mathrm{f}d,d}$ and $\dot{Q}_{\mathrm{f}c,d}$ can be written as:

$$\dot{Q}_{\mathrm{f}d,d} = h_{d,d}(T_{\mathrm{f},d} - T_d), \tag{2.25}$$

$$\dot{Q}_{\mathrm{f}c,d} = h_{c,d}(T_{\mathrm{f},d} - T_c), \tag{2.26}$$

where $h_{d,d}$ and $h_{c,d}$ are the volumetric heat transfer coefficients at the dth interface for the dth disperse phase side and continuous phase side, respectively; T_d and T_c are the phase temperatures.

The coefficient $h_{c,d}$, describing the turbulent heat transfer from the surface of a sphere to the surrounding fluid, can be calculated as [4]:

$$h_{c,d} = \frac{6\alpha_d \kappa_c \mathrm{Nu}}{d_d^2}, \tag{2.27}$$

where κ_c is the continuous phase thermal conductivity; and $\mathrm{Nu} = h_{c,d}^* d_d / \kappa_c$ is the Nusselt number calculated by the Ranz-Marshall correlation [159, 160] as:

$$\mathrm{Nu} = 2 + 0.6 \mathrm{Re}_{\mathrm{r}}^{1/2} \mathrm{Pr}^{1/3}. \tag{2.28}$$

---

[4]The volumetric heat transfer coefficient, $h_{c,d}$, is the product of the coefficient per unit interface area, $h_{c,d}^*$, that is included in the Nusselt number and the volumetric interface area $\alpha_{\mathrm{v},d} = 6\alpha_d / d_d$.
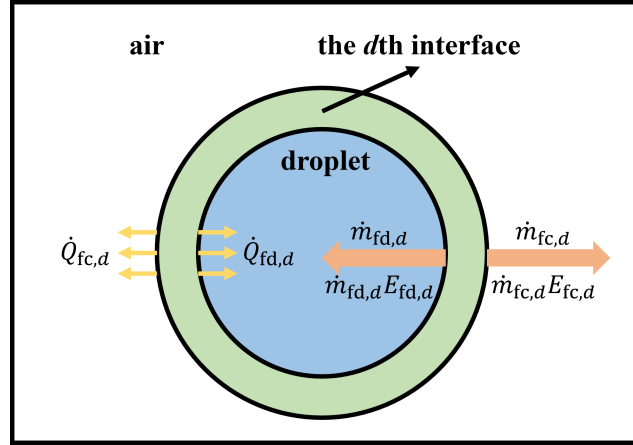
Fig. 2.2 The mass and heat fluxes in the interface between the droplet and the surrounding air.

The coefficient $h_{d,d}$, describing the heat transfer from the surface of a sphere to the fluid within the sphere, can be calculated as:

$$h_{d,d} = \frac{60\alpha_d \kappa_d}{d_d^2}, \tag{2.29}$$

where $\mathrm{Nu} = 10$ is the intermediate value between $\mathrm{Nu} \approx 6.58$ for a stagnant droplet and $\mathrm{Nu} \approx 17.7$ for a circulating droplet [161].

Since neither mass nor heat can be stored at the dth interface, as shown in Figure 2.2, the mass and heat balance at the interface can be written as follows:

$$\begin{cases} \dot{m}_{\mathrm{fd},d} + \dot{m}_{\mathrm{fc},d} = 0, \\ (\dot{Q}_{\mathrm{fd},d} + \dot{m}_{\mathrm{fd},d} E_{\mathrm{fd},d}) + (\dot{Q}_{\mathrm{fc},d} + \dot{m}_{\mathrm{fc},d} E_{\mathrm{fc},d}) = 0. \end{cases} \tag{2.30}$$

Because $\dot{m}_{\mathrm{fd},d} = -\dot{m}_d$, Eq. (2.30) becomes:

$$h_{d,d}(T_{\mathrm{f},d} - T_d) + h_{c,d}(T_{\mathrm{f},d} - T_c) = \dot{m}_{\mathrm{fd},d}(E_{\mathrm{fc},d} - E_{\mathrm{fd},d}) = -\dot{m}_d L_d, \tag{2.31}$$

where $L_d = E_{\mathrm{fc},d} - E_{\mathrm{fd},d}$ is the latent heat of water. $T_{\mathrm{f},d}$ can be calculated as:

$$T_{\mathrm{f},d} = \frac{h_{d,d} T_d + h_{c,d} T_c - \dot{m}_d L_d}{h_{d,d} + h_{c,d}}. \tag{2.32}$$

Interphase updates

To obtain the mass and heat transfer rates in the dth interface, $T_{\mathrm{f},d}$ is required. However, Eq. (2.32) is non-linear because $Y_{\mathrm{f},d}$ in Eq. (2.18) is a non-linear (exponential) function of $T_{\mathrm{f},d}$ as in Eq. (2.22). As a result, the Newton method is adopted to solve for $T_{\mathrm{f},d}$ as follows [162]:

$$T_{\mathrm{f},d}^{n+1} = T_{\mathrm{f},d}^{n} - \frac{f(T_{\mathrm{f},d})}{f'(T_{\mathrm{f},d})}, \qquad (2.33)$$

where: $f(T_{\mathrm{f},d}) = h_{\mathrm{d},d}(T_{\mathrm{f},d} - T_d) + h_{\mathrm{c},d}(T_{\mathrm{f},d} - T_{\mathrm{c}}) + \dot{m}_d L_d$, is constructed from Eq. (2.31), $f'(T_{\mathrm{f},d})$ is its first order derivative, the superscript n represents the known current iteration step, and thus $n+1$ is the unknown next step. The initial guess $T_{\mathrm{f},d}^{1}$ is equal to the converged result of the last iteration. After iteration, the converged $T_{\mathrm{f},d}$ will be used in Eq. (2.18), Eq. (2.23) and Eq. (2.24) to update the interfacial mass and heat transfer.

2.3 Turbulence closure

The RANS equations are adopted to model the turbulent flows of indoor environments. The RNG $k - \varepsilon$ model [163] presents a better performance for the indoor airflows compared with other turbulence models [164–170]. It is also found to be more accurate than the laminar model when the Reynolds number is relatively small (Re = 1600) [171]. As a result, it is widely used in studies on the indoor transport of respiratory droplets [172].

Table 2.1 gives the Reynolds numbers of the cases investigated in this dissertation. It can be noted that the Reynolds numbers are relatively large and the RNG $k - \varepsilon$ model was adopted in most cases. Therefore, considering its performance and to better compare with the literature, the RNG $k - \varepsilon$ model will be used in this dissertation.

In the RNG $k - \varepsilon$ model for the compressible multiphase flows, the transport equation of the turbulent kinetic energy for the ith phase k_i can be written as:

$$\frac{\partial}{\partial t}(\alpha_i \rho_i k_i) + \nabla \cdot (\alpha_i \rho_i \mathbf{U}_i k_i) = \nabla \cdot \left[\alpha_i \left(\frac{\mu_{\mathrm{t},i}}{\sigma_k} + \mu_i \right) \nabla k_i \right] + P_{k,i} - \alpha_i \rho_i \varepsilon_i, \qquad (2.34)$$

Table 2.1 Reynolds number for the cases investigated in this dissertation.

Case	Methods[1]	Turbulence model	Re (-)
Section 3.3 Wang et al. [173]	EXP & SIM	LES	Mouth: 26385.2
Section 3.4 Chen et al. [137]	EXP & SIM	RNG $k-\varepsilon$	Chamber: 5936.7
Section 3.5 Li et al. [52]	SIM	RNG $k-\varepsilon$	Mouth: 17678.1
Section 4.1 Tian et al. [87]	EXP	-	DV: 6104.5 SV: 17396.8 MV: 17396.8
Section 4.2 Liu et al. [65]	EXP & SIM	RNG $k-\varepsilon$	DV: 49075.7 MV: 27110.8
Section 4.3 Wang et al. [68]	EXP & SIM	RNG $k-\varepsilon$	MV: 17097.6

[1] EXP denotes experiment and SIM denotes simulation.

where $P_{k,i}$ is the production term calculated as follows:

$$P_{k,i} = \alpha_i \mu_{\text{t},i} \left[\nabla \mathbf{U}_i : \left(2\mathbf{S}_i - \frac{2}{3} \left(\nabla \cdot \mathbf{U}_i \right) \mathbf{I} \right) \right] - \frac{2}{3} \alpha_i \rho_i k_i \nabla \cdot \mathbf{U}_i. \qquad (2.35)$$

The transport equation of the turbulent dissipation rate for the ith phase ε_i can be written as:

$$\frac{\partial}{\partial t} \left(\alpha_i \rho_i \varepsilon_i \right) + \nabla \cdot \left(\alpha_i \rho_i \mathbf{U}_i \varepsilon_i \right) = \nabla \cdot \left[\alpha_i \left(\frac{\mu_{\text{t},i}}{\sigma_\varepsilon} + \mu_i \right) \nabla \varepsilon_i \right] + C_1 P_{k,i} \frac{\varepsilon_i}{k_i} \\ - R_{\varepsilon,i} + C_2 \alpha_i \rho_i \frac{\varepsilon_i^2}{k_i}, \qquad (2.36)$$

where the term $R_{\varepsilon,i}$ is calculated as:

$$R_{\varepsilon,i} = \alpha_i \rho_i \frac{C_\mu \eta_i^3 (1 - \eta_i/\eta_0)}{1 + \beta \eta_i^3} \frac{\varepsilon_i^2}{k_i}, \qquad (2.37)$$

and η_i is calculated as:

$$\eta_i = \frac{k_i}{\varepsilon_i} \sqrt{\left| \nabla \mathbf{U}_i : \left[2\mathbf{S}_i - \frac{2}{3} \left(\nabla \cdot \mathbf{U}_i \right) \mathbf{I} \right] \right|}. \tag{2.38}$$

With k_i and ε_i, the turbulent viscosity $\mu_{\mathrm{t},i}$ can be calculated as:

$$\mu_{\mathrm{t},i} = \rho_i C_\mu \frac{k_i^2}{\varepsilon_i}. \tag{2.39}$$

Finally, the default model coefficients are: $C_\mu = 0.0845$, $C_1 = 1.42$, $C_2 = 1.68$, $\sigma_k = 0.71942$, $\sigma_\varepsilon = 0.71942$, $\eta_0 = 4.38$, and $\beta = 0.012$.

In this dissertation, the RNG $k - \varepsilon$ model will be used to close the PSPM or the MFM. In the case of PSPM, let $\alpha_i = 1$, and then the above model will reduce to that for single phase flows. In the case of MFM, the above model will be used for the continuous phase only while the dispersed phases will be regarded as laminar flows.

2.4 Population balance equation

The MFM describes droplets of fixed size. To take into account the change in droplet size caused by condensation or evaporation and predict the evolution of droplet size distribution (DSD), a PBE must be coupled with the MFM. Because of the relatively low volume fraction of the respiratory droplets in the exhaled breath [28], their collision, aggregation, and breakup are not considered [174, 175]. Then, the PBE for a univariate DSD, $n(t,\mathbf{x},\xi)$, without aggregation and breakup can be written as [147]:

$$\frac{\partial n(\xi)}{\partial t} + \nabla \cdot [\mathbf{U}(\xi)n(\xi)] + \frac{\partial}{\partial \xi} [G(\xi)n(\xi)] = 0, \tag{2.40}$$

where the scalar ξ is the internal coordinate, representing the interested property of the dispersed phase, such as size, volume, or temperature. The velocity $\mathbf{U}$ is either independent or dependent on ξ. In the first case, droplets of different sizes at a given location move with the same velocity. This treatment is suitable for the droplets distributed in a narrow size range. In the second case, the monokinetic assumption is adopted due to the neglect of interactions between the droplets. Therefore, at a specific location, droplets of the same size will move with the same velocity while

those of different sizes can have different velocities. This case is suitable for droplets whose sizes vary in a wide range. The variable $G = \mathrm{d}\xi/\mathrm{d}t$ is the change rate of the internal coordinate (or drift rate) due to condensation and evaporation.
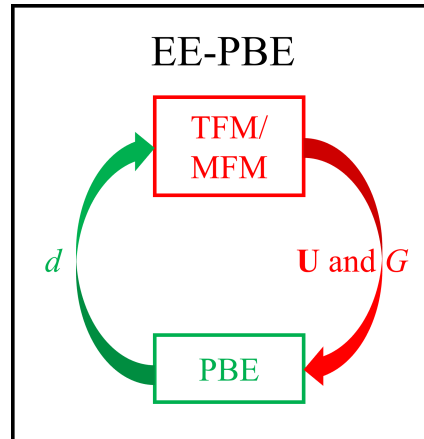
Fig. 2.3 The coupling method between the E-E approach and PBE.

In the coupling of PBE and MFM as shown in Figure 2.3, the PBE is used to trace the evolution of the DSD while the MFM is used to describe the movement of the droplets under interactions with the surrounding air flows. Therefore, the MFM should provide the velocity $\mathbf{U}$ and the drift rate G for the PBE, and the PBE should provide the DSD to the MFM. In the MFM, one dispersed phase generally requires only one diameter to calculate the interphase models at a given location. As a result, the DSD should be converted to one or several representative diameters. In this study, the sectional method (SM) and the quadrature method of moments (QMOM) will be adopted to solve the PBE to trace the transmission and evaporation of the respiratory droplets. Correspondingly, different DSD conversion methods will be used. The details are presented in the following sections.

2.4.1   Sectional method

The PBE can be solved by using the SM, where the space of the internal coordinate is discretized into a number of intervals, and the equations for the number density of droplets belonging to each interval are solved. It should be noted that the droplets may have the same velocity for all intervals, or have a different velocity for each interval or each group of intervals. As a result, the SM can be used to trace the
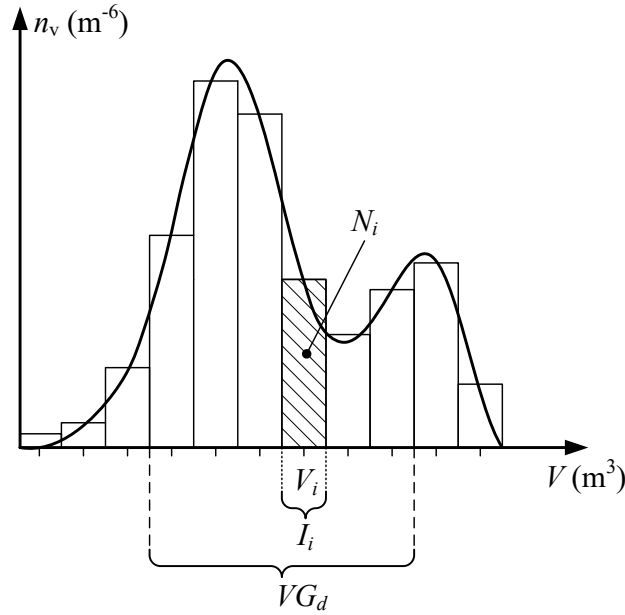
Fig. 2.4 The division of the internal coordinate of MUSIG method.

evolution of respiratory droplets moving with the same or different velocities at one location.

As shown in Figure 2.4, for a volume-based DSD $n_v(t,\mathbf{x},V)$, the SM divides the space of internal coordinate V into M fixed intervals (classes or sections), and a representative volume V_i $(i = 1, 2, \ldots, M)$ is assigned to each interval. With V_i, the ith interval I_i can be written as $I_i = [V_{i-1/2}, V_{i+1/2}]$. Integrating $n_v(t,\mathbf{x},V)$ over I_i results in the ith number concentration N_i, representing the number of droplets belonging to the ith interval per unit volume, as:

$$N_i = \int_{V_{i-1/2}}^{V_{i+1/2}} n_v dV, \tag{2.41}$$

and the volume fraction of droplets belonging to the ith interval, $\alpha_{d,i}$, can be defined as:

$$\alpha_{d,i} = N_i V_i. \tag{2.42}$$

Additionally, the fraction of the ith interval, f_i, can be defined as:

$$f_i = \frac{\alpha_{d,i}}{\alpha_d}, \tag{2.43}$$

where $\alpha_d = \sum_{j=1}^{M} \alpha_{d,j}$ is the volume fraction for all droplets. Then, we have:

$$\alpha_d f_i = N_i V_i \qquad (2.44)$$

For the volume-based DSD $n_v(t, \mathbf{x}, V)$, integrating Eq. (2.40) over the ith interval I_i with respect to the internal coordinate V and substituting N_i with f_i using Eq. (2.44) results in the following equation [148]:

$$\frac{\partial}{\partial t}(\alpha_d \rho_d f_i) + \nabla \cdot (\alpha_d \rho_d \mathbf{U}_{d,i} f_i) + V_i \rho_d (G_v n_v)\Big|_{V_{i-1/2}}^{V_{i+1/2}} = 0, \qquad (2.45)$$

where $\mathbf{U}_{d,i}$ is the velocity by which the droplets belonging to the ith interval is transported in the physical space; and $G_v = dV/dt$ is the volume change rate.

The third term in the left-hand side (LHS) of Eq. (2.45) is the drift term and it can be approximated using an upwind formulation [148]. As shown in Figure 2.5a, when evaporation happens ($G_v \leq 0$), if $i = 1$,

$$V_1 \rho_d (G_v n_v)\Big|_{V_{1/2}}^{V_{3/2}} = V_2 \rho_d \frac{N_2}{V_2 - V_1} G_{v,2}, \qquad (2.46)$$

if $1 < i < M$,

$$V_i \rho_d (G_v n_v)\Big|_{V_{i-1/2}}^{V_{i+1/2}} = V_i \rho_d \frac{N_{i+1}}{V_{i+1} - V_i} G_{v,i+1} - V_i \rho_d \frac{N_i}{V_i - V_{i-1}} G_{v,i}, \qquad (2.47)$$

and if $i = M$,

$$V_N \rho_d (G_v n_v)\Big|_{V_{M-1/2}}^{V_{M+1/2}} = -V_M \rho_d \frac{N_M}{V_M - V_{M-1}} G_{v,M}, \qquad (2.48)$$

When condensation happens ($G_v > 0$), as shown in Figure 2.5b, if $i = 1$,

$$V_1 \rho_d (G_v n_v)\Big|_{V_{1/2}}^{V_{3/2}} = V_1 \rho_d \frac{N_1}{V_2 - V_1} G_{v,1}, \qquad (2.49)$$

if $1 < i < M$,

$$V_i \rho_d (G_v n_v)\Big|_{V_{i-1/2}}^{V_{i+1/2}} = V_i \rho_d \frac{N_i}{V_{i+1} - V_i} G_{v,i} - V_i \rho_d \frac{N_{i-1}}{V_i - V_{i-1}} G_{v,i-1}, \qquad (2.50)$$

$G_v<0$, evaporation happens

$V_{-1/2}$ V_1 $V_{3/2}$ V_2 V_{i-1} $V_{i-1/2}$ V_i $V_{i+1/2}$ V_{i+1} V_{N-1} $V_{N-1/2}$ V_N $V_{N+1/2}$

(a)

$G_v>0$, condensation happens

$V_{-1/2}$ V_1 $V_{3/2}$ V_2 V_{i-1} $V_{i-1/2}$ V_i $V_{i+1/2}$ V_{i+1} V_{N-1} $V_{N-1/2}$ V_N $V_{N+1/2}$

(b)
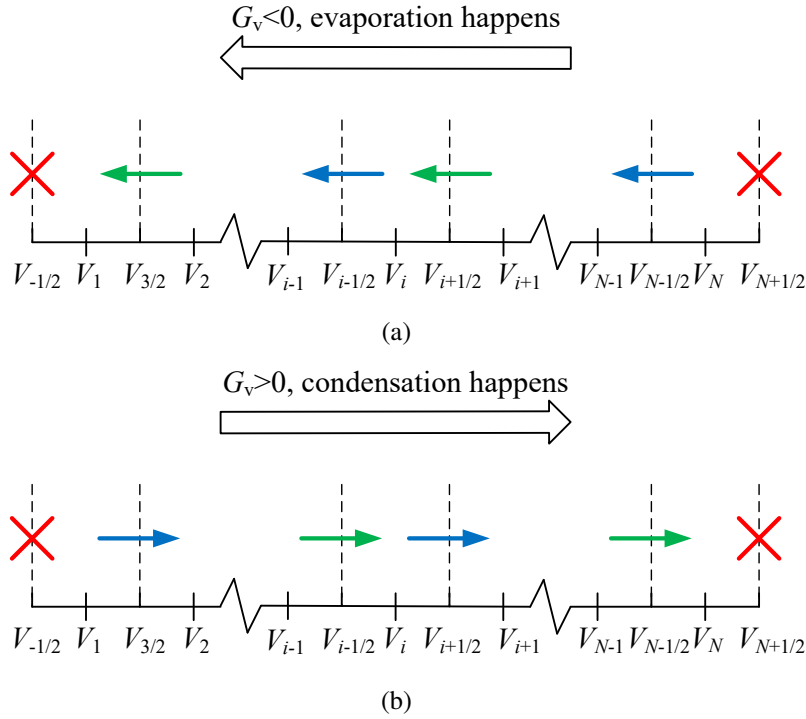
Fig. 2.5 The closures for the drift term: (a) evaporation ($G_v < 0$); (b) condensation ($G_v > 0$).

and if $i = M$,

$$V_M\rho_d(G_v n_v)\Big|_{V_{M-1/2}}^{V_{M+1/2}} = -V_M\rho_d\frac{N_{M-1}}{V_M - V_{M-1}}G_{v,M-1}. \qquad (2.51)$$

It can be noted that the total number of droplets is conserved. When evaporation happens, no droplet will disappear but just accumulate in the first interval for the smallest droplets. Similarly, during condensation, no droplet will appear and just accumulate in the last interval for the largest droplets.

To solve Eq. (2.45), the velocity and the volume change rate of the ith interval, $\mathbf{U}_{d,i}$ and $G_{v,i}$ are required, which can be obtained by coupling the SM with the MFM. When assuming that the droplets of different sizes move with the same velocity, all the droplets can be naturally regarded as one dispersed phase. Since there is only one disperse phase, the disperse phase velocity $\mathbf{U}_d$ and the interphase mass transfer rate $\dot{m}_d$ can be obtained by solving the TFM. Then, $\mathbf{U}_{d,i} = \mathbf{U}_d$ for all intervals, and

$\dot{m}_d$ is converted to $G_{v,i}$ using a surface-weighted method as:

$$G_{v,i} = -\frac{\dot{m}_d A_i}{\rho_d \sum_{j=1}^{M} N_j A_j}, \tag{2.52}$$

where $A_i = 6V_i/d_i$ is the representative surface area of the ith interval.

Meanwhile, to capture the changes in the droplet dynamics caused by their size changes, the PBE should provide the TFM with the local value of the Sauter mean diameter as:

$$d_d = \frac{1}{\sum_{i=1}^{M} \frac{f_i}{d_i}}. \tag{2.53}$$

The Sauter mean diameter is used to represent the DSD and is used as the effective size of the disperse phase to evaluate the drag force and the rates of mass and heat transfer as in Section 2.2.2.

At each iteration during a time step of the simulation, the PBE is solved first to update d_d, with which the TFM is solved to update $\mathbf{U}_d$ and $G_{v,i}$. The iterations stop when a convergence criterion or iteration number is reached.

The SM can also be used to trace the evolution of droplets of different sizes moving with different velocities. By introducing the concept of velocity group [176], the SM becomes the multiple size group (MUSIG) method.

As shown in Figure 2.4, in the MUSIG method, the M intervals are further divided into L velocity groups. Each velocity group has its own velocity. As a result, droplets of different velocity groups have different sizes and may move with different velocities. It should be noted the MUSIG method implies that the droplets are monokinetic, namely, at one location, droplets of the same velocity group (or belonging to the same size ranges) only have one velocity. This is reasonable because it is a dilute system.

The lth velocity group VG_l contains L_l successive intervals ($l = 1, 2, \ldots, L$), namely,

$$VG_l = \left\{ I_{L_{\text{pre},l}+1}, I_{L_{\text{pre},l}+2}, \ldots, I_{L_{\text{pre},l}+L_l} \right\}, \tag{2.54}$$

where $L_{\text{pre},l} = \sum_{j=0}^{l-1} L_j$ with $L_0 = 0$ is the total number of intervals of the previous $l-1$ velocity groups. Similar to Eq. (2.45), the PBE Eq. 2.40 for $I_i \in VG_l$ can be

written as:

$$\frac{\partial}{\partial t}\left(\alpha_{d,l}\rho_d f_i\right) + \nabla \cdot \left(\alpha_{d,l}\rho_d \mathbf{U}_{d,l} f_i\right) + V_i \rho_d (G_{v,l} n_v)\Big|_{V_{i-1/2}}^{V_{i+1/2}} = 0, \qquad (2.55)$$

where $\alpha_{d,l}$ is the volume fraction for all droplets belonging to VG_l; the definition for the fraction of I_i is changed to $f_i = \alpha_{d,i}/\alpha_{d,l}$, so that we have $\alpha_{d,l} f_i = N_i V_i$; $\mathbf{U}_{d,l}$ is the velocity of VG_l; and $G_{v,l}$ is the volume change rate of VG_l.

To solve Eq. (2.55), the MUSIG method is coupled with the MFM. Each velocity group is regarded as a dispersed phase. Therefore, the MFM for one continuous phase and L disperse phases will be solved to obtain $\mathbf{U}_{d,l}$ and $G_{v,l}$. Meanwhile, the DSD of each velocity group will be used to calculate the Sauter mean diameter as the effective size for the dispersed phase of the MFM. Finally, the solving procedure is the same as the previous case: PBE is solved first for dispersed phase diameters and followed by solving MFM for velocities and volume change rates.

In this dissertation, OpenFOAM v8 [162] is adopted for the sectional method, where the MFM and the MUSIG method have been implemented. However, the evaporation model was not combined with the MUSIG method in OpenFOAM v8. Therefore, necessary modifications, passing the mass transfer rate $\dot{m}_d$ obtained by Eq. (2.18) to calculate the volume change rate $G_{v,i}$ as in Eq. (2.52), were made to the codes to implement the coupling. The modified solver will be denoted as "SM-solver" in the following sections.

2.4.2   QMOM for PBE: size-independent droplets velocity

The PBE can also be solved by the quadrature method of moments (QMOM). In this case, the evolution of integral properties of the DSD, i.e., moments, is evaluated. The diameter-based DSD, $n_d(t,\mathbf{x},d)$, rather than $n_v(t,\mathbf{x},V)$ is adopted here to capture accurately the lowest order moments with respect to size and to avoid the too small value of higher order moments.

In QMOM, $n_d(t,\mathbf{x},d)$ can be approximated using N quadrature nodes (Figure 2.6) as:

$$n_d(t,\mathbf{x},d) \approx \sum_{p=1}^{N} w_p(t,\mathbf{x}) \delta(d - d_p(t,\mathbf{x})), \qquad (2.56)$$
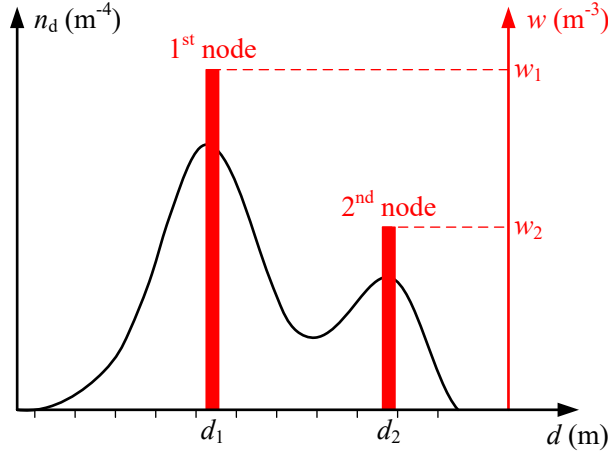
Fig. 2.6 The quadrature method of moments.

where $w_p(t, \mathbf{x})$ and $d_p(t, \mathbf{x})$ are the weight and abscissa of the node p, and δ denotes the Dirac delta function.

The kth order moment of the DSD, M_k, can be calculated as:

$$M_k = \int_0^{+\infty} d^k n_{\mathrm{d}}(d) \mathrm{d}d \approx \sum_{p=1}^{N} w_p d_p^k. \qquad (2.57)$$

The above equation implies that the N unknown weights and the N unknown abscissas can be determined by solving the set of nonlinear equations for the first $2N$ moments as:

$$\begin{cases} M_0 = w_1 + w_2 + \cdots + w_N, \\ M_1 = w_1 d_1 + w_2 d_2 + \cdots + w_N d_N, \\ \quad \vdots \\ M_{2N-1} = w_1 d_1^{2N-1} + w_2 d_2^{2N-1} + \cdots + w_N d_N^{2N-1}. \end{cases} \qquad (2.58)$$

The above set of nonlinear equations can be solved using the Wheeler algorithm [177] or its adaptive version [178]. The $2N$ moments can be obtained by solving their transport equations derived from the PBE Eq. (2.40).

In the simplest case, the droplets of different sizes are assumed to share the same velocity field $\mathbf{U}_{\mathrm{d}}$, i.e., $\mathbf{U} = \mathbf{U}_{\mathrm{d}}(t, \mathbf{x})$ is independent of the internal coordinate d. Then, multiplying Eq. (2.40) with d^k, and integrating it with respect to d yields the

transport equation for M_k as:

$$\frac{\partial M_k}{\partial t} + \nabla \cdot (\mathbf{U}_{\mathrm{d}} M_k) + \int_0^{+\infty} d^k \frac{\partial}{\partial d}(G_{\mathrm{d}} n_{\mathrm{d}}) \mathrm{d}d = 0, \qquad (2.59)$$

where $G_{\mathrm{d}} = \mathrm{d}d/\mathrm{d}t$ is the diameter change rate.

The third term in the LHS of Eq. (2.59) is the drift term and is treated following the idea of Yuan et al. [179], namely, using a time-splitting method to solve the moment transport equations and modeling the drift term by updating the abscissas. The abscissas are updated as follows:

$$d_p(t + \Delta t) = d_p(t) - G_{\mathrm{d},p} \Delta t, \qquad (2.60)$$

where $G_{\mathrm{d},p}$ is the diameter change rate for pth quadrature node; and Δt is the time step.

Additionally, the respiratory droplets generally consist of the volatile water, and the non-volatile biological materials, such as the virus. In this dissertation, to trace the dispersion of the non-volatile materials, the respiratory droplets are not allowed to fully evaporate but left droplet nuclei. This is implemented by specifying a minimum droplet size $d_{\min}$ for the quadrature node abscissa d_p. If $d_p(t + \Delta t) < d_{\min}$, then let $d_p(t + \Delta t) = d_{\min}$. This treatment of the quadrature node abscissas avoids the disappearance of droplets due to full evaporation and the droplets, owning size of $d_{\min}$, remain traceable. In the following simulations, $d_{\min}$ is set as 1 μm because most of the droplet nuclei distribute in a range of 1 μm to 2 μm [26, 30]. Meanwhile, $d_{\min} = 1$ μm is representative. As mentioned in Chapter 1, droplets ranging from 0.7 μm to 3.5 μm, having similar behaviors, tend to completely follow the airflow [82–86, 80]. Moreover, to be consistent with the evaporation model of Section 2.2.2, the volumetric mass transfer coefficient k_{c} is set as 0 when $d_p(t + \Delta t) \leq d_{\min}$.

To solve Eq. (2.59), $\mathbf{U}_{\mathrm{d}}$ and G_{d} are required. Similar to the method used in the SM, the droplets of different sizes, owning the same velocity, can be regarded as the dispersed phase of the TFM. Then, the TFM provides Eq.2.59 with the disperse phase velocity as $\mathbf{U}_{\mathrm{d}}$ and the interphase mass transfer rate $\dot{m}_{\mathrm{d}}$ to calculated the diameter change rate for the pth node, $G_{\mathrm{d},p}$, as (detailed derivation can be found in Appendix A):

$$G_{\mathrm{d},p} = \frac{2}{\rho_{\mathrm{d}} \pi d_p M_1} \dot{m}_{\mathrm{d}}. \qquad (2.61)$$

Meanwhile, the PBE provides the TFM with the mean disperse phase diameter (Sauter mean diameter) as:

$$d_{\mathrm{d}} = \frac{M_3}{M_2},\qquad\qquad(2.62)$$

similarly, d_{d} representing the DSD is used in the interphase models of the TFM.

The detailed algorithm can be found in Appendix B. The solver for this algorithm is developed based on OpenFOAM v2106 [180] and its module OpenQBMM v7 [181], which provides the tools and libraries for multiphase flows and QBMM. This solver can be used to model the droplets moving with the same velocity on varied sizes, and it will be denoted as the "mono-solver" in the following sections.

2.4.3   QMOM for PBE: size-dependent droplets velocity

To model the droplets moving with different velocities on varied sizes, the generalized population balance equation (GPBE) for the diameter-velocity joint DSD, $f_{\mathrm{d}}(t, \mathbf{x}, d, \mathbf{v})$ is generally required, which, however, is relatively complex to solve. In this study, to simplify the problem, the monokinetic assumption is employed:

$$f_{\mathrm{d}}(t, \mathbf{x}, d, \mathbf{v}) = n_{\mathrm{d}}(t, \mathbf{x}, d)\delta\left(\mathbf{v} - \mathbf{U}(t, \mathbf{x}, d)\right),\qquad\qquad(2.63)$$

where $n_{\mathrm{d}}(t, \mathbf{x}, d)$ is the diameter-based DSD and $\mathbf{U}(t, \mathbf{x}, d)$ is the droplet velocity conditioned on the droplet size d.

The monokinetic assumption is equivalent to assuming that the droplets with the same internal coordinate d move with the same velocity. With this assumption, the GPBE reduces to the PBE in Eq. (2.40) where the velocity is $\mathbf{U} = \mathbf{U}(t, \mathbf{x}, d)$ [182]. Similar to Section 2.4.2, the transport equation of the kth order size moment M_k can be obtained from Eq. (2.40) as follows:

$$\frac{\partial M_k}{\partial t} + \nabla \cdot \boldsymbol{\mathcal{U}}_k + \int_0^{+\infty} d^k \frac{\partial}{\partial d}(G_{\mathrm{d}} n_{\mathrm{d}})\mathrm{d}d = 0,\qquad\qquad(2.64)$$

where $\boldsymbol{\mathcal{U}}_k = \int_0^{+\infty} d^k n_{\mathrm{d}}(d)\mathbf{U}(d)\mathrm{d}d$ is the kth order velocity moment, which cannot be further simplified, as $\mathbf{U}(t, \mathbf{x}, d)$ depends on the internal coordinate d.

To solve for $\mathbf{U}(t, \mathbf{x}, d)$, the transport equations of velocity moments are introduced following the idea of Heylmun et al. [149]. The equations can be obtained by first multiplying Eq. (2.40) by $d^k \mathbf{U}(d)$ and then integrating it with respect to the internal

coordinate d:

$$\frac{\partial \mathscr{U}_k}{\partial t} + \nabla \cdot \mathscr{P}_k + \int_0^{+\infty} d^k \frac{\partial}{\partial d}(G_d n_d \mathbf{U})\mathrm{d}d - \int_0^{+\infty} d^k \mathbf{A} n_d \mathrm{d}d = 0, \qquad (2.65)$$

where $\mathscr{P}_k = \int_0^{+\infty} d^k n_d(d)\mathbf{U}(d) \otimes \mathbf{U}(d)\mathrm{d}d$; and $\mathbf{A}(t,\mathbf{x},d) = \mathrm{d}\mathbf{U}(t,\mathbf{x},d)/\mathrm{d}t$ is the acceleration vector. The relative velocity $\mathbf{V}(t,\mathbf{x},d) = \mathbf{U}(t,\mathbf{x},d) - \mathbf{U}_d(t,\mathbf{x})$ is introduced, where $\mathbf{U}_d(t,\mathbf{x})$ is the average velocity of the disperse phase. Then,

$$\mathscr{V}_k = \int_0^{+\infty} d^k n_d(d)\mathbf{V}(d)\mathrm{d}d = \mathscr{U}_k - M_k \mathbf{U}_d. \qquad (2.66)$$

Similarly, $\mathscr{P}_k$ can be divided into two parts: the relative part $\mathscr{P}_{k,r}$ as:

$$\mathscr{P}_{k,r} = \int_0^{+\infty} d^k n_d(d)\mathbf{V}(d) \otimes \mathbf{U}(d)\mathrm{d}d, \qquad (2.67)$$

and the average part $\mathscr{P}_{k,a}$ as:

$$\mathscr{P}_{k,a} = \int_0^{+\infty} d^k n_d(d)\mathbf{U}_d \otimes \mathbf{U}(d)\mathrm{d}d = \mathbf{U}_d \otimes \mathscr{U}_k. \qquad (2.68)$$

Finally, Eq. (2.64) and Eq. (2.65) can be written as:

$$\frac{\partial M_k}{\partial t} + \nabla \cdot \mathscr{V}_k + \nabla \cdot (\mathbf{U}_d M_k) + \int_0^{+\infty} d^k \frac{\partial}{\partial d}(G_d n_d)\mathrm{d}d = 0, \qquad (2.69)$$

$$\frac{\partial \mathscr{U}_k}{\partial t} + \nabla \cdot \mathscr{P}_{k,r} + \nabla \cdot \mathscr{P}_{k,a} + \int_0^{+\infty} d^k \frac{\partial}{\partial d}(G_d n_d \mathbf{U})\mathrm{d}d - \int_0^{+\infty} d^k \mathbf{A} n_d \mathrm{d}d = 0. \qquad (2.70)$$

When considering N quadrature nodes, there are N unknown weights w_p, N unknown abscissas d_p, and N unknown quadrature node velocity vectors (containing $3N$ unknown velocity components). Therefore, $2N$ size moments, namely, M_k where $k = 0, 1, 2, ..., 2N - 1$ are required to obtain w_p and d_p. Additionally, N velocity moment vectors, namely, $\mathscr{U}_k$ where $k = 0, 1, 2, ..., N - 1$ are required to obtain the pth quadrature node velocity $\mathbf{U}_p = (U_{x,p}, U_{y,p}, U_{z,p})$.

The transport equations of size moments and velocity moments, as in Eq. (2.69) and Eq. (2.70), are solved by using a time-splitting method, where the drift term for the droplet size and the velocity acceleration term are modeled by updating the

diameter and velocity abscissas as in Section 2.4.2 and in the work of Heylmun et al. [149], respectively.

For the coupling of PBE and TFM, the droplets are moving at different velocities, therefore, the interfacial models should consider the interactions with each quadrature node. Take the drag force for example, in this case, the drag force for the disperse phase in the momentum equations is written as:

$$\mathbf{F}_{\mathrm{D,d}} = \sum_{p=0}^{N-1} \mathbf{F}_{\mathrm{D,d},p} = \sum_{p=0}^{N-1} \left(\frac{3}{4} C_{\mathrm{D},p} \mathrm{Re}_p \frac{\alpha_{\mathrm{d},p}\rho_{\mathrm{c}} \nu_{\mathrm{c}}}{d_p^2} (\mathbf{U}_{\mathrm{c}} - \mathbf{U}_p) \right), \qquad (2.71)$$

where $\mathbf{F}_{\mathrm{D,d},p}$ is the drag force acted on the pth node, $C_{\mathrm{D},p}$ and Re_p are the drag coefficient and Reynolds number calculated using the pth node velocity $\mathbf{U}_p$, $\alpha_{\mathrm{d},p} = (\alpha_{\mathrm{d}} w_p d_p^3)/M_3$ is the volume fraction of the pth node. Other interfacial models are calculated in a similar way, replacing the velocities, volume fractions, and diameters with those of the pth node and making a summation. Therefore, the PBE should provide the TFM with $\alpha_{\mathrm{d},p}$, d_p and $\mathbf{U}_p$ for the calculation of interfacial models, while the TFM should provide PBE with $\mathbf{U}_{\mathrm{d}}$ for the relative velocity and the interfacial mass transfer rate of the pth node $\dot{m}_p$ for $G_{\mathrm{d},p}$ as (detailed derivation can be found in Appendix A):

$$G_{\mathrm{d},p} = \frac{2}{\rho_{\mathrm{d}} \pi w_p d_p^2} \dot{m}_p. \qquad (2.72)$$

The detailed algorithm can be found in Appendix C. The solver for this algorithm is developed based on the tools and libraries of OpenFOAM v2106 and OpenQBMM v7. This solver can be used to model the droplets moving with different velocities on varied sizes and will be denoted as "poly-solver" in the following sections.

2.5   Numerical solution

The above models are implemented within the frame of OpenFOAM. To deal with the coupling between the pressure and the velocity for the unsteady simulations, the PIMPLE algorithm of OpenFOAM is adopted. It is the combination of PISO (pressure-implicit with splitting of operators) and SIMPLE (semi-implicit method for pressure-linked equations) [183, 184]. As for the steady simulations, the SIM-PLE algorithm is adopted. The convergence criteria are specified as 1×10^{-4} or

lower values. For example, the criterion for pressure or velocity is 1×10^{-4}. For volume fraction or moment, smaller values, such as 1×10^{-8}, are used to ensure the convergence.

As for the numerical schemes, the first-order upwind scheme is adopted to discretize the equations of the EE-PBE approach. This is to avoid the problem of realizability when using the QMOM to solve the PBE. Using higher-order schemes to discretize the moment transport equations may result in unreasonable moments that cannot be inverted to quadrature nodes. Therefore, the first-order upwind scheme is adopted to discretize equations of moments for numerical stability. Meanwhile, considering consistency, this scheme is also adopted for equations of other variables.

For the Eulerian approaches not involving PBE, such as the PSPM or the TFM, second-order schemes are adopted. The *limitedLinear* scheme of OpenFOAM is used to discretize the advection terms. It is a second-order total variation diminishing (TVD) scheme based on Sweby limiter [185]. Furthermore, the second-order central differencing scheme, named *linear* in OpenFOAM, is adopted to discretize the diffusion terms.

2.6   Summary

In this chapter, the different Eulerian approaches are presented:

- in the pseudo-single-phase model (PSPM), the dispersed droplets are modeled as solute dissolved in the same phase with the air, so this method is only suitable for the monodispersed small-size droplets that completely follow the airflow;

- in the multi-fluid model (MFM), the dispersed droplets are considered as additional continuums interpenetrating with the air phase. The Navier-Stokes equations containing interphase interaction terms are solved for the continuous and the dispersed phases, respectively. Therefore, this model can be used for the monodispersed droplets that may move at a velocity different from the air velocity;

- in the Eulerian-Eulerian approach and population balance equation (EE-PBE) coupled approach, the E-E approach provides dispersed phase velocities and

evaporation rate for the PBE while the PBE provides the E-E approach with
the dispersed phase diameters. Two different PBE solving methods, sectional
method (SM) and quadrature method of moments (QMOM), are presented.
The EE-PBE coupled approaches can be used to trace the transmission and
evaporation of monodispersed or polydispersed droplets.

Codes are developed for the above Eulerian approaches based on the open-source
software OpenFOAM and its module OpenQBMM. The details are listed in Table
2.2.

Table 2.2 List of the adopted solvers in this study.

Name	Version	Developed?	Method	Application
PSPM-solver	OpenFOAM v2106	Yes	PSPM	small-size, monodispersed
TFM-solver	OpenFOAM v2106	No	TFM	monodispersed
SM-solver	OpenFOAM v8	Yes	MFM-PBE, MUSIG-SM	mono-/poly-dispersed, evaporating
mono-solver	OpenFOAM v2106, OpenQBMM v7	Yes	TFM-PBE, QMOM	monodispersed, evaporating
poly-solver	OpenFOAM v2106, OpenQBMM v7	Yes	monokinetic TFM-PBE QMOM	mono-/poly-dispersed, evaporating

Chapter 3

Verification and validation

As discussed in previous sections, polydispersity and evaporation are important features of respiratory droplets and can significantly affect their space and time evolution. Therefore, the ability of the developed EE-PBE approach to deal with these features is assessed systematically in this section, by using test cases of increasing complexity. The evaporation model is validated first using the reported temporal evolution of the diameter of a single droplet (Section 3.1) and freely falling droplets (Section 3.2). Then, the reliability of the EE-PBE approach to simulate the non-evaporating particle flows is evaluated by using two test cases: one concerning the evolution of the exhaled breath of respiratory activities (Section 3.3) and the other concerning the flow field and the particle dispersion in a chamber (Section 3.4). Finally, the EE-PBE approach is applied in the transport of evaporating cough droplets in a 3D chamber and compared with numerical results in the literature (Section 3.5).

3.1 Verification of the evaporation model

Evaporation is an important feature of the expelled respiratory droplets. After evaporation, the droplets lose their weight and may present behaviors different from those with their original sizes. This is particularly significant for small droplets. They quickly evaporate into nuclei, suspend in the air, and may cause infection in a larger range. However, many factors affect the evaporation process, such as the composition and velocity of the droplets, and the relative humidity and temperature

of the environment. An accurate droplet evaporation model is essential to numerical studies on the transmission of respiratory droplets. Therefore, the evaporation model is first validated using the experimental data in the literature.

In their experimental study, Chaudhuri et al. [186] adopted an ultrasonic levitator to study the evaporation of pure water droplets with an initial diameter equal to 346 μm and 647 μm, and saltwater droplets with an initial diameter equal to 339 μm and 593 μm. The d^2-law [187] was observed for the pure water droplets, while the evaporation of the saltwater droplets showed a deviation from the d^2-law because the presence of the salt made the evaporation slower. Basu et al. [188] investigated the evaporation of droplets having different compositions using an acoustic levitator. Droplets consisting of pure water, saltwater, saltwater with nanoparticles, and human saliva were studied, respectively. They found that the evaporation rate of pure water is the highest and that of human saliva is the lowest. Stiti et al. [189] studied the evaporation of saliva droplets. In addition to the d^2-law, they also found the formation of a solid skin due to crystallization. Lieber et al. [190] adopted the acoustic levitator to investigate the evaporation of pure water droplets and saliva droplets. They found that the initial evaporation rate of both droplets was nearly identical and, consequently, the first stage of the evaporation process of saliva droplets can be represented by the evaporation of pure water. These experimental studies reveal the temporal evolution of the droplet sizes during evaporation and build a foundation for the development and validation of the evaporation model.

In this study, the evaporation of respiratory droplets is represented by that of pure water droplets according to the conclusion of Lieber et al. [190]. Their experiment is adopted to validate the evaporation model.

3.1.1 Case description and numerical method

In the experiment of Lieber et al. [190], a single droplet was injected into the process chamber, levitated in the air by an acoustic levitator, and evaporated at constant temperature and relative humidity. The evaporation process of the droplet was recorded by using microscopic imaging. Additionally, special measures were taken to minimize the influence of the experimental setup, such as using a high resonance frequency of 100 kHz to reduce the effect of acoustic streaming.

Since the experiment recorded the evaporation of a single droplet, the evaporation model of the MFM for a cloud of droplets in Section 2.2.2 must be rewritten for a single droplet. This can be obtained by setting N_i in Eq. (2.42) equal to 1 m^{-3}, which means that there is only one droplet in the unit volume. Then, substituting the obtained volume fraction for one droplet into Eq. (2.19), the mass transfer coefficient for a single droplet, k_d, can be written as:

$$k_d = \pi d_d \text{Sh} D_c. \tag{3.1}$$

Similarly, the heat transfer coefficients in the continuous phase side (Eq. (2.27)) for a single droplet can be written as:

$$h_c = \pi d_d \text{Nu} \kappa_c, \tag{3.2}$$

and that in the dispersed phase side (Eq. (2.29)) can be written as:

$$h_d = 10\pi d_d \kappa_d. \tag{3.3}$$

With the above coefficients, the mass and energy balance equation for a single stationary droplet can be written as:

$$\frac{dm_d}{dt} = \dot{m}_d = \rho_c k_d (Y_f - Y_{H_2O}), \tag{3.4}$$

$$\frac{dm_d E_d}{dt} = Q_{fd} - \dot{m}_d E_{fd} = h_d(T_f - T_d) - \dot{m}_d E_{fd}, \tag{3.5}$$

where m_d is the mass of the droplet; and E_d is the internal energy of the droplet.

The simplified evaporation model is a system of two ordinary differential equations (ODEs). This is solved by using a developed Python code, where T_f is iteratively solved first as in Section 2.2.2, and then Eq. (3.4) and Eq. (3.5) are solved.

For the verification, an ambient temperature (T_g) of 296.15 K and a relative humidity of 50% were adopted and kept constant during the simulation, as the experimental setups [190]. The initial temperature of the droplet (T_d) was also 296.15 K and the initial diameter (d_0) was 215 μm. The thermal properties of the droplet and the surrounding air can be found in Appendix D.

3.1.2 Results and discussion

Figure 3.1 shows the temporal evolution of the normalized surface of the water droplet. A good agreement between the predicted and experimental results can be observed. Some deviations, no larger than 10% from the measurement, appear after the droplet loses 50% surface ($d^2/d_0^2 < 0.5$), which might be caused by the acoustic streaming [189] or the instability [190] induced by the acoustic field. An approximately linear evolution of the normalized surface d^2/d_0^2, known as the classical d^2-law, is observed. This is because when the forced and natural convection is small, the surface of an evaporating droplet decreases linearly at a rate depending on ambient properties [191]. Therefore, we can conclude that the evaporation model and the thermal physical property models are reliable for predicting the diameter changes of a pure water droplet.
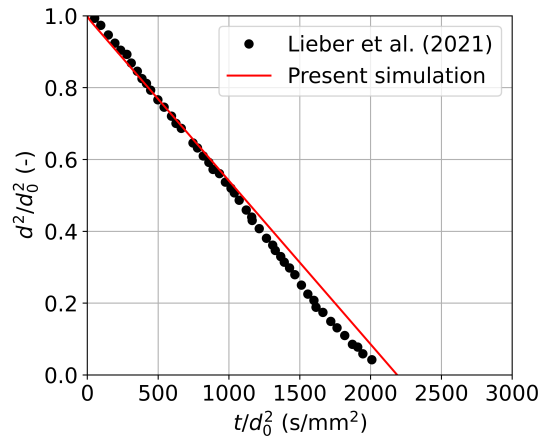
Fig. 3.1 Temporal evolution of the normalized surface of a water droplet.

3.2 Validation of the evaporation model of the PBE

After the validation of the evaporation model for a single stationary droplet, its ability to trace the size changes of a cloud of evaporating droplets within the frame of the E-E approach and PBE coupled approach should be assessed. Therefore, the two PBE-solving methods, SM and QMOM, are validated with the data in the literature.

In the classic work of Wells [18], the d^2-law was adopted to predict the lifetime of the evaporating pure water droplets. The relationship between droplet diameters and

falling time as well as evaporation time was presented. Redrow et al. [192] used the numerical method to investigate the evaporation of pure water droplets of different sizes and under different relative humidities. They found that the evaporation was very fast, usually less than 0.5 s, for droplets smaller than 10 μm. The relative humidity played an important role in the droplet evaporation, namely, higher relative humidity results in slower evaporation rate. Wei and Li [193] investigated the droplet evaporation through the Lagrangian approach. The effect of droplet size, relative humidity, and relative velocity were studied. Results similar to those of Redrow et al. [192] were found. They also found that higher relative velocity between the droplets and the environment enhances evaporation. The work of Redrow et al. [192] and Wei and Li [193], covering a diameter range from 1 μm to 100 μm and showing good consistency, are widely used by researchers to validate their models [52, 99, 194–197].

Therefore, these two works are adopted in this study. To reproduce the results reported in the literature, the setups of Li et al. [52] are adopted, where the droplets are freely falling and evaporating in quiescent air.

3.2.1 Case description and numerical method

As shown in Figure 3.2, a two-dimensional (2D) chamber (length × height = 4 m × 3 m) is adopted as geometry. The droplets are initially located in the red square region, whose size is 0.2 m × 0.2 m and center is at $x = 2$ m and $z = 2$ m. The droplets are released with zero initial velocity. The initial droplet volume fraction is $\alpha_\mathrm{d} = 1 \times 10^{-6}$. This value is large enough so that the continuum assumption still holds for the EE-PBE approach meanwhile it is small enough to match the setups in the reference papers. The evaporation of droplets of two sizes, 10 μm and 100 μm, under two relative humidities of 0% and 60% are simulated, respectively. The initial droplet temperature T_d is 310.15 K and the environment temperature T_c is 298.15 K as in Redraw et al. [192].

For the simulation, the SM-solver and the QMOM mono-solver are used and compared. A uniform grid with 30000 square cells (200×150) is adopted here. Both phases are regarded as laminar due to their low velocities. The thermal physical property models are set as in Appendix D. For the SM-solver, 21 representative volumes are specified to divide the droplet size interval from the initial size to

the minimum size. For clarity, the 21 representative volumes are converted into diameters and are shown in Table 3.1. For the QMOM mono-solver, two nodes are used and four moments equations are thus solved. The initial values for the moments are reported in Table 3.2.
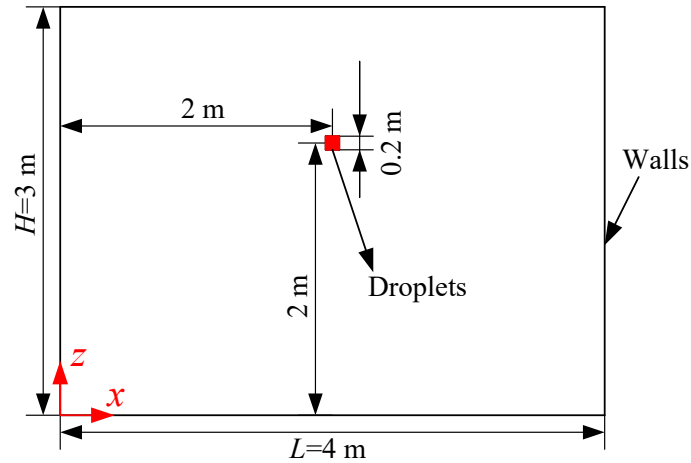
Fig. 3.2 Geometry of the 2D chamber for the case of freely falling droplets.

3.2.2   Results and discussion

In the E-L approach, droplets are tracked individually, so the droplet size changes with time caused by evaporation can be easily recorded. In the E-E approach, a cloud of droplets is tracked as a continuum. Therefore, the mean size of the droplets, calculated by Eq. (2.53) for the SM and by Eq. (2.62) for the QMOM, is used to represent the size changes caused by evaporation. Though specifying a very low initial volume fraction for the droplets ($\alpha_d = 1 \times 10^{-6}$), droplets within the cloud may have different evaporation rates due to the accumulation of water vapor in the air phase, especially for the droplets located in the center of the cloud. Therefore, the changes of the minimum mean size, representing the droplets that have the largest evaporation rate and thus are less affected by the effect of droplet cloud, are recorded and compared with the results obtained by the E-L approach in the literature.

The droplet sizes predicted by the SM and the QMOM are shown in Figure 3.3. The numerical results of both methods agree well with the literature data. It can be noted that for the 10 μm droplets, the evaporation rate predicted by the SM is a little faster than the QMOM, especially when the relative humidity is 60%.

Table 3.1 Representative volumes and initial size class fractions for the droplets of the two
sizes.

No.	$d_0 = 100\ \mu m$		$d_0 = 10\ \mu m$	
	d_i (μm)	f_i (-)	d_i (μm)	f_i (-)
1	1	0	0.1	0
2	5	0	0.5	0
3	10	0	1.0	0
4	15	0	1.5	0
5	20	0	2.0	0
6	25	0	2.5	0
7	30	0	3.0	0
8	35	0	3.5	0
9	40	0	4.0	0
10	45	0	4.5	0
11	50	0	5.0	0
12	55	0	5.5	0
13	60	0	6.0	0
14	65	0	6.5	0
15	70	0	7.0	0
16	75	0	7.5	0
17	80	0	8.0	0
18	85	0	8.5	0
19	90	0	9.0	0
20	95	0	9.5	0
21	100	1.0	10.0	1.0

Table 3.2 Initial moments for the droplets of the two sizes.

Variable	1st size	2nd size
d (µm)	10	100
α_{d} (-)	1×10^{-6}	1×10^{-6}
M_0 (m^{-3})	$1.909\,859 \times 10^{9}$	$1.909\,859 \times 10^{6}$
M_1 (m^{-2})	$1.909\,859 \times 10^{4}$	$1.909\,859 \times 10^{2}$
M_2 (m^{-1})	$1.909\,859 \times 10^{-1}$	$1.909\,859 \times 10^{-2}$
M_3 (-)	$1.909\,859 \times 10^{-6}$	$1.909\,859 \times 10^{-6}$

This might be caused by the limited number of the size classes used in the SM. Additionally, the effects of initial size and relative humidity are also presented as: smaller droplets (10 µm) evaporate faster than larger droplets (100 µm); increasing the relative humidity will reduce the evaporation rate. Therefore, the EE-PBE approach can trace the diameter changes of evaporating droplets under different conditions.
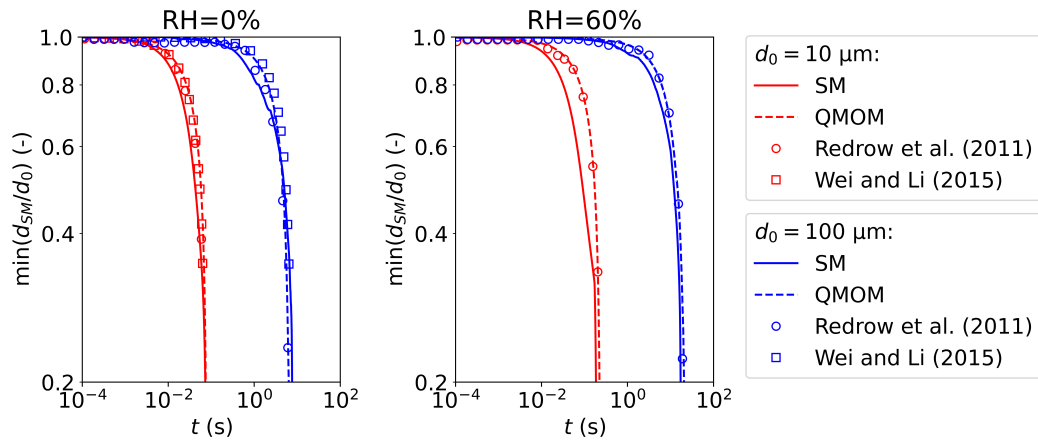

Fig. 3.3 Droplet size time evolution obtained by using SM and QMOM.

3.3 Validation of the EE-PBE approach for respiratory activity

The respiratory droplets are carried by and interact with the expelled airflow. Therefore, an accurate description of the respiratory airflow is essential for the prediction

of the dispersion and evaporation of the droplets. To assess the reliability of the EE-PBE approach in the simulations of respiratory activities, the QMOM mono-solver and the QMOM poly-solver (i.e., the solver considering the effect of size on droplet velocity) are validated against the experimental data from Wang et al. [173], where the distance traveled by the front of a sneeze jet was measured.

3.3.1   Case description and numerical method

In the experiment of Wang et al. [173], the jet was expelled from the mouth, a circular opening, of a dummy head to mimic a sneeze. The diameter of the mouth was 2 cm. A gamma function was adopted as the time-varying inlet velocity for a sneeze lasting for 0.6 seconds. The jet was seeded with non-evaporating droplets ($\rho_d = 1000 \text{ kg m}^{-3}$) and a high-speed camera was used to visualize the flow field and track the jet front. The sizes of the droplets ranged from 1 μm to 3 μm, having an average size of 2 μm. The volume fraction of the droplets was set to 4.55×10^{-6}. The temperature of the environment, jet, and droplets are identical and constant, equal to 295 K. The relative humidities of the environment and jet are also identical and constant, equal to 50%.

For the simulation, the geometry of the 3D chamber discussed in detail in Section 3.5 is adopted. Both the mono-solver and the poly-solver are used to solve the TFM and PBE to trace the evolution of the sneeze jet front with advancing time. The RNG $k - \varepsilon$ model is used for the continuous phase while the laminar flow assumption is used for the dispersed phase. During the simulation, the evaporation model is disabled to mimic the non-evaporating droplets used in the experiment. The thermal physical properties in Appendix D are used. The boundary conditions and initial fields are given as in the experiment, namely, specifying a time-varying velocity condition at the inlet, open to air at the right boundary, and no-slip conditions at other boundaries. For the setup of QMOM, two nodes are adopted, so four moment transport equations are solved. At the inlet, the moments of the DSD are calculated by using the volume fraction and the DSD from the experiment (see Table 3.3).

The traveling distance of the sneeze jet front L is extracted by setting a threshold for the dispersed phase volume fraction, α_d, and by selecting the maximum distance from the mouth where the breath is released at each time step. The threshold value is prescribed as $\alpha_d = 1 \times 10^{-10}$. It is large enough to ensure the continuum assumption

Table 3.3 Moments at the inlet for the case of sneeze jet front.

Variable	Value
α_d (-)	4.55×10^{-6}
M_0 (m^{-3})	$1.277\,276 \times 10^{12}$
M_1 (m^{-2})	$2.360\,087 \times 10^{6}$
M_2 (m^{-1})	$4.472\,296$
M_3 (-)	$8.689\,860 \times 10^{-6}$

of the EE-PBE approach. Meanwhile, it is small enough so that the movement of the sneeze jet front can be detected accurately. Therefore, particles are regarded as actually existing in the cells where $\alpha_d \geq 1 \times 10^{-10}$, and the maximum x-coordinate of those cells is the traveling distance at each time step.

3.3.2   Results and discussion

The predicted and measured temporal evolution of the sneeze jet front are shown in Figure 3.4. It can be seen that the numerical results of both solvers are very close and are in good agreement with the experimental result. This indicates that the poly-solver is reliable for the flows where the droplet size distributes in a narrow range, such as in droplet nuclei dispersion. In addition, the evolution of exhaled breath can be divided into two stages: the jet stage and the puff stage. In the early jet stage, the sneeze continues, constantly providing momentum to the exhaled jet and resulting in the self-similar behavior of $L \propto t^{1/2}$. In the late puff stage, the sneeze stops, leading to the constant momentum of the exhaled jet and the self-similar behavior of $L \propto t^{1/4}$. The different behaviors of the jet and puff stage are expected to affect the droplets' dispersion and evaporation [96], making it important to capture such features. It can be seen that the two scaling laws and their transition are accurately captured by both numerical and experimental results. Therefore, the developed mono-solver and poly-solver for the EE-PBE approach are validated against the experimental data of the sneeze and are capable of accurately predicting the two-stage evolution of the exhaled breath.
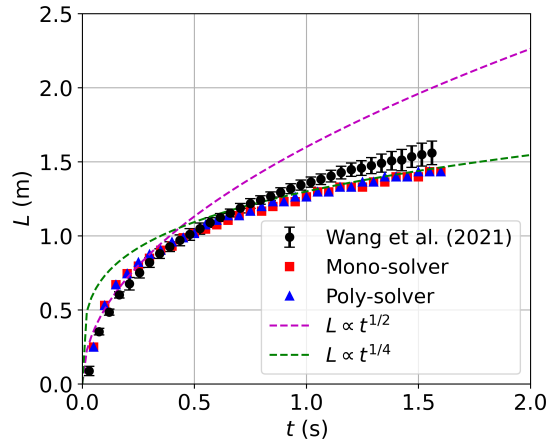
Fig. 3.4 Temporal evolution of the sneeze jet front.

3.4   Validation of the EE-PBE approach for particle transport

The previous analysis confirms the ability of the QMOM poly-solver to describe droplet transport during respiratory activities. However, in a closed environment, such as a chamber, the behavior of the dispersion changes because of the role played by other phenomena, such as droplet settling, flow confinement, or recirculation. Therefore, the reliability of the EE-PBE approach to predict the space and time evolution of the aerosols in three-dimensional (3D) chambers is also assessed by comparing its results with the experimental data of Chen et al. [137].

3.4.1   Case description and numerical method

In the experiment of Chen et al. [137], non-evaporating particles (10 μm) and airflow are injected into a 3D chamber from the inlet on the left side and leave the chamber from the outlet on the right side. The gas phase velocity profiles and the normalized concentration at specific locations in the center plane were measured.

The geometry is shown in Figure 3.5. The size of the chamber is: length $\times$ width $\times$ height $= x \times y \times z = 0.8$ m $\times$ 0.4 m $\times$ 0.4 m. To match the experimental setups, the inlet and outlet are extended 0.2 m out of the chamber. They are of the same size, 0.04 m $\times$ 0.04 m, and their centers are located at $x = -0.2$ m, $y = 0$ m, $z = 0.36$ m and $x = 1.00$ m, $y = 0$ m, $z = 0.04$ m, respectively. Only half of the

3D chamber is selected as the computing domain due to symmetry. A multi-block structured grid with 67520 cube cells is built in this study. The grids of similar scale have been proven to be reliable under the experimental conditions [106, 137]. For boundary conditions, the inlet velocity is $0.225\,\mathrm{m\,s^{-1}}$. The dispersed phase volume fraction at the inlet is $\alpha_d = 5 \times 10^{-8}$, to match the experiment. The system is isothermal at 293.15 K. The boundaries except the symmetric plane and inlet/outlet regions, are set as no-slip walls. The particle density is $1400\,\mathrm{kg\,m^{-3}}$ as in the experiment.
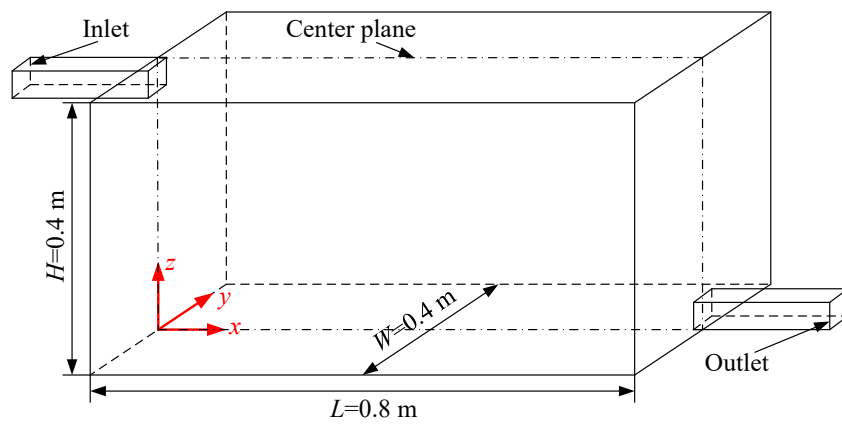
Fig. 3.5 Geometry of a ventilated 3D chamber model.

The QMOM poly-solver is adopted again to solve the TFM and PBE to trace the particles. The setup is similar to Section 3.3: RNG $k - \varepsilon$ model for the continuous phase and laminar for the dispersed phase, evaporation model disabled, and two nodes for the QMOM. The moments at the inlet are also evaluated using α_d and droplet size distribution (8 μm to 13 μm) of the experiment and are listed in Table 3.4.

Table 3.4 Moments at the inlet for the case of aerosol transmission.

Variable	Value
α_d (-)	5×10^{-8}
M_0 (m^{-3})	$9.587\,645 \times 10^{7}$
M_1 (m^{-2})	$9.561\,545 \times 10^{2}$
M_2 (m^{-1})	$9.548\,915 \times 10^{-3}$
M_3 (-)	$9.549\,295 \times 10^{-8}$

3.4.2   Results and discussion

The transient simulation is performed for a time long enough to reach the steady state as in the experiment. Then, the profile of x direction continuous phase velocity (U_x) and the dispersed phase volume fraction α_d at $x = 0.2$ m, 0.4 m and 0.6 m in the center plane ($y = 0$ m) are extracted. The normalized concentration is calculated as $\bar{C} = M_0/M_{0,\mathrm{inlet}}$. The comparison of predicted and measured U_x and $\bar{C}$ are shown in Figure 3.6. Good agreements are observed.

Because of the inlet jet flow, U_x is high in the upper region of the chamber ($z = 0.2$ m to $z = 0.4$ m). Figure 3.7a gives the magnitude and direction of the air velocity, which is similar to the flow pattern found by Chen et al. [137]. The jet is injected from the left upper inlet, impinges on the right wall, turns downwards, and finally moves out of the room from the right lower outlet. This leads to low-speed recirculation regions appearing in the lower part of the room. In these regions, the air flows to the left, resulting in the relatively uniform small negative U_x in the lower region ($z = 0$ m to $z = 0.2$ m) as in Figure 3.6a. Moreover, as the jet advances from $x = 0.2$ m to $x = 0.6$ m, it interacts with the surrounding still air. The maximum of U_x decreases and the velocity of surrounding air increases, showing a typical jet evolution.

Figure 3.7b and Figure 3.7c present the particle velocity of the two quadrature nodes, $\mathbf{U}_{\mathrm{particles},i}$. It can be noted that the difference between the two velocities is small. This is because particle size distribution is narrow and the diameters of the two quadrature nodes are 9.4 μm and 10.2 μm, respectively. They are close and thus the two quadrature nodes present similar behaviors. Consequently, for the particles having a narrow size distribution, it is reasonable to assume they move with the same velocity.

Figure 3.7d and Figure 3.7e show the slip velocity between air and quadrature nodes calculated by $\mathbf{U}_{\mathrm{slip},i} = \mathbf{U}_{\mathrm{air}} - \mathbf{U}_{\mathrm{particles},i}$. Because of the small particle sizes, the magnitude of slip velocities is small, namely, the particles tend to follow the airflow. Meanwhile, the slip velocities point upwards, indicating that the particles have a falling trend. The falling trend is more significant for the particles represented by the second quadrature node. They have a larger diameter, therefore, the magnitude of $\mathbf{U}_{\mathrm{slip},2}$ is slightly larger than $\mathbf{U}_{\mathrm{slip},1}$. This falling trend of 10 μm particles was also found by Pei et al. [146].
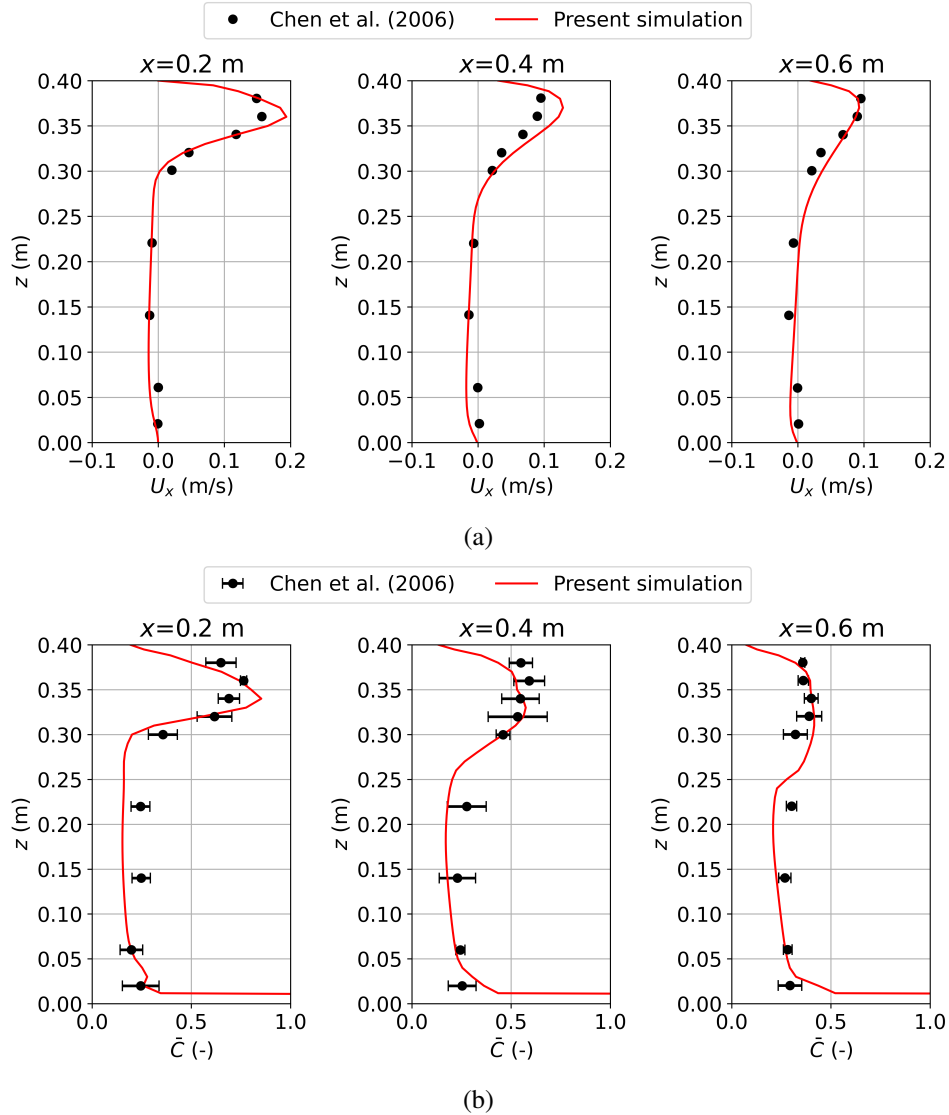
Fig. 3.6 The comparison of predicted and measured profiles at $x = 0.2$, 0.4 and 0.6 m in the center plane ($y = 0$ m): (a) the x direction continuous phase velocity U_x, (b) the normalized concentration $\bar{C}$.

Figure 3.7f shows the distribution of normalized concentration. It can be seen that the $\bar{C}$ is high within the jet. In the lower part, the aerosols, carried by the recirculated air, are uniformly dispersed with a relatively low normalized concentration of 0.3. Additionally, it should be noted that $\bar{C}$ is extremely high on the lower wall, indicating that the particles are accumulating there. This is caused by the boundary conditions: the no-slip boundary condition for continuous and dispersed phase velocity and the zero gradient boundary condition for volume fractions and moments. The particles

cannot leave the computing domain and thus accumulate there. Although this effect could be removed by specifying a particle depositing boundary condition as in the work of Chen et al. [137], we did not implement it because the inaccuracy is restricted to a very thin layer close to the lower wall and does not affect the remaining portion of the profile.
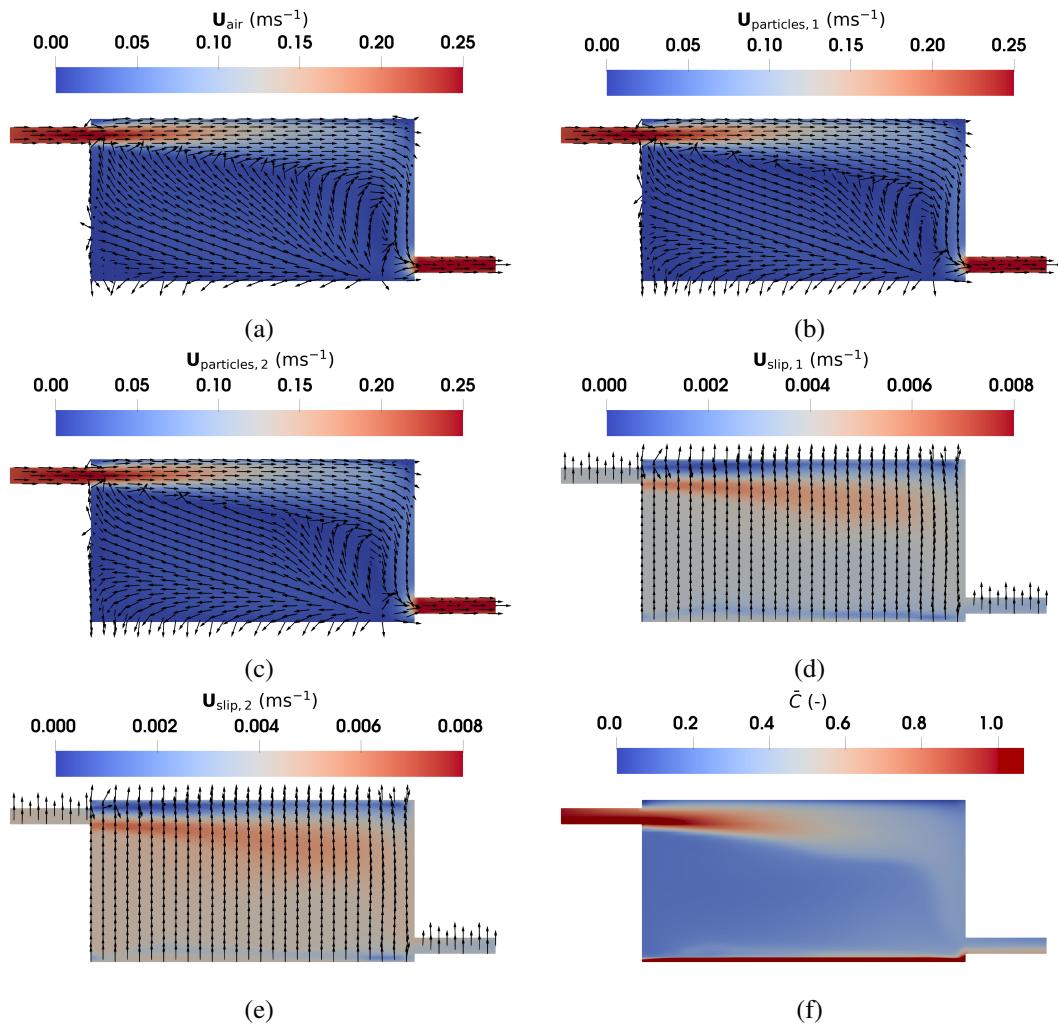
Fig. 3.7 The predicted velocity magnitude and direction and concentration in the center plane ($y = 0$ m): (a) air velocity; (b) particle velocity of the first quadrature node; (c) particle velocity of the second quadrature node; (d) slip velocity between air and the first quadrature node; (e) slip velocity between air and second quadrature node; (f) normalized concentration. The arrows in Figure (a) to (e) have identical lengths and only present the directions of velocities. The magnitudes of velocities are represented by the contours.

In conclusion, the predicted results agree well with the measured data indicating that the EE-PBE approach can be used to trace both flow and concentration fields of aerosols in the 3D chamber and the developed codes are reliable.

3.5   Transmission of cough droplets in a room

3.5.1   Case description and numerical method

Eventually, the EE-PBE approach is applied in the transmission and evaporation of cough droplets in a 3D chamber and compared with the numerical results using the E-L approach reported by Li et al. [52]. The geometry, identical to that in Li et al. [52], is shown in Figure 3.8, the size of which is length $\times$ width $\times$ height $= x \times y \times z = 4.0$ m $\times 2.0$ m $\times 3.0$ m. The mouth (inlet) is modeled by a circle, whose diameter is 2 cm. Its center is located at $x = 0$ m, $y = 0$ m, $z = 2.0$ m. The right boundary (or outlet) is open to the atmosphere. The bottom wall is also set as an outlet in order to avoid the accumulation of droplets in the near-wall cells, which might affect the stability of the poly-solver. Additionally, only half of the chamber is built as the computing domain in order to reproduce the settings used by Li et al. [52]. Therefore, the front boundary is set as a symmetric plane. All other boundaries are no-slip walls.
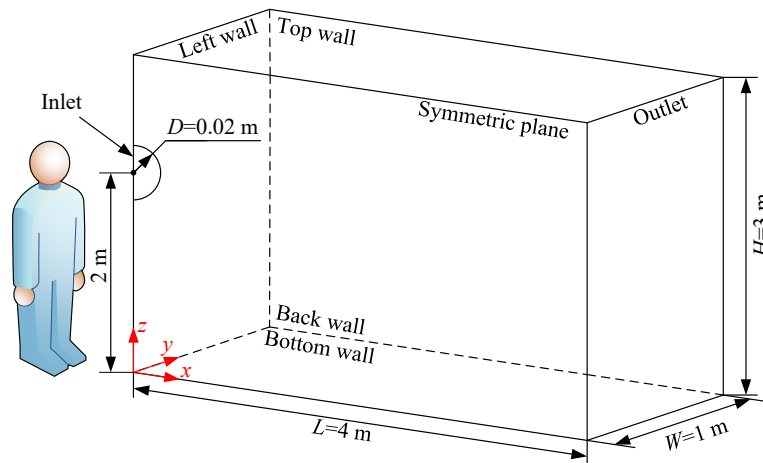
Fig. 3.8 Geometry of the 3D chamber.

A multi-block structured grid is built for the computing domain. The grid is refined in the near-wall regions and the inlet region. The grid convergence is

examined using three grids having 364640 (coarse), 831220 (middle), and 1912700 (fine) cube cells, respectively. It is found that the middle grid of 831220 cells shows good consistency with the fine grid and thus is adopted in this study. The details can be found in Appendix E.1

To compare with Li et al. [52], the same boundary conditions are used in this study. The ambient temperature is 298.15 K and the relative humidity is 50%. The cough jet temperature is 310.15 K and the relative humidity is 100%. The temperature of cough droplets is also 310.15 K. To mimic a single cough, a time-varying inlet velocity obtained from the experiment of Gupta et al. [46] is specified for the continuous phase. The cough lasts for 0.5 s with a maximum velocity of $13.4 \mathrm{~m\,s^{-1}}$ at 0.08 s, as shown in Figure 3.9a. The droplets are injected into the chamber with the same instantaneous velocity as the continuous phase. The droplet size distribution obtained from the experimental data of Chao et al. [28] is given at the inlet. As shown in Figure 3.9b, the droplet sizes range from 3 μm to 750 μm, and it can be noted that a huge number of small droplets only have a very low volume fraction while the large droplets are contrary. The dispersed phase volume fraction α_{d} at the inlet is 2.323×10^{-4}, which is equivalent to a total injected amount of 100 mg.
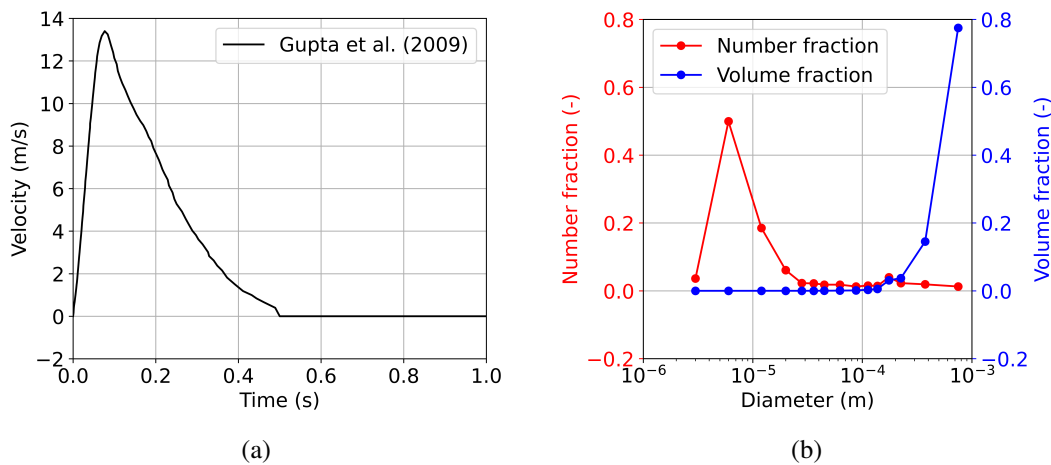
Fig. 3.9 The cough jet and droplets inlet boundary conditions: (a) the velocity of a single cough [46], (b) the number and volume fraction of the cough droplets [28].

For the transient simulation of the cough droplets, the SM-solver and the QMOM poly-solver are adopted to trace the droplets moving with different velocities on various sizes. The RNG $k - \varepsilon$ model is used for the continuous phase while the laminar one for the dispersed phase. The thermal physical property models in Appendix D are

Table 3.5 Size groups of the dispersed phase for small and large droplets.

Small droplets (< 100 μm)			Large droplets (> 100 μm)		
No.	d (μm)	f_i (-)	No.	d (μm)	f_i (-)
1	1.0	0	11	112.5	3.18×10^{-3}
2	3.0	5.76×10^{-5}	12	137.5	5.47×10^{-3}
3	6.0	6.33×10^{-3}	13	175.0	3.10×10^{-2}
4	12.0	1.88×10^{-2}	14	225.0	3.75×10^{-2}
5	20.0	2.86×10^{-2}	15	375.0	1.46×10^{-1}
6	28.0	2.93×10^{-2}	16	750.0	7.77×10^{-1}
7	36.0	5.97×10^{-2}	17	1500.0	0
8	45.0	9.71×10^{-2}			
9	62.5	2.60×10^{-1}			
10	87.5	5.00×10^{-1}			

adopted. A minimum diameter of 1 μm is specified for the evaporation model. After evaporation into the minimum diameter, the droplets will stop further evaporation, and they will only be dispersed by the airflow, leading to an accumulation of droplets in an indoor environment.

For the SM-solver, 17 pivotal volumes are used to cover the experimental DSD in the work of Chao et al. [28]. To model the multiple velocities of the droplets, a two-class MUSIG is adopted. As mentioned in Chapter 1, 100 μm is the crucial size [33], which differentiates the behavior of the droplets of different sizes. Therefore, the droplets are divided into two dispersed phases as shown in Table 3.5, where the pivotal volumes are converted into pivotal diameters for clarity. The first dispersed phase contains the small droplets (<100 μm), including 10 pivotal volumes (from No. 1 to 10), whose volume fraction at the inlet is 5.7×10^{-7}. The second one contains the large droplets (> 100 μm), including 7 pivotal volumes (from No. 11 to 17), whose volume fraction at the inlet is 2.3173×10^{-4}. The velocities of the two dispersed phases can be obtained by solving the three-fluid E-E model.

For the QMOM poly-solver, two nodes are adopted to trace the behavior of droplets. The moments are calculated by using the DSD in Figure 3.9b and scaled to match α_d at the inlet. The details are reported in Table 3.6. At the inlet, the two abscissas or node diameters are 21.6 μm and 550.7 μm, respectively. One is indeed

Table 3.6 Moments at the inlet for the case of cough droplets.

Variable	Value
α_{d} (-)	2.323×10^{-4}
M_0 (m^{-3})	$6.411\,369 \times 10^7$
M_1 (m^{-2})	$2.792\,789 \times 10^3$
M_2 (m^{-1})	$8.334\,057 \times 10^{-1}$
M_3 (-)	$4.436\,603 \times 10^{-4}$

smaller than 100 µm while the other is larger than 100 µm. Therefore, both small and large droplets can be represented by the quadrature nodes.

3.5.2 Results and discussion

Figure 3.10 and Figure 3.11 show the results obtained by using the SM. Figure 3.10a shows the predicted volume fraction of the dispersed phase for small droplets $\alpha_{\mathrm{d,S}}$. The small droplets mainly suspend in the air and travel a relatively short distance. This is because the small droplets, owning small momentum response time (or inertia), tend to be carried by the airflow. In addition, it can be noted that even the small droplets show a falling trend, especially at $t = 0.5$ s. A check of the volume fraction of the different size classes belonging to small droplets, reported in Figure 3.11a, shows that the falling trends are mainly caused by 10th and 9th size classes, which represent the size of 87.5 µm and 62.5 µm, respectively. For smaller size classes, the falling trends disappear and only a suspending trend is observed for the 5th size class (20 µm) in Figure 3.11a. This indicates that the size of 100 µm might be a little large to differentiate the small and large droplets.

The volume fraction of the dispersed phase for large droplets $\alpha_{\mathrm{d,L}}$ is shown in Figure 3.10b. The large droplets show a remarkable falling trend and no suspending trends are observed because of gravity. By inspecting the volume fraction of different size classes belonging to large droplets (Figure 3.11b), it can be seen that the droplets of all the size classes belonging to the large droplets are falling. This again implies that the crucial size of 100 µm is large enough.

Table 3.7 presents the maximum horizontal traveling distance and vertical expansion of the small and large droplets. It can be noted that, before settling, the
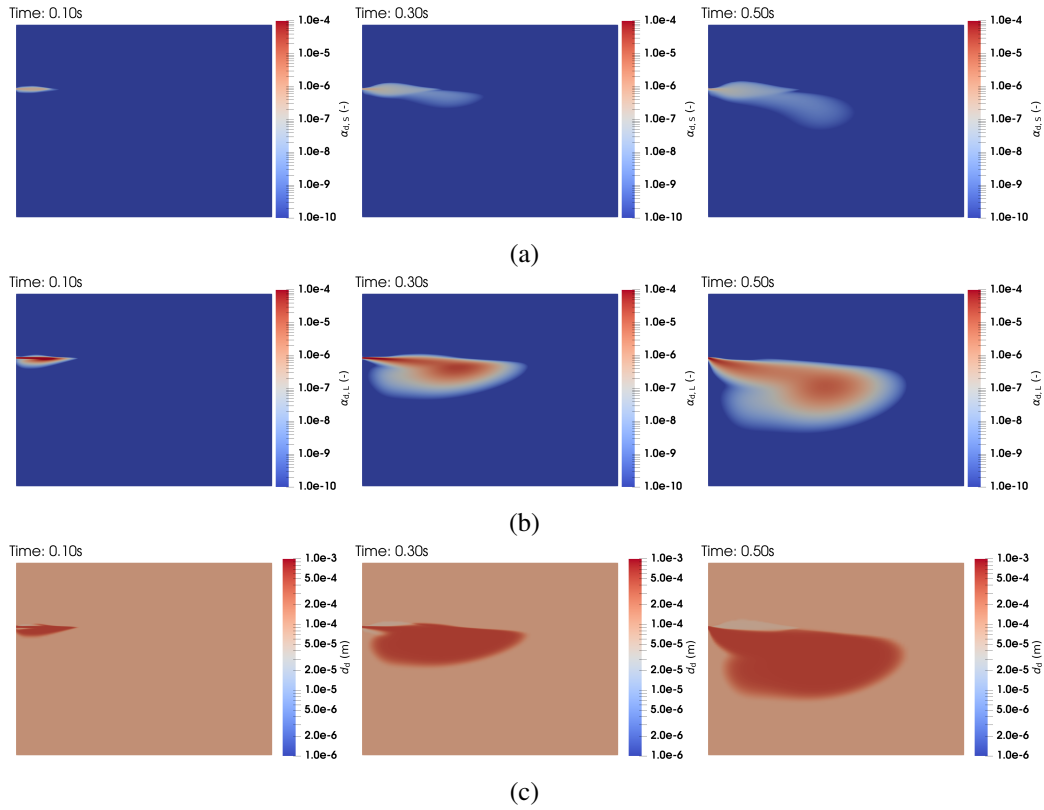
Fig. 3.10 The variables of the dispersed phase obtained by using the SM-solver in the symmetry plane at different times, from left to right: $t = 0.1$, 0.3 and 0.5 s: (a) volume fraction for small droplets $\alpha_{d,S}$, (b) volume fraction for large droplets $\alpha_{d,L}$, (c) mean dispersed phase diameter d_d.

large droplets travel about 42% to 52% longer than the small ones. This is because the large droplets have a larger momentum response time (or inertia), less affected by the originally still indoor air, traveling a longer distance with their high initial velocity. However, after the settlement of the large droplets, the small droplets remain suspended in the air. Depending on the background airflows, such as those induced by indoor ventilation systems, the small droplets are possible to be transported to larger ranges. In particular, affected by the time-varying inlet velocity and gravity, the large droplet cloud shows a leftward-opening parabola-shaped distribution. The droplets released at the beginning and the ending of the cough might have the same x-coordinate (horizontal distance) but different z-coordinates (height). As a result, the vertical expansion of the large droplets is also larger than that of the small droplets. A similar pattern was also found in the work of Dbouk et al. [107], where the E-L approach was used for the cough droplets.

Table 3.7 Maximum horizontal distance and vertical expansion of the small and large droplets.

Time (s)	Horizontal distance (m)		Vertical expansion (m)	
	Small droplets	Large droplets	Small droplets	Large droplets
0.1	0.63	0.96	0.10	0.22
0.3	1.81	2.57	0.24	0.68
0.5	2.15	3.06	0.46	1.10

The Sauter mean size for the two dispersed phases is shown in Figure 3.10c. The sizes of the small and large droplets are around 50 μm and 500 μm, respectively. The size changes caused by evaporation are not significant. The initial Sauter mean size for the small and large droplet phases are 53.2 μm and 544.5 μm, respectively. According to the d^2-law in Section 3.2, even for the small droplets, the time required for full evaporation is in order of several seconds. Therefore, at t=0.5 s, both droplets have not evaporated remarkably.

(a)

(b)
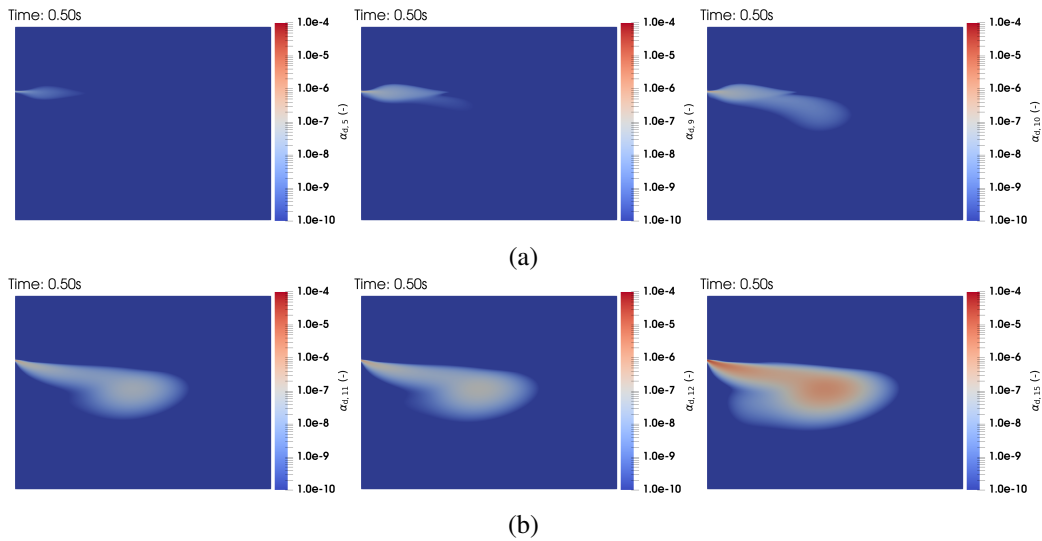
Fig. 3.11 The volume fraction of the size classes obtained using SM-solver in the symmetry plane at $t = 0.5$ s: (a) for small droplets: 20 μm ($\alpha_{d,5}$), 62.5 μm ($\alpha_{d,9}$) and 87.5 μm ($\alpha_{d,10}$), (b) for large droplets: 112.5 μm ($\alpha_{d,11}$), 137.5 μm ($\alpha_{d,12}$) and 375 μm ($\alpha_{d,15}$).

The Figures 3.12 to 3.14 show the results obtained by using the QMOM. Figure 3.12 gives the evolution of the dispersed phase volume fraction, α_d. Similar to the results obtained with the SM-solver and in [52], the suspension of small droplets and the falling of large droplets are observed. It should be noted that the quadrature

nodes in QMOM represent the dynamic size distribution rather than the fixed size classification in the SM. Therefore, the conclusion cannot be drawn only from Figure 3.12, but also with the help of the quadrature node distribution in Figure 3.13. As mentioned before, the inlet quadrature nodes are 21.6 μm and 550.7 μm, respectively. Since they can move with different velocities, the small droplets initially represented by the 1st node will evaporate remarkably, suspend in the air and form a suspending droplets cloud while the large droplets initially represented by the 2nd node will evaporate slightly, fall in the air and form a falling droplets cloud. Therefore, the size distribution moves toward smaller sizes in the suspending cloud and moves toward larger sizes in the falling cloud. The changing DSD results in the changes of the quadrature nodes. Finally, the decreasing 2nd node diameters in Figure 3.13b together with the small 1st node diameter represent the small droplets that are found to be suspending. Meanwhile, the increasing 1st node diameters in Figure 3.13a together with the large 2nd node diameter represent the large droplets that are found to be falling.
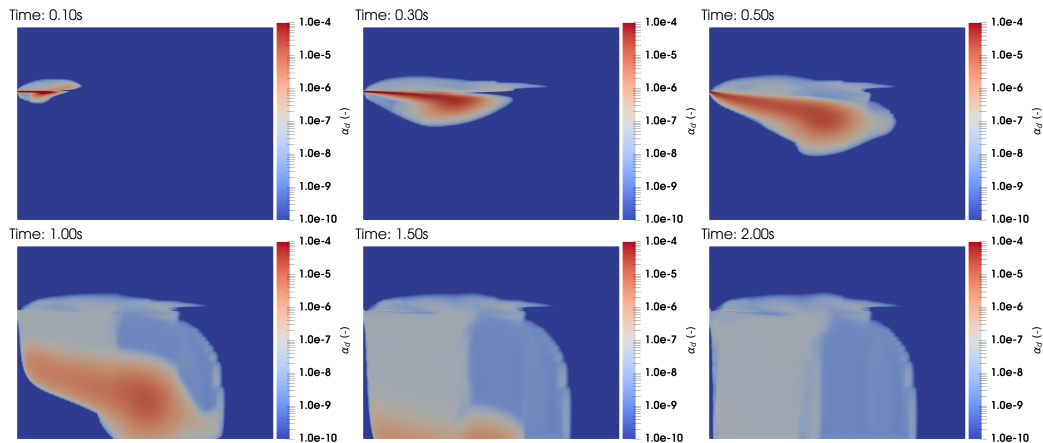
Fig. 3.12 The dispersed phase volume fraction α_d obtained by the QMOM poly-solver in the symmetry plane at different times, from left to right and top to bottom: $t = 0.1, 0.3, 0.5, 1.0, 1.5$ and 2.0 s.

Figure 3.14 shows the 0th order moment M_0, representing the droplet number density. Again, the suspending or falling trends are found. Comparing Figure 3.12 with Figure 3.14, it can be found that the suspending small droplets have a huge number density but a small volume fraction. For other respiratory activities, like speaking, fewer droplets are expelled. After evaporation, the volume fraction for the small droplets might be extremely small, which might result in difficulty in analysis.
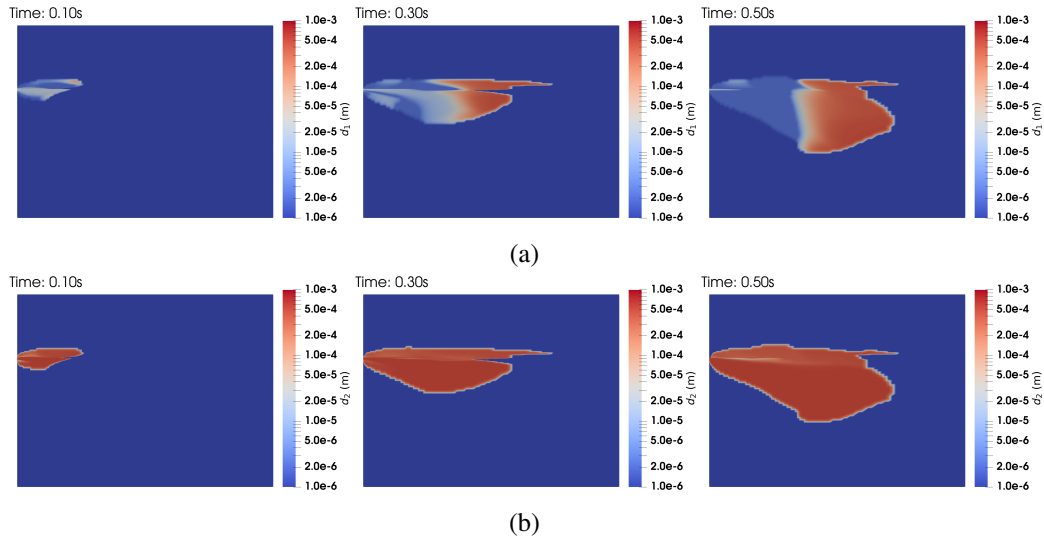
Fig. 3.13 The quadrature node diameter obtained by the QMOM poly-solver in the symmetry plane at different times, from left to right: $t = 0.1$, 0.3 and 0.5 s: (a) 1st quadrature node $d_{d,1}$, (b) 2nd quadrature node $d_{d,2}$.
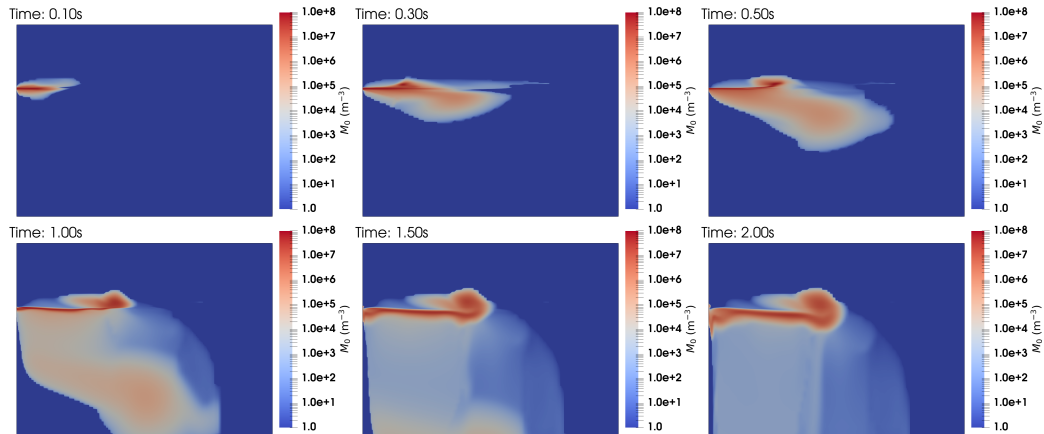
Fig. 3.14 The 0th order moment M_0 obtained by the QMOM poly-solver in the symmetry plane at different times, from left to right and top to bottom: $t = 0.1$, 0.3, 0.5, 1.0, 1.5 and 2.0 s.

Furthermore, the parabola-like pattern of the large droplet cloud in the work of Dbouk et al. [107] is also observed in Figure 3.12 or Figure 3.14. Compared with the results obtained using the SM (Figure 3.10b), the parabola-like pattern is less remarkable due to its shorter lower part. For example, at $t = 0.5$ s, the horizontal length of the lower part is around 1.5 m, which is smaller than that of the SM (2.8 m). This is because the diameter of large droplets in SM is smaller than that in QMOM.

So, the large droplets in QMOM have larger mass or inertia and thus they are less affected by the originally still indoor air. Finally, they are not exceeded too much by the later released droplets, resulting in a less remarkable parabola-like pattern. The droplet trajectories at 0.5 s and 2.0 s are compared with those in Li et al. [52], where the maximum droplet traveling distance at 0.5 s and 2.0 s are approximately 2.70 m and 3.25 m, respectively. In this study, the traveling distances are 2.95 m at 0.5 s and 3.20 m at 2.0 s. Good agreement is observed and, identical to the conclusion of Li et al. [52], large droplets settle on the ground within 2.0 s. Therefore, the results obtained by using the EE-PBE approach can be regarded as reliable.

The dispersed phase volume fraction α_d and diameter d_d obtained by using SM and QMOM are compared in Figure 3.15. As shown in Figure 3.15a, the vertical distribution of the droplets, represented by α_d and predicted by the two approaches, is similar. The cough jet is injected at the height of $z = 2.0$ m. Because of the gravity, most part of the droplet jet falls. Therefore, the main peak of the α_d distribution is below $z = 2.0$ m. Additionally, both SM and QMOM show an additional peak above the main jet, while SM also shows an additional peak below the main jet. The former is caused by the suspension of the small droplets. As mentioned before, the suspending trend is more significant in QMOM due to its lower initial 1st node diameter, and thus its peak is more significant. The latter is caused by the parabola-like pattern, which is more remarkable in SM than in QMOM. Therefore, such a peak is not captured by QMOM.

Figure 3.15b shows the distribution of d_d along horizontal lines at different heights. At $z = 2.1$ m, the height above the inlet, d_d predicted by SM and QMOM is smaller than 100 µm because small droplets are suspended in air and dispersed to this region. Significant differences can be noted in the results. d_d obtained by SM changes in a narrow range and is distributed in a small region while that by QMOM is the opposite. This, as discussed previously, is because QMOM tracks the changing DSD dynamically and captures a more significant suspending trend of small droplets. Therefore, in QMOM, d_d has wider range (1 µm to 100 µm) and droplets are distributed in larger region ($x = 0.1$ m to $x = 2.9$ m). At the height of the inlet, $z = 2.0$ m, the sharp decrease of d_d near the inlet indicates the falling of large droplets. Below the inlet, at $z = 1.9$ m and 1.8 m, d_d obtained by the two methods are very close. It is large and almost keeps constant, indicating that the large droplets are falling to the ground and barely evaporate. Moreover, the traveling distances predicted by the two methods are also close. This d_d distribution, again, shows the

different behaviors of small and large droplets under gravity and evaporation, and presents the ability of the EE-PBE approach to predict the transport of respiratory droplets.

(a)

(b)
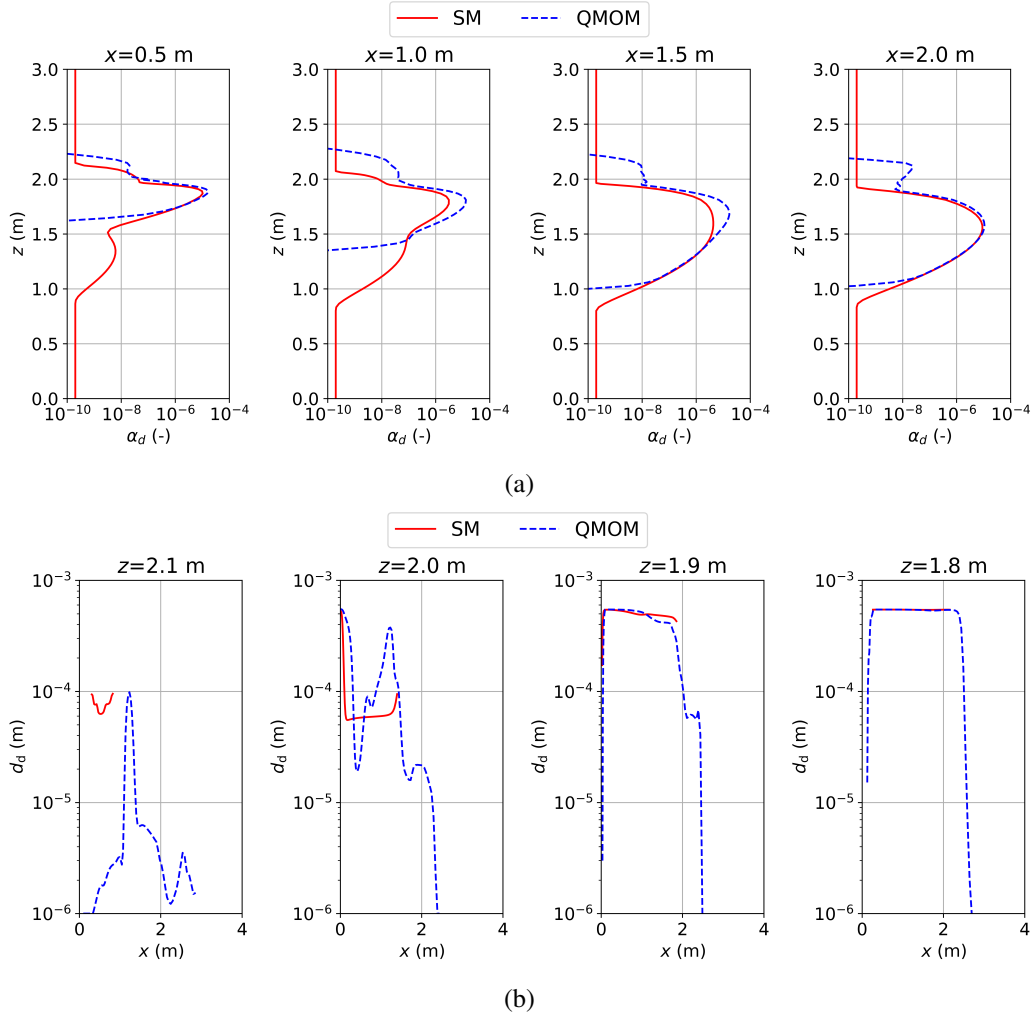
Fig. 3.15 Comparison of the dispersed phase variables obtained using SM and QMOM in the symmetry plane at $t = 0.5$ s: (a) vertical distribution of the dispersed phase volume fraction α_d at $x = 0.5, 1.0, 1.5$ and 2.0 m, (b) horizontal distribution of the dispersed phase diameter d_d at $z = 2.1, 2.0, 1.9$ and 1.8 m (the curves are only plotted in regions where $\alpha_d \geq 1 \times 10^{-10}$, namely, where the droplets exist).

Finally, the advantages and disadvantages of SM and QMOM are discussed here. The simulations are parallelized on a workstation with an Intel Xeon CPU E5-2630 v4 (2.20 GHz, 10 cores). The average time (averaged on the first 5000 time steps) for every 1000 time steps of SM-solver and QMOM poly-solver are 4.8 hours and 6.32

hours, respectively. SM has relatively lower costs than those of QMOM in the case and setup of this study. This is because, the QMOM poly-solver has more equations to solve, and QMOM also has additional costs of moments inversion. However, it should be noted that two nodes are used in the QMOM simulation of this study. The first four moments are solved and traced, including M_2, the total surface area of droplets, which is of great importance in droplet evaporation according to the d^2 law. As for SM, only the total number and total volume are traced (equivalently, M_0 and M_3 in QMOM). The results of SM in this study are acceptable and in good agreement with the literature, but in other cases, more size classes might be required by SM to make up for the missing total surface area. Obviously, this would increase the computational costs of SM.

Additionally, to model the different velocities of droplets with different sizes, the SM (MUSIG method) requires manually dividing the size classes into several groups and defining each of them as a dispersed phase to obtain their different velocities. Inappropriate criteria can result in unreasonable results, such as the group of small droplets showing a falling trend. On the contrary, the QMOM uses the quadrature nodes obtained from the quadrature method to represent the droplets moving with different velocities. No explicit interaction is required, which can provide a better representation of the behavior of the polydispersed droplets.

As for the post-processing, both methods can directly provide variables, like the droplet volume fraction, for analyses. Furthermore, QMOM can directly provide the number density M_0, which is especially helpful in the simulations having a too-low volume fraction to analyze.

3.6   Summary

In this chapter, the developed EE-PBE approach for the transmission and evaporation of polydispersed respiratory droplets is systematically verified and validated with experimental or numerical data from the literature. This is performed by first assessing the different aspects of the transmission process, including evaporation, movement of the respiratory jet (or puff), and particle transmission in ventilated environments. Finally, all features are collectively considered through the examination of the transmission of polydispersed evaporating cough droplets. The following conclusion can be drawn.

The evaporation model and the thermal physical property models are verified and validated first against the experimental results of a stationary evaporating pure water droplet. The predicted droplet size time evolution is in good agreement with the experimental data, laying a solid foundation for the following coupled approaches.

The evaporation model is further validated with the reported diameter changes of evaporating droplets in the literature. Both SM and QMOM agree well with the literature, indicating that the EE-PBE approach can be used to trace the evaporation of the droplets.

Since the respiratory droplets are carried by and interact with the expelled airflow, the ability of the EE-PBE approach to accurately predict the evolution of the exhaled jet or puff during respiratory activities is assessed. The poly-solver solving TFM and PBE is validated using the measured temporal evolution of the sneeze jet front. The simulation agrees well with the measurement. The transition from the jet stage to the puff stage is captured. Therefore, the solver can be used in the simulations of respiratory activities.

The reliability of the EE-PBE approach is further tested by comparing the predicted results of the poly-solver with the experimental results for aerosol transmission in a ventilated room model. It is found that both velocity profiles and concentration distributions agree well with the experimental results. The droplets, having a narrow size distribution, can be assumed to move with the same velocity. The approach is reliable for aerosol transmission simulations.

Finally, the EE-PBE approach is applied in the transmission and evaporation of polydispersed evaporating cough droplets in a 3D chamber. The SM-solver and poly-solver are adopted and compared. The suspending trends of small droplets and the falling trends of large droplets are presented by both approaches. The droplets are found to be able to travel a distance longer than 2 m, which is valuable for the guidelines of social distancing. Additionally, the advantages and disadvantages of the two methods are discussed. Both methods can directly provide variables for analyses, such as volume fraction or mean size. Compared with SM, which requires that the user subdivides the population of droplets into classes for the calculation of size and velocity, no manual intervention is required for QMOM, which thus is free of unreasonable results caused by inappropriate criteria.

Chapter 4

Respiratory droplet transmission under ventilation systems

The ventilation systems, changing indoor ambient conditions and resulting in diverse indoor airflow patterns, can significantly affect the transmission of respiratory droplets. Therefore, they are widely used to dilute or remove respiratory droplets and to control indoor infection. The Eulerian approaches provide computationally efficient and reliable tools to predict the fate of respiratory droplets under indoor ventilation systems. In this chapter, the ability of different Eulerian approaches to deal with different kinds of droplets is assessed using the experimental results in the literature: in Section 4.1, the PSPM is used to trace the transmission of small-size droplets (or aerosols) in an office equipped with displacement ventilation (DV), stratum ventilation (SV), and mixing ventilation (MV); in Section 4.2, the TFM is used to trace the transmission of non-evaporating particles in an office under DV and MV; in Section 4.3, the EE-PBE approach is applied in the transmission of evaporating droplets in an isolation ward with MV.

4.1   The pseudo-single-phase model for tracer gas

The PSPM is first validated with the experiment of Tian et al. [87]. In their experiment, the tracer gas CO_2 was adopted as a surrogate of the small-size respiratory droplets or aerosols to study the performance of DV, SV, and MV in a small office.

4.1.1   Case description and numerical method

As shown in Figure 4.1, a thermally isolated small office was adopted in the experiment, whose dimensions were length (x) × width (y) × height (z) = 4 m × 3.5 m × 3.5 m. The inlets of DV (1.56 m × 0.355 m), SV (0.19 m × 0.09 m), and MV (0.19 m × 0.09 m) were located on the front wall ($y = 3.5$ m). The exhaust was extended into the office by a square pipe. On the ceiling, there were three fluorescents, each had a power rate of 72 W. In the office, there was a desk, a closet, a computer (consisting of a system unit on the floor and a monitor on the desk), and a manikin. The manikin was represented by a rectangular cuboid. A light bulb of 100 W was located inside the cuboid to model the thermal effect of a sedentary human body, and the system unit also had a power rate of 180 W. In the experiment, different CO_2 releasing locations, floor ($z = 0$ m), desk ($z = 0.8$ m), and armpit ($z = 1.0$ m), were considered, and the profiles of velocity, temperature, and CO_2 concentration were measured along the sampling lines under steady states.

(a)   (b)
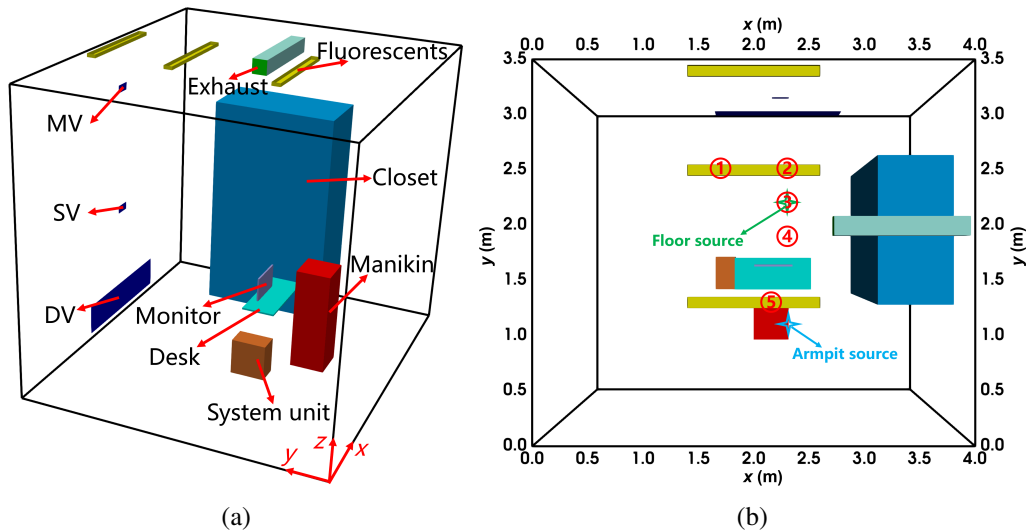
Fig. 4.1 The configuration of the office with DV, SV, and MV: (a) the layout; (b) the locations of sampling lines and locations of sources. The locations of sampling line 1 to 5 are (x, y) = (1.7 m, 2.5 m), (2.35 m, 2.5 m), (2.35 m, 2.2 m), (2.35 m, 1.9 m), (2.18 m, 1.25 m), respectively. The floor source location is (x, y, z) = (2.35 m, 2.20 m, 0.00 m), and the armpit source is (2.40 m, 0.95 m, 1.00 m).

The computational geometry was built as the experimental configuration. To reduce the complexity and computational costs, some simplifications were carefully made. The desk legs, the keyboard, and the cables of the computer were neglected.

In particular, the ventilation inlet diffusers were also simplified. For example, the inlet of DV in the experiment was a perforated diffuser with a perforated area ratio of 33.2%, namely, the supplied air can only flow through 33.22% of the DV inlet area. The reduced flowing area resulted in an increase in inlet velocity. For simplicity, the detailed geometry of the diffuser was not built but replaced with a simple opening. To match the perforated area ratio, the method of Zhang et al. [198] was adopted to specify boundary conditions for the diffuser. It was achieved by specifying the measured velocity for a number of grid cells of the diffuser boundary. Meanwhile, the number of grid cells was determined by the perforated area ratio. This method guaranteed the consistency of supplied air momentum and flow rate and was widely used to simplify the diffusers [199, 65].

As for the other boundary conditions, they were specified according to the experimental setups. In this study, six simulations for three ventilation systems under one inlet flow rate (2.2 air changes per hour, ACH) and two source locations were performed. The experimental case numbers were: DV-A1, SV-A1, MV-A1, DV-F1, SV-F1, and MV-F1. Therefore, the velocity was given as mentioned above. The walls and other surfaces were set as non-slip boundary condition, and a fixed pressure was prescribed at the exhaust. For the temperature boundary conditions, a fixed temperature was prescribed at the inlet; fixed power rates were specified for the fluorescents, the system unit, and the manikin; the walls, the floor, and the ceiling were set as adiabatic due to the experimental condition of thermal isolation. The adiabatic boundary condition was also specified for the surfaces not mentioned in the reference paper. Additionally, the inlet concentration and the source releasing rate of CO_2 were also specified according to experimental data.

The PSPM was adopted for the steady simulations. Since the relative humidity (RH) was also measured in the experiment, the air was regarded as consisting of three components, dry air, water vapor, and CO_2 in the simulation. Therefore, two species transport equations for water vapor and CO_2 were solved, respectively. The turbulent diffusivity was calculated using the default turbulent Schmidt number $Sc_t = 0.7$. The molecular diffusivity of CO_2 and water vapor were 1.4×10^{-5} m^2s^{-1} [200, 201]. The thermal physical model depending on temperature and composition as in Appendix D was used and the turbulence was modeled by using the RNG $k - \varepsilon$ model. The second-order schemes were used to discretize the governing equations.

The hexahedral grid was built for the simulation and was refined in the regions near walls and surfaces. The grid convergence was examined using three grids having 258232 (coarse), 553632 (medium), and 1222930 (fine) cells, respectively. It was found that the results of the medium grid and the fine grid were very close and presented good consistency. As a result, the medium grid having 553632 cells was adopted for the simulations in this study. The details can be found in Appendix E.2.

4.1.2 Results and discussion

Figure 4.2, 4.3 and 4.4 show the predicted and measured profiles of velocity, temperature, and CO_2 concentration under DV, SV, and MV, respectively. It can be seen that the predicted results agree well with the experimental data in most of the cases. Some discrepancies are found in the profiles of temperature or concentration at some locations (e.g., Location 5 for DV). They may be caused by the differences in boundary conditions. As mentioned previously, the reference paper only provides boundary conditions for several surfaces. For the unmentioned surfaces, the adiabatic condition was adopted in the simulations, which may be different from the experimental conditions and thus result in discrepancies. Such discrepancies are acceptable. Furthermore, some flow features that were not captured by the experiment due to the limited number of measuring points are described by the numerical simulations. This indicates that the adopted PSPM is reliable in tracing the tracer gas transmission in indoor environments and is able to provide detailed flow fields.

Additionally, it can be noted that the different ventilation systems, resulting in different indoor airflow patterns, present different temperature, velocity, and CO_2 concentration profiles. In fact, the different ventilation systems are distinguished by the form in which the fresh air is supplied, including the locations of the inlet and exhaust, the air passing area, and the air velocity. These differences naturally result in different indoor airflow patterns, and thus lead to different effectiveness in removing the respiratory droplets. Figure 4.5 further gives the velocity field of DV, SV, and MV in the plane of $x = 2.2$ m, in which the typical indoor airflow patterns of the three ventilation systems [202] were successfully captured. Detailed discussions are presented as follows.

Fig. 4.2 The predicted and measured results along the sampling lines in the small office under DV: (a) velocity magnitude; (b) temperature; (c) CO_2 concentration with source located at the armpit ($z = 1.0$ m); (d) CO_2 concentration with source located on the floor ($z = 0$ m). Circles: experimental data [87]; solid lines: numerical results of this study.

For the case of DV, the fresh cool air is supplied with a relatively low velocity from the lower part of the front wall as shown in Figure 4.1a. Therefore, both the predicted and measured velocities are higher in the lower part as in Figure 4.2a. Meanwhile, as shown in Figure 4.2b, the temperature at the five sampling lines is lower near the floor due to the supplied cool air and is higher near the ceiling due to the thermal effect of the fluorescents. Figure 4.5a presents the magnitude

and direction of velocity under DV in the plane of $x = 2.2$ m, which intersects the manikin and the desk. The supplied cool air has a lower temperature and thus high density. Therefore, after entering the office, the airflow moves downwards due to gravity and then moves along the floor. Meanwhile, due to the thermal effect of the manikin, the air near the manikin surface is heated and its density decreases. The heated air moves upwards due to buoyancy and presents upward airflow around the manikin, which is especially significant over the head (or top) of the manikin. Such upward buoyant airflows tend to transport the tracer gas or aerosols from the floor to the ceiling.

As a result, when the source is at the armpit as shown in Figure 4.2c, the CO_2 concentration increases with the height. When the source is on the floor as shown in Figure 4.2d, the CO_2 concentration presents similar trends. However, at Location 3, 4, and 5 the CO_2 concentration near the floor is extremely high. This is because the source is located at Location 3. At Location 3 and its downstream, Location 4 and 5, the CO_2 accumulates in the near wall region, resulting in a high concentration. Above the near wall region, the CO_2 concentration is also increasing with the height. Therefore, the DV transporting the gaseous pollutant or small-size droplets to the upper region of the office can reduce the indoor infection risk.

For the case of SV, the fresh cool air is supplied from the middle part of the front wall as shown in Figure 4.1a. Operating under the same air change rate, its velocity is higher than DV because of its smaller size. Therefore, as shown in Figure 4.3a, at Location 2, 3, 4, and 5, both predicted and measured velocities present remarkable velocity peaks at the injection height, which decrease with increasing traveling distance (from Location 2 to Location 5). At Location 1, far from the SV inlet, there is no such peak, and the velocity is small and relatively uniform. Figure 4.3b gives the temperature profiles. Similar to the velocity profiles, the numerical results also present the low-temperature peaks at the injection height due to the supplied cool air. Such peaks are not found by the experimental results because of the limited number of measuring points.

Figure 4.5b shows the velocity field under SV. It can be seen that the supplied air impinges on the manikin. The main part of the airflow moves downwards along the front surface of the manikin. After reaching the floor, it continues to move along the floor and then the front wall, finally forming a large recirculation region in front of the manikin in the lower part of the office. A small part of the flow passes through

the head of the manikin, impinges on the back wall, and forms a recirculation region behind the manikin. Additionally, due to the obstruction of the monitor, there is also a small part of the airflow moving downwards along the monitor. These airflows determine the distribution of CO_2 in the office.
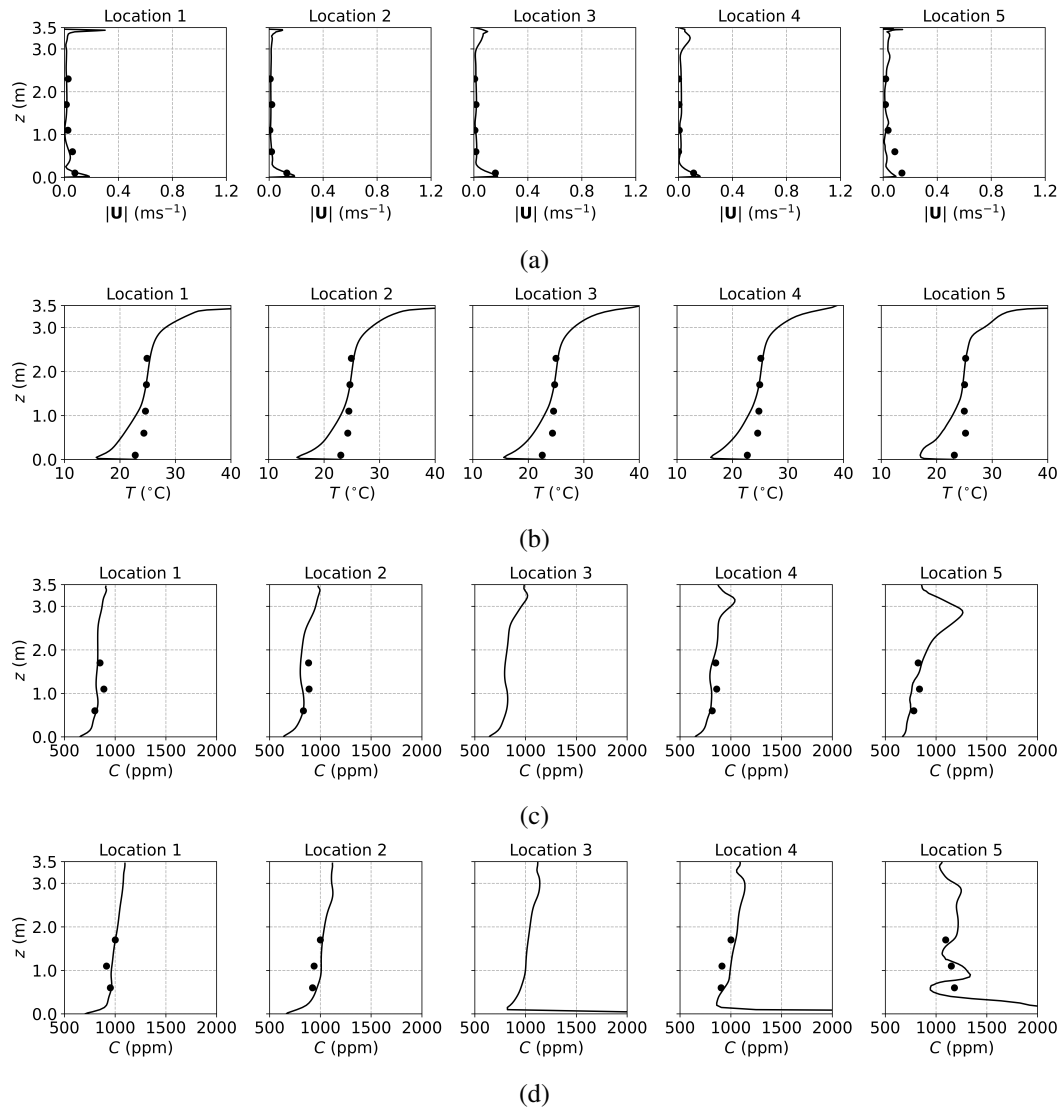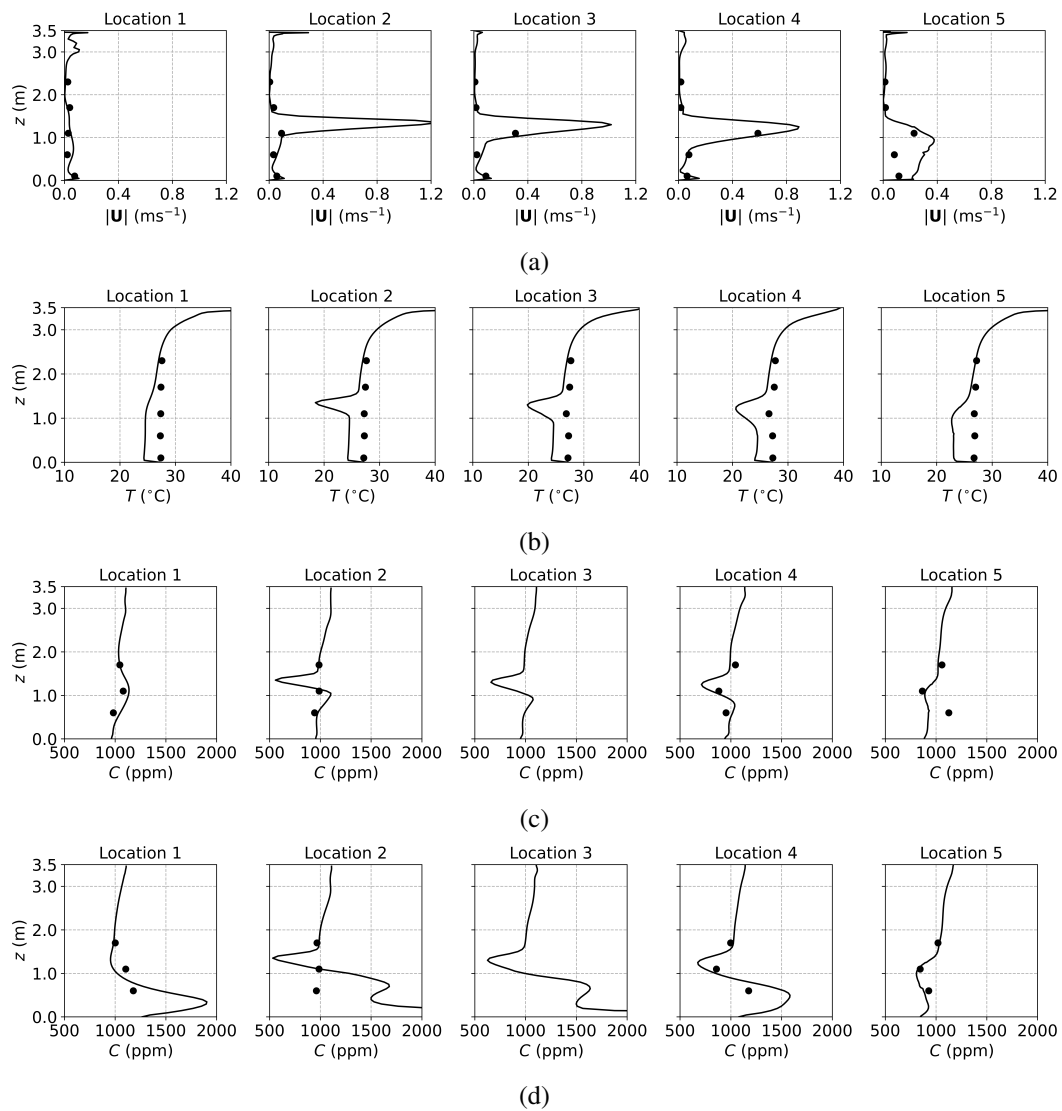

Fig. 4.3 The predicted and measured results along the sampling lines in the small office under SV: (a) velocity magnitude; (b) temperature; (c) CO_2 concentration with source located at the armpit ($z = 1.0$ m); (d) CO_2 concentration with source located on the floor ($z = 0$ m). Circles: experimental data [87]; solid lines: numerical results of this study.
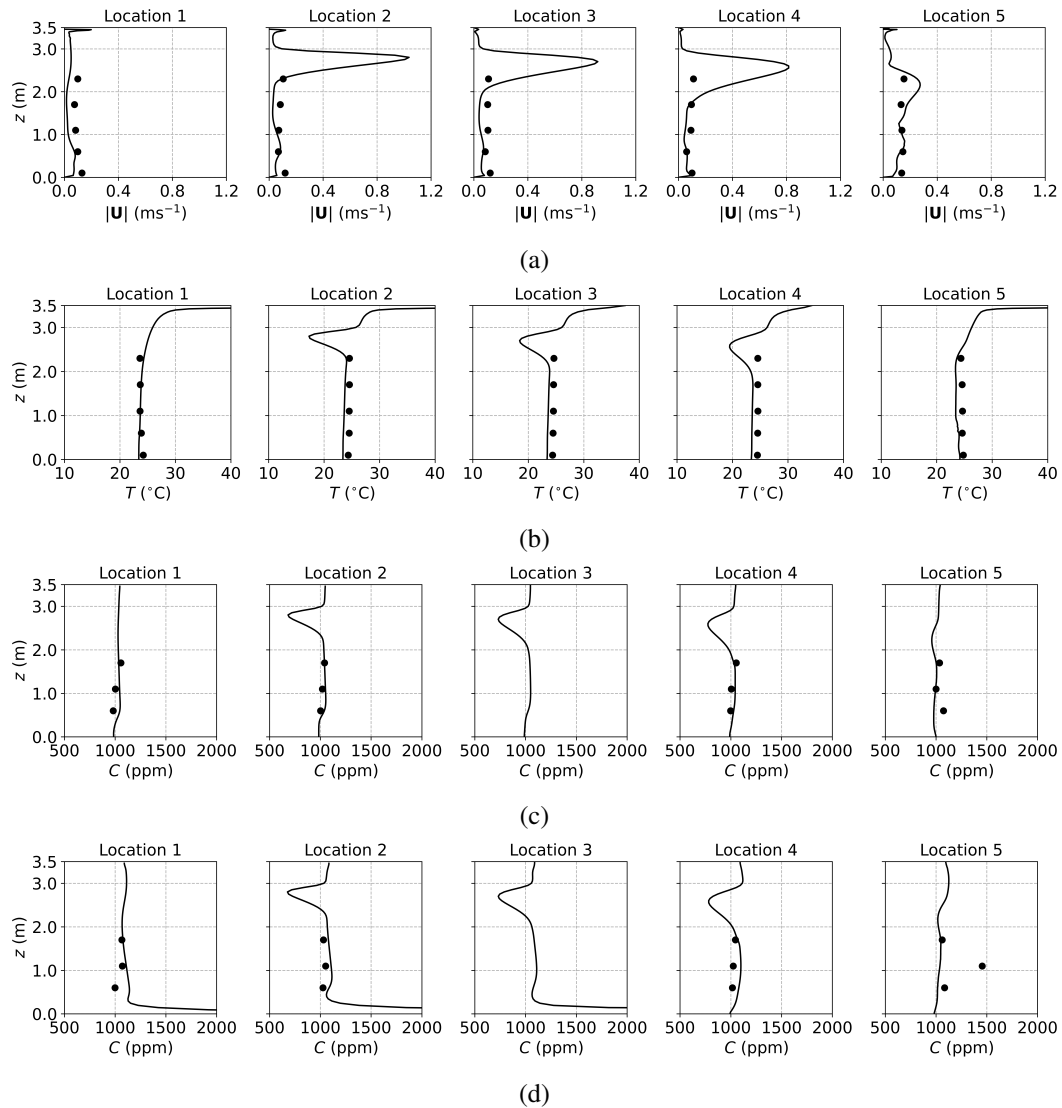
Fig. 4.4 The predicted and measured results along the sampling lines in the small office under MV: (a) velocity magnitude; (b) temperature; (c) CO_2 concentration with source located at the armpit ($z = 1.0$ m); (d) CO_2 concentration with source located on the floor ($z = 0$ m). Circles: experimental data [87]; solid lines: numerical results of this study.

Figure 4.3c gives the CO_2 concentration profiles when the source is at the armpit ($z = 1.0$ m). It can be seen that at Location 2, there is a low concentration peak in the height of the SV injection. This is because Location 2 is in front of the SV inlet. The supplied fresh air, passing through the sampling line, results in the low CO_2 concentration. Below this peak, there is also a smaller high-concentration peak, which is caused by the recirculation in front of the manikin. From Location 3 to

5, downstream of Location 2, the CO_2 concentration profiles are similar but have decreasing peak magnitudes due to interaction with the surrounding air. At Location 1, away from the SV inlet, there is no low-concentration peak but only one small high-concentration peak caused by the recirculation. When the CO_2 source is on the floor ($z = 0$ m), as shown in Figure 4.3d, similar low concentration peaks are also observed from Location 2 to 5. However, the CO_2 concentration is high in the lower regions. This is because the CO_2 source is located in the recirculation region before the manikin, which prevents CO_2 from being transported to other regions.

The SV, providing fresh air to the breath zone in front of the manikin directly, can significantly reduce the infection risk. However, its performance might be easily affected by the location of the people and the layout of the furniture. For example, a standing person might find it difficult to reach the injected fresh air. Or, using a larger monitor or installing barriers might block the SV injection and thus affect its performance. Therefore, when using SV, attention is required for the indoor layout to obtain better performance.

For the case of MV, the fresh cool air is supplied from the upper part of the front wall as shown in Figure 4.1a. Similar to SV, its velocity is relatively high. As shown in Figure 4.4a, at Location 2, 3, 4, and 5, the numerical results present remarkable velocity peaks at the injection height in the upper part of the office. Correspondingly, the temperature profiles in Figure 4.4b have low-temperature peaks at the injection height. Below the injection height, the temperature is almost uniform.

Figure 4.5c shows the velocity field under MV. It can be seen that the injected airflow gradually moves downwards due to gravity, and results in different recirculation regions in the office. Such recirculation regions will fully mix the indoor air and provide a uniform environment. As a result, below the injection height, in addition to the temperature, the CO_2 concentrations in the two cases of different source locations are also uniform as shown in Figure 4.4c and Figure 4.4d. This indicates that the MV can reduce the total amount of aerosols meanwhile it can promote the uniform dispersion of aerosols. Therefore, MV might not be a suitable choice to control indoor infection.

In summary, considering the limited experimental conditions provided in the reference paper, the PSPM gives reasonable predictions of the velocity, temperature, and CO_2 concentration profiles, which present good agreement with the experimental data. The PSPM is reliable in predicting the transmission of gaseous pollutants or

aerosols in ventilated indoor environments. Additionally, the DV, SV, and MV resulting in different indoor airflow patterns, have different performances in controlling indoor infection.

(a)

(b)

(c)
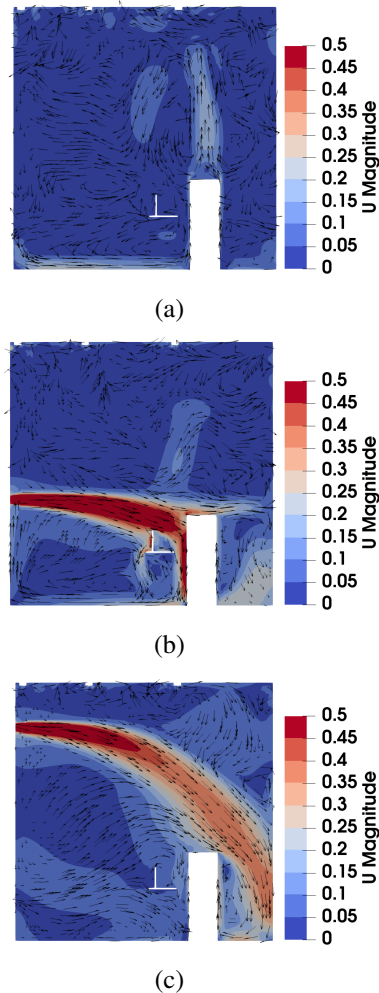
Fig. 4.5 The velocity field in the small office under DV, SV, and MV in the plane of $x = 2.2$ m: (a) DV; (b) SV; (c) MV.

4.2   The two-fluid model for particles

The TFM was adopted to trace the transmission of particles under indoor ventilation systems. The experiment of Liu et al. [65] was used, where the velocity, temperature, and concentration of tracer particles in a large office under DV and MV were measured.

4.2.1   Case description and numerical method

As shown in Figure 4.6a, the dimensions of the office were length (x) $\times$ width (y) $\times$ height (z) = 7 m $\times$ 5.8 m $\times$ 3.05 m. The DV inlet was located on the left wall ($x = 0$ m), two MV inlets were located on the ceiling, and the exhaust was in a corner of the ceiling. In the office, there were four manikins (A, B, C, and D), four desks, four chairs, and four computers (system unit and monitor on the desk). The thermal effect of the human body was modeled by heating the manikin with a direct electrical current. The heat production was controlled at around 80 W for each manikin. There was also one TV on the front wall ($y = 5.8$ m), one table in the corner, and ten 64 W fluorescents on the ceiling. The solid droplet residue without further evaporating was used as tracer particles. Their sizes ranged from 0.3 µm to 2 µm. They were injected into the office from the emitter in front of the mouth of the manikin A at a velocity of 1.58 m s^{-1}, and the injection was cycling as 0.8 s on and 1.2 s off. During the experiment, the profiles of velocity, temperature, and particle concentration were measured at four vertical sampling lines as shown in Figure 4.6b. Furthermore, the temperature of some heated surfaces was measured to provide the temperature boundary conditions for the simulations.

(a)   (b)
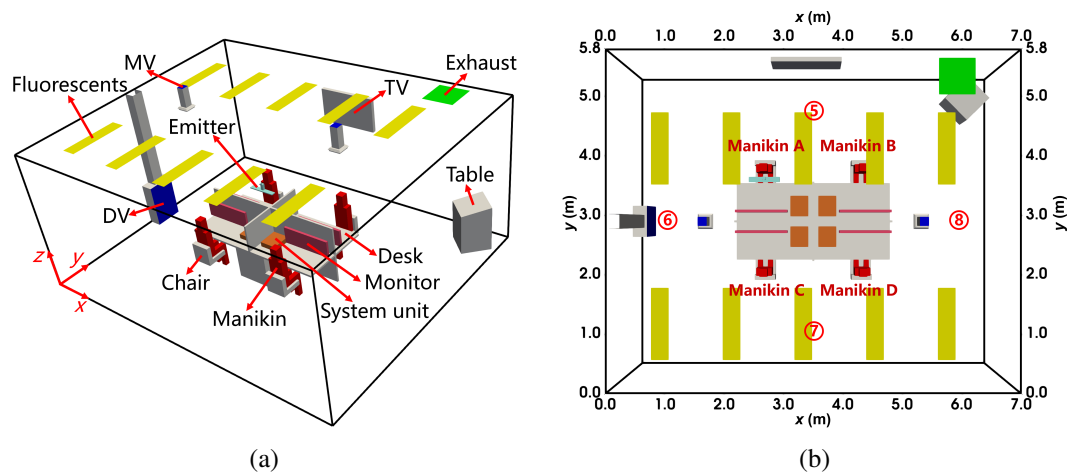
Fig. 4.6 The configuration of the large office with DV and MV: (a) the layout; (b) the locations of sampling lines. The locations of sampling line 5 to 8 are (x, y) = (3.5 m, 4.8 m), (1.0 m, 2.9 m), (3.5 m, 1.0 m), (6.0 m, 2.9 m), respectively.

Compared with the experimental configuration, some simplifications were made to model the geometry. In addition to the simplifications of keyboards, and cables of the computers, the manikins and chairs were simplified by using a combination

of cuboids of similar sizes. The diffuser of DV was simplified as in Section 4.1, while the geometry of the MV inlet was built as in the experiment. Furthermore, the round pipes for the ventilation systems were replaced with square pipes. These simplifications significantly reduce the complexity of the grid and the number of the cells, and are proved to be reasonable by the results in the later part.

The experimental setups, where the supplied air flow rates were equal to 4 ACH, were adopted for the simulations. For the case of DV, its diffuser had a perforated area ratio of 20%, from which the inlet velocity was calculated, and specified using the method of Zhang et al. [198] as in Section 4.1. For the case of MV, a uniform inlet velocity for the 4 ACH scenario was specified at the two MV inlets. The temperatures obtained from experimental measurements were specified for walls and surfaces. For the fluorescents, the fixed temperature boundary conditions were used in the simulations which had been adjusted to match the given power rate. For the particle emitter, a constant velocity of $1.58\,\mathrm{m\,s^{-1}}$, not varying with time, was specified as in the E-L approach simulation of Liu et al. [65] and the volume fraction of the particles was set as 1×10^{-6}.

The TFM was adopted for the transient simulations of particle transmission. Both air and particles were treated as a continuum and two sets of N-S equations for the two phases were solved. The diameter of the dispersed phase was set as $0.4\,\mathrm{\mu m}$ because the experiment focused on particles of this size. For the interphase interactions, only drag force and heat transfer were considered. The former was evaluated using the model of Schiller and Naumann, while the latter was calculated using the Ranz-Marshall correlation [203]. The RNG $k - \varepsilon$ model was used for the continuous air phase, and the dispersed particles phase was assumed to be laminar. A constant thermal physical model was used. The second-order schemes were used to discretize the governing equations. Furthermore, considering the small sizes of the particles, the PSPM, solving a particle concentration transport equation, was also adopted here, and compared with the TFM. The turbulent diffusivity is calculated using $\mathrm{Sc_t} = 0.7$ and the molecular diffusivity of CO_2 ($1.4 \times 10^{-5}\,\mathrm{m^2 s^{-1}}$) is specified for the particles. This is reasonable because turbulent diffusion generally overwhelms molecular diffusion, making the value of molecular diffusivity less influential.

The simulations were performed on hexahedral grids that were refined in the regions near walls, surfaces, and especially the particle emitter. The grid convergence was examined using three grids having 964947 (coarse), 1965986 (medium), and

4571857 (fine) cells, respectively. The medium grid having 1965986 cells was found to be consistent with the results of the fine grid, so it was adopted for the simulations in this study. The details can be found in Appendix E.3. Additionally, to further reduce the computational costs, in the simulations of DV, the geometries of the two MV inlets were removed.

4.2.2   Results and discussion

Figure 4.7 presents the air velocity, air temperature, and normalized particle concentration profiles under DV obtained from experimental measurements, PSPM, and TFM. Figure 4.7a gives the air velocity magnitude. It can be seen that the results obtained using the TFM and the PSPM are close and show good agreement with the experimental data. Because the DV supplies fresh cool air from the lower part of the office as shown in Figure 4.6a, velocity is higher near the floor. This is especially remarkable at location 6 because it is closer to the DV inlet as shown in Figure 4.6b. Additionally, there are differences, though not significant, between the results of TFM and PSPM. This is because the TFM takes the effect of particles on airflow into account, which, though small due to the small size and concentration of the particles, does make some difference. Figure 4.7b presents the temperature profiles. the results obtained using the two numerical methods are close and agree well with the measurement. The cool air enters the office in the lower part, so the temperature is lower near the floor. In the upper part of the office, the temperature is higher due to the thermal effect of the heat sources, such as manikins and fluorescents.

The normalized particle concentration, C^*, is shown in Figure 4.7c. It is defined as $C^* = (C - C_s)/(C_e - C_s)$, where C, C_s, and C_e are the particle concentration at a specific location, at the supply, and at the exhaust, respectively. It can be seen that the concentration profiles predicted by the TFM agree well with the experimental data at Location 5 and 7, but are lower than experimental data at Location 6 and 8. In fact, Location 6 is close to the DV inlet, so the particles tend to be transported away from this region. Location 8 is far from the particle emitter and is obstructed by desks and barriers so that few particles are transported here. Similar underpredictions were also found in the numerical results of Liu et al. [65], and they attributed such differences to the simplifications of the geometry and boundary conditions.

(a)

(b)

(c)

Fig. 4.7 The predicted and measured results along the sampling lines in the large office under DV: (a) air velocity magnitude; (b) air temperature; (c) normalized particle concentration. Circles: experimental data [65]; red solid lines: numerical results of the PSPM; blue dashed lines: numerical results of the TFM.

Furthermore, it can be noted that the results obtained using the PSPM are close to those using the TFM at Location 6 and 8 but different at Location 5 and 7. This is because the two methods solve different equations to trace the transmission of particles. The PSPM solves Eq. (2.5) to obtain the particle concentration, while the TFM solves Eq. (2.8) to obtain the particle volume fraction. It is clear that the former contains a diffusion term and the latter considers the interactions between particles and air through the velocity in the convection term. In this study, the particle emitting velocity is along the direction from Location 5 to 7 (y axis) but perpendicular to the direction from Location 6 to 8 (x axis). Therefore, the particle transport is mainly influenced by diffusion at Location 6 and 8, whereas it is primarily driven

by convection at Location 5 and 7. The interphase interaction in the TFM is not significant due to the small particle size. However, the diffusion term in PSPM seems strong. It is mainly contributed by the turbulent diffusion. The default $Sc_t = 0.7$ results in the magnitude of turbulent diffusivity in most regions being of the order of 1×10^{-3}, which is much larger than the molecular diffusivity. Finally, at Location 6 and 8, governed by diffusion, the additional strong diffusion term of the PSPM does not result in a significant difference from the TFM. However, at Location 5 and 7, governed by convection, the diffusion term of the PSPM makes its results more diffusive than those of the TFM, and thus lower than the experimental data.
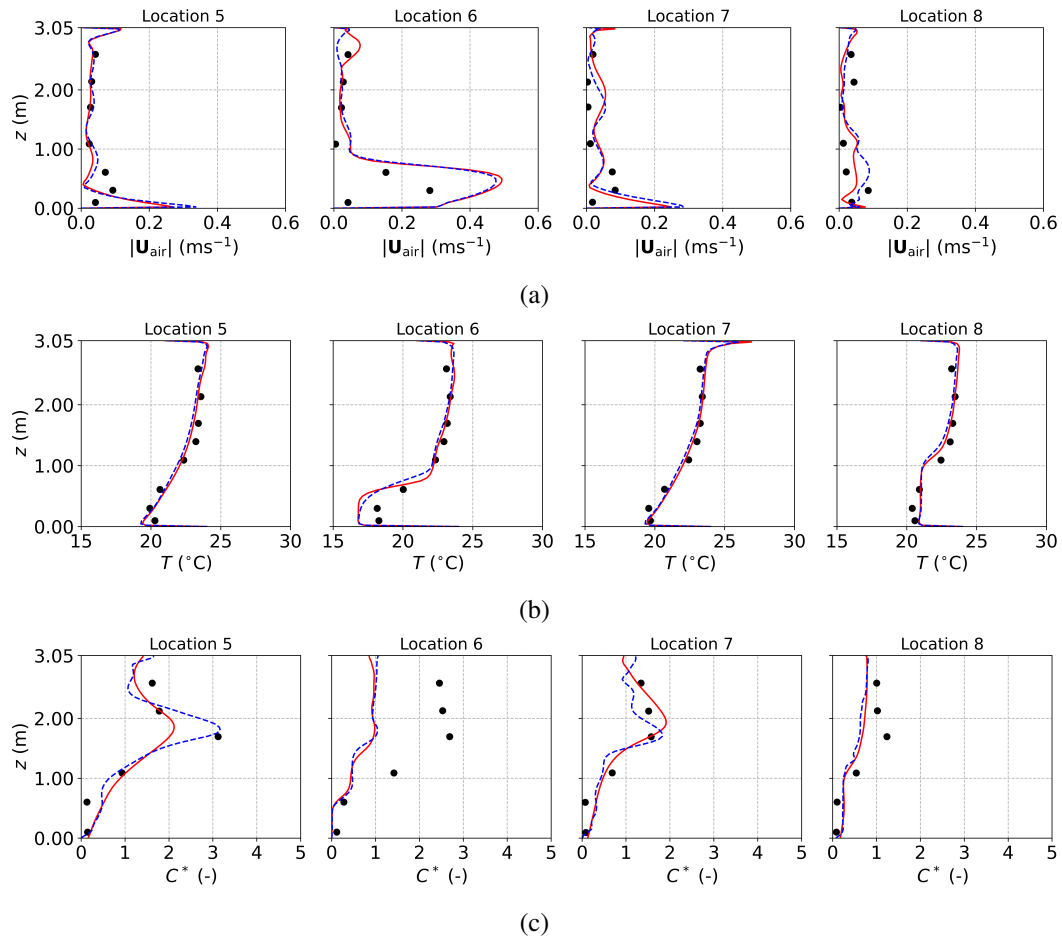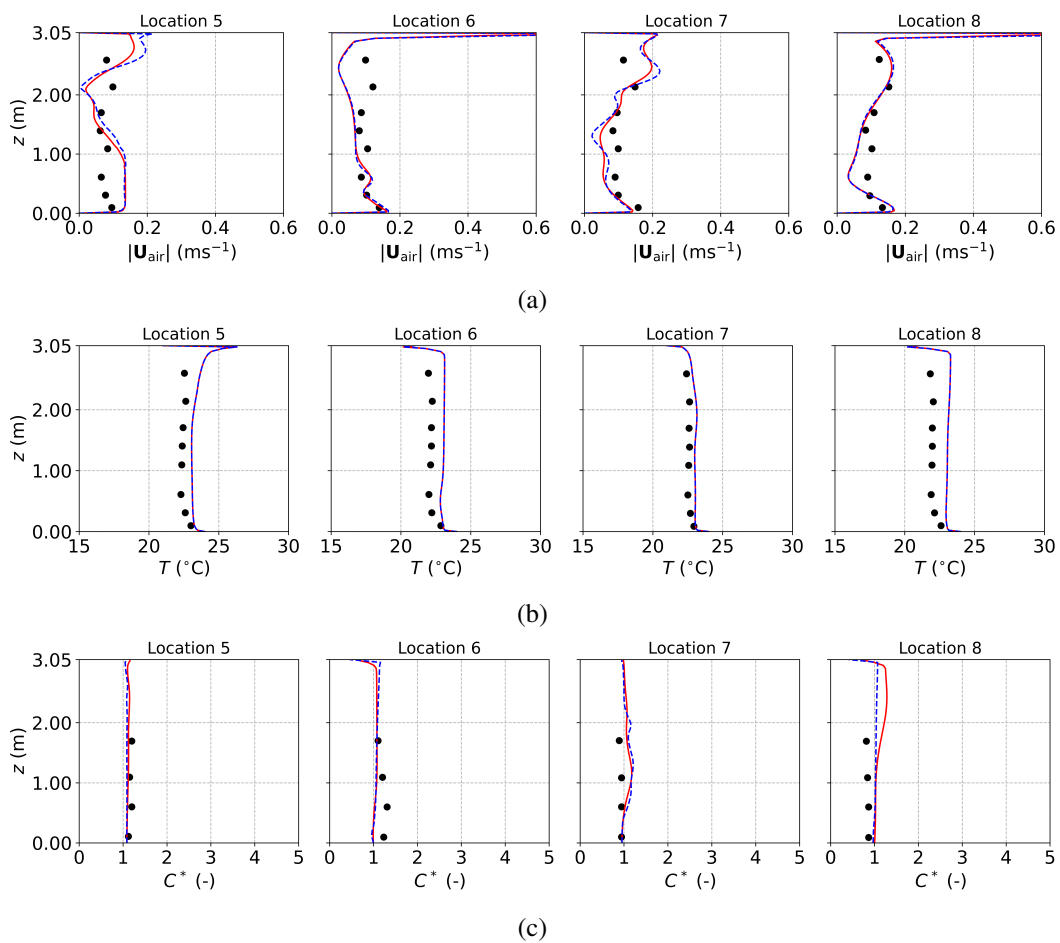

Fig. 4.8 The predicted and measured results along the sampling lines in the large office under MV: (a) air velocity magnitude; (b) air temperature; (c) normalized particle concentration. Circles: experimental data [65]; red solid lines: numerical results of the PSPM; blue dashed lines: numerical results of the TFM.

Figure 4.8 presents the air velocity, air temperature, and normalized particle concentration profiles under MV. It can be seen that the results of the TFM and the PSPM are close and agree well with the experimental data. This is because the MV tends to provide a uniform environment through a full mixing as shown in Figure 4.8b and Figure 4.8c. The diffusion term in the PSPM makes little difference in such a uniform environment, so the PSPM gives results similar to the TFM.

(a)

(b)

(c)

(d)

Fig. 4.9 The magnitude and direction of air and particles velocity in the large office obtained using TFM in the plane of $x = 2.55$ m: (a) air velocity under DV; (b) particles velocity under DV; (c) air velocity under MV; (d) particles velocity under MV.

Figure 4.9 gives the air and particle velocity obtained using the TFM in the vertical plane of $x = 2.55$ m. Comparing Figure 4.9a with Figure 4.9b, or Figure 4.9c with Figure 4.9d, it can be found that the particle velocity is almost identical to the air velocity. The relative difference between the air velocity and the particle velocity is defined as $D_{U_r} = |U_{air} - U_{particles}|/|U_{air}|$. For the case of DV, $D_{U_r} < 0.1\%$ in most of the office and $D_{U_r} < 1.0\%$ in the whole office. Meanwhile, for the case of MV, $D_{U_r} < 0.1\%$ in the whole office. These results indicate that the particles tend to

completely follow the airflow. This feature is confirmed by the values of the Stokes number, defined as $St = \tau_p/\tau_k$, where $\tau_p = \rho_p d_p^2/(18\mu_c)$ is the particle time scale, and $\tau_k = \sqrt{\nu_c/\varepsilon_c}$ is the Kolmogorov time scale. In the calculation, the maximum turbulence dissipation rate ε_c is used to obtain the maximum Stokes number. For the considered size, 0.4 μm, the Stokes number is about 1.94×10^{-4} and 7.32×10^{-4} for DV and MV, respectively. According to the work of Balachandar and Eaton [204], when $St < 0.2$, it is safe to use the PSPM to predict particle transport.

Furthermore, upward buoyant flows above the manikins and the monitors due to thermal effect and gravity are observed in the case of DV as in Figure 4.9a. In the near-floor region, the velocity is also high due to the low inlet location of DV. In the rest of the office, the velocity is relatively low because there are no heat sources driving the airflows. However, under MV as shown in Figure 4.9c, in addition to the buoyant flows similar to DV, the high-speed cool air injected from the ceiling results in large recirculation regions around the manikins and furniture. Therefore, the air velocity in the office is higher than that under DV, which finally results in a full mixing of the indoor air and provides a uniform environment.

Figure 4.10 shows the velocity and normalized concentration distribution in the horizontal plane of $z = 1.12$ m (the height of the particle emitter center). Under DV, as shown in Figure 4.10a, the velocity is high in front of the particle emitter and in the regions near the heated surfaces, such as manikins and monitors. Additionally, it can be noted that in the right part of the office, the velocity is relatively high and points to the left. This is a part of the recirculation caused by the supplied air and the buoyant flows. The supplied air moves along the floor and turns upwards at the right wall ($x = 7$ m), while the buoyant flows move upwards, and then along the ceiling, finally turning downwards at the right wall. They meet in the middle part of the right wall and result in the airflows pointing left. Figure 4.10b gives the normalized concentration C^* distribution. Under DV, after being injected into the office, the particles are transported by the buoyant airflows induced by recirculations to the regions behind the manikin A and C and then dispersed in the office. Due to the obstruction of the barriers and left pointing flows, the particles are seldom transported to the right part of the office, and an environment with relatively low infection risk is provided to the manikin B and D.

Figure 4.10c gives the velocity distribution under MV. It can be seen that the airflows are more complex than those under DV, consisting of recirculations caused

by the buoyant flows and the supplied air. These recirculations provide good mixing of the indoor air, which results in an almost uniform dispersion of particles in the office as shown in Figure 4.10d. This again confirms that DV may be a better choice than MV to control indoor infection.
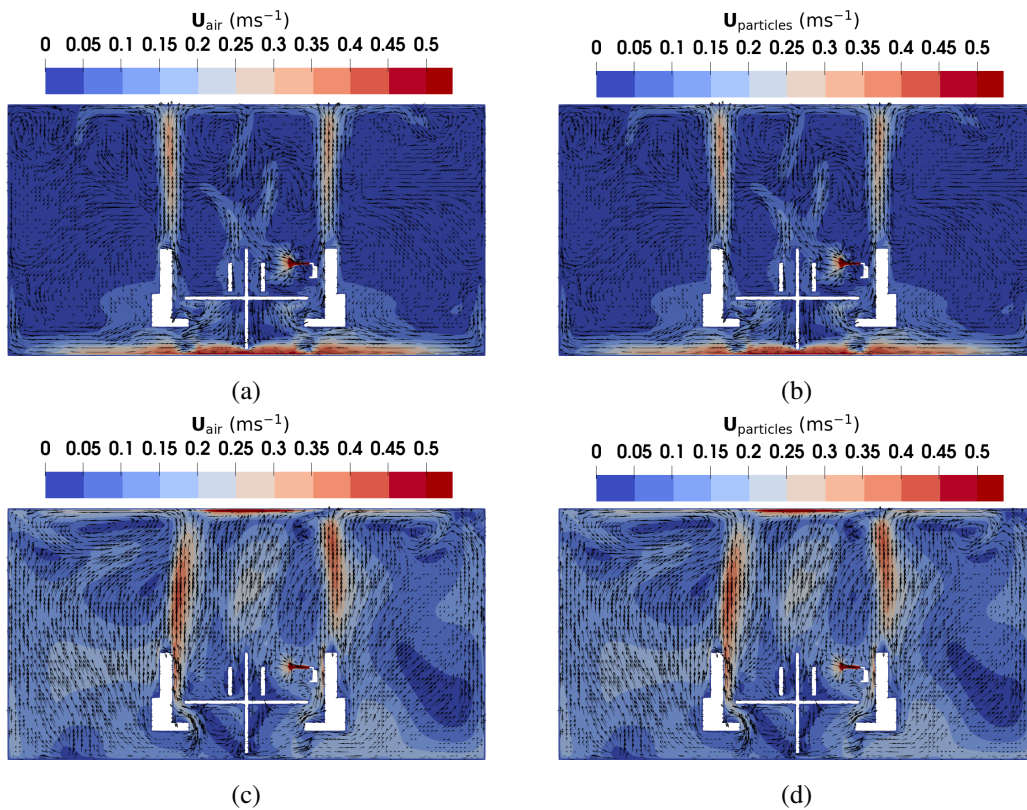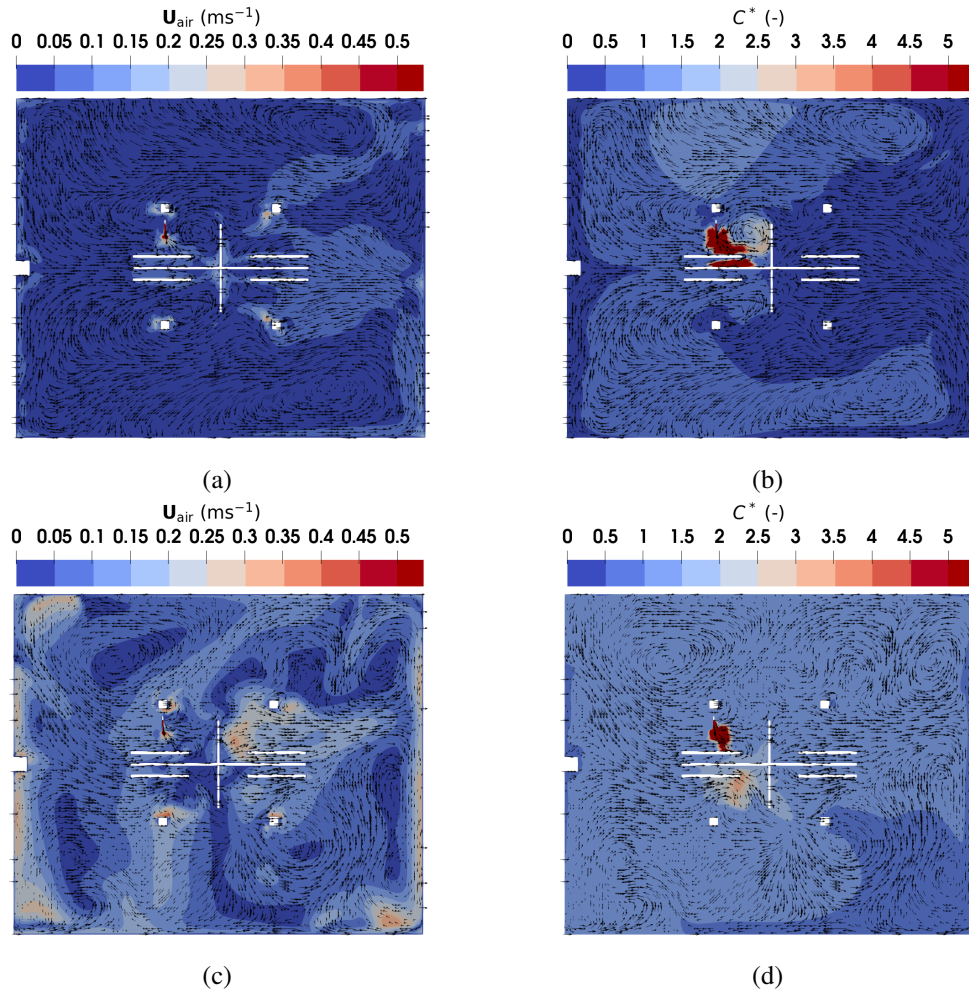

Fig. 4.10 The magnitude and direction of air and particle velocity in the large office obtained using TFM in the plane of $z = 1.12$ m: (a) air velocity under DV; (b) normalized particle concentration under DV; (c) air velocity under MV; (d) normalized particle concentration under MV.

In summary, the TFM can accurately predict the transmission of particles within a narrow size range in ventilated environments. When the particle sizes are small, they tend to completely follow the airflows. In this case, the PSPM can also be used to predict the transmission but special attention should be paid to the diffusion term to avoid too strong diffusion in nonuniform environments.

4.3   The EE-PBE approach for evaporating droplets

The EE-PBE approach was adopted to trace the transmission and evaporation of
the respiratory droplets. The experiment of Wang et al. [68] was used, where the
concentration and size distribution of evaporating droplets in a negative pressure
isolation ward equipped with MV were measured.

4.3.1   Case description and numerical method

The dimensions of the ward, as shown in Figure 4.11a, were length (x) $\times$ width (y)
$\times$ height (z) = 4.22 m $\times$ 2.66 m $\times$ 2.8 m. Two MV inlets with a size of (0.135 m $\times$
0.24 m) were located on the ceiling, and the exhaust with a size of (0.27 m $\times$ 0.27 m)
was in the lower corner of the ward. In the ward, there was one manikin, one bed,
one table, and one equipment belt above the bed. The manikin was heated to keep
a temperature of 34 ± 1 °C. In the simulations, the geometry of the manikin was
simplified by a combination of cuboids of similar sizes. Additionally, there were
two door gaps on the back wall ($y = 0$ m), from which the leaking flows caused
by pressure difference passed through. The measurements showed that the airflow
flowed into the ward from door gap 1 (with the size of 1.14 m $\times$ 0.02 m) at a velocity
of 2 m/s while flowed out of the ward from door gap 2 (with the size of 0.9 m $\times$
0.02 m) at a velocity of 2.3 m/s.

(a)   (b)
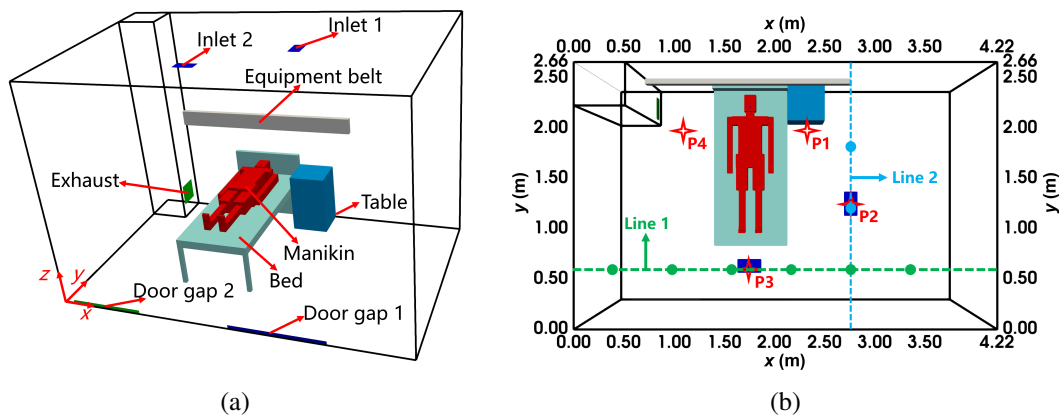
Fig. 4.11 The configuration of the negative pressure isolation ward with MV: (a) the layout;
(b) the locations of sampling lines and points. The location of velocity sampling line 1 is
(y, z) = (0.6 m, 1.5 m) while the location of line 2 is (x, z) = (2.8 m, 1.5 m). The locations
of concentration and size distribution sampling points 1 to 4 are (x, y, z) = (2.27 m, 1.96 m,
1.6 m), (2.76 m, 1.25 m, 1.6 m), (1.75 m, 0.6 m, 1.6 m), (1.1 m, 1.96 m, 1.6 m), respectively.

Table 4.1 Moments at the inlet for the case of droplet transmission in the isolation ward.

Variable	Value
α_d (-)	1×10^{-6}
M_0 (m^{-3})	4.013053×10^{11}
M_1 (m^{-2})	4.936059×10^{5}
M_2 (m^{-1})	8.492310×10^{-1}
M_3 (-)	1.909859×10^{-6}

In the experiment, artificial saliva was used to generate the evaporating tracer droplets. The droplets were injected into the ward from the mouth of the manikin. The measurements showed that the droplet sizes ranged from 0.3 μm to 5 μm. As shown in Figure 4.11b, the profiles of velocity were measured along two horizontal sampling lines while the droplet concentration and size distribution were measured at 4 sampling points.

The boundary conditions were specified according to the experimental setups. A fixed velocity was given at the two MV inlets to provide an air flow rate of 12 ACH for the ward. At the two door gaps, the experimentally measured magnitude and direction of velocity were prescribed. The walls and other surfaces were set as no-slip boundary condition, and a fixed pressure was given at the exhaust. For temperature boundary conditions, the value of 299.1 K was specified for the two MV inlets, and 307.1 K was given for the surface of the manikin. The walls and other surfaces were set as adiabatic. The RH was kept at 60% in the ward. For the droplet emitter, the following boundary conditions were given to model a breath: velocity of 0.5 m s^{-1}; temperature of 309.1 K, and RH of 90%. The mass flow rate of the droplets was not provided in the reference paper. To ensure the continuum assumption, the volume fraction of droplets at the emitter inlet was set as $\alpha_\mathrm{d} = 1 \times 10^{-6}$, which is proved to be reasonable by the following results. The moments were calculated using the measured size distribution at the emitter and are given in Table 4.1.

Since the droplet sizes were distributed in a relatively narrow range, the EE-PBE approach for droplets of varied sizes moving with the same velocity (mono-solver) was adopted for the transient simulations. Schiller and Naumann drag force model, Ranz-Marshall heat transfer model, and Frössling mass transfer model were used for the interphase momentum, heat, and mass exchanges; the RNG $k - \varepsilon$ turbulence

model and laminar behavior were specified for the continuous phase and the dispersed phase, respectively; the temperature and composition-dependent thermal physical model of Appendix D was used. For the setup of the PBE, two quadrature nodes were used, so that four moment transport equations were solved. Additionally, to model the droplet residues in the experiment, a minimum droplet diameter of 1.0 μm was specified, below which the evaporation stops. The first-order upwind scheme was used here to minimize the stability and realizability issues of the QMOM solver.

Hexahedral grids refined in the regions near walls and surfaces were adopted for the simulations. The grid convergence was examined using three grids having 627326 (coarse), 1143714 (medium), and 2280912 (fine) cells, respectively. It was found that the results of the medium grid and the fine grid were close showing good consistency. Therefore, the medium grid having 1143714 cells was adopted for the simulations in this study. The details can be found in Appendix E.4.

4.3.2 Results and discussion

Figure 4.12 compares the predicted velocity profiles and dimensionless concentration with the experimental data. Good agreement is observed, indicating that the EE-PBE coupled approach is reliable in tracing the indoor transmission of evaporating droplets. Figure 4.12a gives the air velocity profile along the sampling line 1. It can be seen that there is a velocity peak centered at $x = 1.75$ m. This is caused by the air supplied from the ventilation inlet 2, which is just above the sampling line 1 as shown in Figure 4.11b. Similarly, as shown in Figure 4.12b, a velocity peak appears just below the ventilation inlet 1 at $y = 1.25$ m. Figure 4.12c presents the dimensionless concentration $\overline{C}_i$. It is calculated by dividing the local concentration by the average concentration at the four measurement points (P1 to P4) as $\overline{C}_i = M_{0,i}/(\sum_{i=1}^{4} M_{0,i}/4)$, $(i = 1, 2, 3, 4)$. Because of the supplied fresh air, the concentration is low in regions below the ventilation inlets, namely, at point 2 and point 3, whereas the concentration is higher at point 1 and point 4, which are located near the droplet emitter at the head of the manikin. In addition, the concentration at point 1 is lower than that at point 4 which is located further from the ventilation inlet. The concentration differences present the ability of the adopted ventilation system to remove or dilute the respiratory droplets.

(a)

(b)

(c)
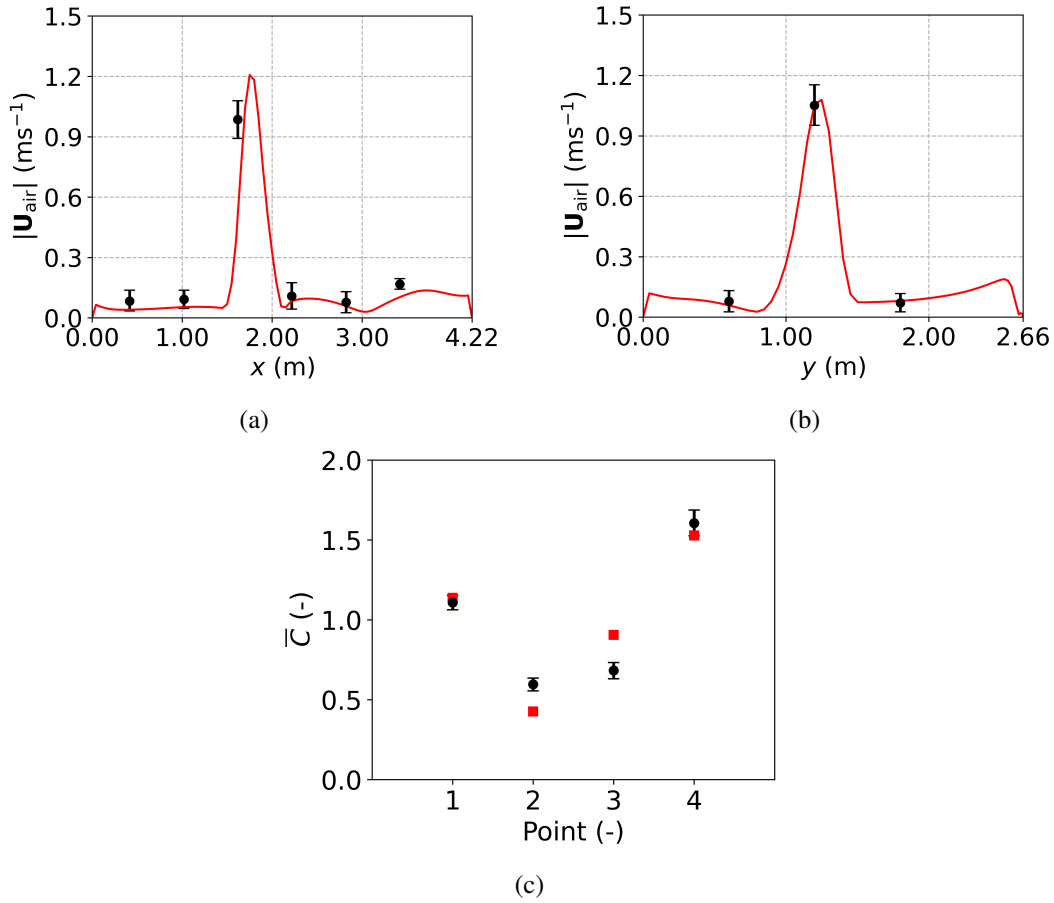
Fig. 4.12 Comparison between simulation results and experimental data in the ward with MV: (a) air velocity profile along line 1; (b) air velocity profile along line 2; (c) dimensionless concentration at the four sampling point. Circles: experimental data [68]; solid lines or squares: numerical results of this study.

Figure 4.13 shows the contour plots of droplet diameter, velocities, and concentration in the plane of $x = 1.685$ m, which passes through the middle section of the manikin. Figure 4.13a presents the Sauter mean diameter of the droplets calculated as $d_d = M_3/M_2$. The droplet diameter at the emitter was calculated using the experimental size distribution and was equal to 2.25 μm. As mentioned above, a minimum diameter of 1 μm is specified to represent the droplet nuclei that are not further evaporating. It can be seen that the droplet diameter is larger than the minimum value only in a small region near the mouth, and in the remaining regions, it is equal to the minimum value. This indicates that the droplets evaporate into nuclei very quickly. This is reasonable since in our previous work [203], we found that droplets with a size of 10 μm might fully evaporate within one second, and smaller droplets

evaporate even faster. This finding is also consistent with the experimental results. Wang et al. [68] measured the droplet size distribution at the four measurement points, and almost identical distributions were found at the four different points. This implies that the droplets evaporate and form nuclei very quickly. Such nuclei are subsequently transported by the airflows to different regions in the ward.

Figure 4.13b and Figure 4.13c give the air and droplet velocities, which are very close due to the small sizes of the droplet nuclei. To reproduce the experimental setup, the human breath is modeled by a droplet-laden flow injected from the mouth of the manikin with a constant velocity, equal to $0.5\,\mathrm{m\,s^{-1}}$, pointing upwards. Therefore, there is an upward flow above the head of the lying manikin. Meanwhile, the fresh air is supplied from the ventilation inlet 2 downwards, developing and decelerating in the ward, finally impinging on the floor and resulting in the airflows in the near floor regions. Additionally, the left part of the supplied air impinges on the bed and forms an airflow pointing left. This airflow, heated by the legs and trunk of the manikin, moves along the manikin's body and finally joins the upward exhaled air. Furthermore, in the left lower corner, close to the exhaust, the velocity is also relatively high. Such indoor airflows determine the distribution of the droplets.

Figure 4.13d gives the droplet number concentration normalized using the inlet value, $C^* = M_0/M_{0,\mathrm{in}}$. Obviously, the concentration is high in the exhaled air near the manikin mouth and is low in the injected air close to the ventilation inlet. Additionally, quickly evaporating into the nuclei, and tending to completely follow the airflow, the droplets are transported by the previously mentioned upward airflows above the manikin head to the upper part of the ward. This is consistent with the numerical results of Wang et al. [68]. They adopted the E-L approach to predict droplet transmission and found that the droplet nuclei mainly concentrated in the upper part of the ward and deposited mostly on the ceiling. This stratified distribution is caused by the incomplete mixing of indoor air. The breathing velocity is relatively low. The fresh air is supplied away from the manikin mouth and pointing downwards. Therefore, the interference between these two flows is relatively weak and leads to incomplete mixing.

In summary, the TFM-PBE coupled approach can be used to trace the transmission of evaporating droplets. The small droplets evaporate into nuclei very quickly and then follow the airflow.

(a)

(b)

(c)

(d)
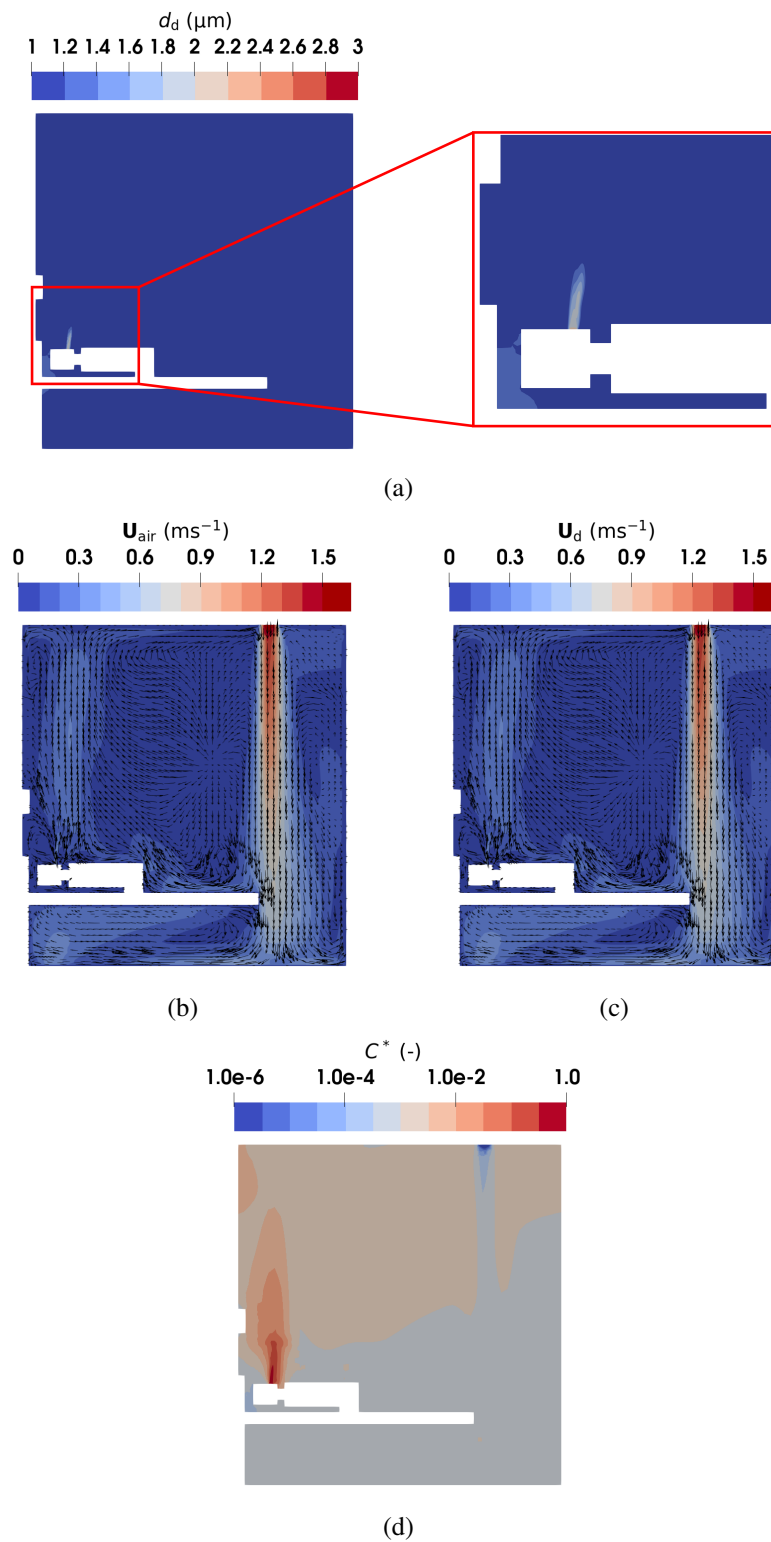
Fig. 4.13 The contour plots of droplets diameter, velocities, and normalized concentration in the ward with MV in the plane of $x = 1.685$ m: (a) droplet Sauter mean diameter; (b) air velocity; (c) droplet velocity; (d) normalized concentration of droplets.

4.4   Summary

In this chapter, the ability of different Eulerian approaches to trace the transmission of different kinds of droplets in ventilated indoor environments is assessed by comparing them with experimental results reported in the literature. The performance of different ventilation systems to dilute or remove the virus-laden respiratory droplets is discussed.

The pseudo-single-phase model is adopted to predict the transmission of a tracer gas that is widely used as a surrogate of small-size respiratory droplets or aerosols in studies of indoor ventilation systems. The experiment tracing CO_2 transmission in an office under DV, SV, and MV is adopted. The predicted CO_2 concentration profiles agree well with the experimental data, indicating the reliability of PSPM. The DV transports the tracer gas to the upper part of the office, providing a stratified environment; the MV disperses the tracer gas uniformly in the office, providing a uniform environment; and the SV supplies the fresh air to the breath zone directly, providing good air quality there. Therefore, the SV is recommended to control indoor infection.

The two-fluid model and the pseudo-single-phase model are used to trace the transmission of particles ranging from 0.3 μm to 2 μm in an office with DV and MV. The results of TFM show good agreement with experimental measurement. The air and particle velocities are almost identical, confirming that the small particles tend to completely follow the airflows. The results of PSPM are close to TFM, except that PSPM underpredicts the concentration in the case of DV due to a strong diffusion. Therefore, PSPM can be used to trace the transmission of small particles but requires a suitable diffusion coefficient. Additionally, similar to the previous case, the stratified environment of DV and the uniform environment of MV, are observed, respectively.

The EE-PBE approach is used to trace the transmission of evaporating droplets in a negative pressure isolation ward. The predicted velocity and concentration profiles agree well with the experimental data. The droplets ranging from 0.3 μm to 10 μm are found to evaporate into nuclei very quickly and accumulate in the upper part of the ward, which is consistent with experimental results. These results present the ability of the EE-PBE approach to accurately the temporal evolution of the sizes and locations of the droplets.

Chapter 5

Conclusions

The COVID-19 pandemic has spread widely around the world and made a huge difference to all aspects of society. It is found to be able to be transmitted by the virus-laden respiratory droplets (or aerosols) exhaled by an infected person. People spend most of their time in indoor environments, such as offices, classrooms, and hospital wards. The ventilation systems, changing the indoor ambient conditions and resulting in different indoor airflow patterns, are widely used to dilute or remove respiratory droplets. Therefore, the knowledge of the transmission of respiratory droplets in ventilated indoor environments is important to break the transmission chain and control the infection.

The transmission of respiratory droplets is a complex multiphase system, whose description must include features such as multiphase flow, polydisperse populations of droplets, multicomponent mass transfer, heat transfer, and evaporation. Computational fluid dynamics provides an efficient and reliable tool to investigate the droplet transmission. The dispersed droplets can be treated in a Lagrangian manner or in an Eulerian manner. The former tracks the movement of a number of droplets individually. It can easily deal with the polydispersity and evaporation of the droplets but may require high computational costs. The latter treats the dispersed droplets as a continuum, either being in the same phase with the air or being an additional continuous phase interpenetrating with the air phase. Although dealing with the polydispersity of the population and the evaporation of the droplets is more complex in an Eulerian framework than in a Lagrangian one, the Eulerian approach gener-

ally has lower costs, which makes it promising in the numerical study of droplet transmission in ventilated indoor environments.

In this dissertation, to fully exploit the advantage of the lower costs of the Eulerian approach, the population balance equation is coupled with the Eulerian-Eulerian approach to trace the transmission of the polydispersed evaporating respiratory droplets in indoor environments equipped with ventilation systems. The related codes are developed based on the open-source software OpenFOAM and its module OpenQBMM and are verified and validated using the experimental and numerical data in the literature. Different Eulerian approaches are adopted to investigate the transmission of different kinds of respiratory droplets under different ventilation systems. The conclusions are drawn as follows.

In Chapter 2, different Eulerian approaches, including the pseudo-single-phase model and the Eulerian-Eulerian approach (multi-fluid model), are reported first. Then, the population balance equation and its coupling with the Eulerian-Eulerian approach are presented. The algorithms for two PBE solving methods, the sectional method (SM) and the quadrature method of moments (QMOM), are illustrated.

In Chapter 3, the developed EE-PBE approach for the transmission and evaporation of polydispersed respiratory droplets is systematically verified and validated with experimental or numerical data from the literature. This is performed by first assessing the different aspects of the transmission process using the experimental and numerical results in the literature, including evaporation, movement of the respiratory jet (or puff), and particle transmission in ventilated environments. Good agreements are found, indicating that the EE-PBE approach is capable of dealing with the different aspects of droplet transmission. Finally, all features are collectively considered through the examination of the transmission of polydispersed evaporating cough droplets in a 3D chamber. The SM-solver and the QMOM poly-solver are adopted and compared. The suspending trends of small droplets and the falling trends of large droplets are currently reproduced by both approaches. The droplets are found to be able to travel a distance longer than 2 m, which is valuable for the guidelines of social distancing. Additionally, the advantages and disadvantages of the two methods are discussed. Both methods can directly provide variables, like volume fraction for analyses. Compared with SM, which needs a preliminary subdivision of the population of droplets in classes, no user intervention is required for QMOM, which is free of unreasonable results caused by inappropriate criteria.

In Chapter 4, the ability of different Eulerian approaches to trace the transmission of different kinds of droplets in ventilated indoor environments is assessed by comparing them with experimental results reported in the literature, and the performances of different ventilation systems are discussed. The PSPM is adopted to predict the transmission of tracer gas, the surrogate of small-size respiratory droplets or aerosols, in an office under DV, SV, and MV. The predicted results agree well with the experimental data, indicating the reliability of the PSPM. The DV transports the tracer gas to the upper part of the office, providing a stratified environment; the MV disperses the tracer gas uniformly in the office, providing a uniform environment; and the SV supplies the fresh air to the breath zone directly, providing good air quality there. Therefore, the SV is recommended to control indoor infection. The TFM and PSPM are used to trace the transmission of tracer particles ranging from 0.3 μm to 2 μm in an experimental office with DV and MV. The results of TFM show good agreement with measurement. The air and particle velocities are almost identical, confirming that the small particles tend to completely follow the airflows. The results of PSPM are close to TFM, except that PSPM underpredicts the concentration in the case of DV due to a strong diffusion. Therefore, PSPM can be used to trace the transmission of small particles but requires a suitable diffusion coefficient. Additionally, similar to the previous case, the stratified environment of DV and the uniform environment of MV are observed. Finally, the EE-PBE approach is used to trace the transmission of evaporating droplets in a negative pressure isolation ward. The predicted velocity and concentration profiles agree well with the experimental data. The droplets ranging from 0.3 μm to 10 μm are found to evaporate into nuclei very quickly and accumulate in the upper part of the ward, which is consistent with experimental results. These results present the ability of the EE-PBE approach to accurately the temporal evolution of the sizes and locations of the droplets.

In conclusion, the developed EE-PBE approach is proven to be able to trace the transmission of polydispersed evaporating respiratory droplets. The different Eulerian approaches, capable of dealing with different kinds of respiratory droplets, provide reliable and efficient tools for studies on respiratory droplet transmission in ventilated indoor environments. In future works, the multi-component composition of respiratory droplets, affecting evaporation, will be considered to reveal the droplet transport under real-world conditions. Meanwhile, the droplet residence time will be analyzed using the mean age theory to evaluate the performance of different indoor ventilation systems.

References

[1] WHO, "Transmission of sars-cov-2: Implications for infection prevention precautions," tech. rep., World Health Organization, July 2020.

[2] L. Ferretti, C. Wymant, M. Kendall, L. Zhao, A. Nurtay, L. Abeler-Dörner, M. Parker, D. Bonsall, and C. Fraser, "Quantifying sars-cov-2 transmission suggests epidemic control with digital contact tracing," *Science*, vol. 368, p. eabb6936, May 2020.

[3] C. C. Wang, K. A. Prather, J. Sznitman, J. L. Jimenez, S. S. Lakdawala, Z. Tufekci, and L. C. Marr, "Airborne transmission of respiratory viruses," *Science*, vol. 373, p. eabd9149, Aug. 2021.

[4] J. L. Santarpia, D. N. Rivera, V. L. Herrera, M. J. Morwitzer, H. M. Creager, G. W. Santarpia, K. K. Crown, D. M. Brett-Major, E. R. Schnaubelt, M. J. Broadhurst, J. V. Lawler, S. P. Reid, and J. J. Lowe, "Aerosol and surface contamination of sars-cov-2 observed in quarantine and isolation care," *Scientific Reports*, vol. 10, p. 12732, July 2020.

[5] P. Y. Chia, K. K. Coleman, Y. K. Tan, S. W. X. Ong, M. Gum, S. K. Lau, X. F. Lim, A. S. Lim, S. Sutjipto, P. H. Lee, T. T. Son, B. E. Young, D. K. Milton, G. C. Gray, S. Schuster, T. Barkham, P. P. De, S. Vasoo, M. Chan, B. S. P. Ang, B. H. Tan, Y.-S. Leo, O.-T. Ng, M. S. Y. Wong, and K. Marimuthu, "Detection of air and surface contamination by sars-cov-2 in hospital rooms of infected patients," *Nature Communications*, vol. 11, p. 2800, May 2020.

[6] J. A. Lednicky, M. Lauzardo, Z. H. Fan, A. Jutla, T. B. Tilly, M. Gangwar, M. Usmani, S. N. Shankar, K. Mohamed, A. Eiguren-Fernandez, C. J. Stephenson, M. M. Alam, M. A. Elbadry, J. C. Loeb, K. Subramaniam, T. B. Waltzek, K. Cherabuddi, J. G. Morris, and C.-Y. Wu, "Viable sars-cov-2 in the air of a hospital room with covid-19 patients," *International Journal of Infectious Diseases*, vol. 100, pp. 476–482, Nov. 2020.

[7] Y. Liu, Z. Ning, Y. Chen, M. Guo, Y. Liu, N. K. Gali, L. Sun, Y. Duan, J. Cai, D. Westerdahl, X. Liu, K. Xu, K.-f. Ho, H. Kan, Q. Fu, and K. Lan, "Aerodynamic analysis of sars-cov-2 in two wuhan hospitals," *Nature*, vol. 582, pp. 557–560, June 2020.

[8] J. L. Santarpia, V. L. Herrera, D. N. Rivera, S. Ratnesar-Shumate, S. P. Reid, D. N. Ackerman, P. W. Denton, J. W. S. Martens, Y. Fang, N. Conoan, M. V. Callahan, J. V. Lawler, D. M. Brett-Major, and J. J. Lowe, "The size and culturability of patient-generated sars-cov-2 aerosol," *Journal of Exposure Science & Environmental Epidemiology*, vol. 32, pp. 706–711, Sept. 2022.

[9] M. Schuit, S. Ratnesar-Shumate, J. Yolitz, G. Williams, W. Weaver, B. Green, D. Miller, M. Krause, K. Beck, S. Wood, B. Holland, J. Bohannon, D. Freeburger, I. Hooper, J. Biryukov, L. A. Altamura, V. Wahl, M. Hevey, and P. Dabisch, "Airborne sars-cov-2 is rapidly inactivated by simulated sunlight," *The Journal of Infectious Diseases*, vol. 222, pp. 564–571, July 2020.

[10] S. J. Smither, L. S. Eastaugh, J. S. Findlay, and M. S. Lever, "Experimental aerosol survival of sars-cov-2 in artificial saliva and tissue culture media at medium and high humidity," *Emerging Microbes & Infections*, vol. 9, pp. 1415–1417, Jan. 2020.

[11] N. van Doremalen, T. Bushmaker, D. H. Morris, M. G. Holbrook, A. Gamble, B. N. Williamson, A. Tamin, J. L. Harcourt, N. J. Thornburg, S. I. Gerber, J. O. Lloyd-Smith, E. de Wit, and V. J. Munster, "Aerosol and surface stability of sars-cov-2 as compared with sars-cov-1," *New England Journal of Medicine*, vol. 382, pp. 1564–1567, Apr. 2020.

[12] H. A. Aboubakr, T. A. Sharafeldin, and S. M. Goyal, "Stability of sars-cov-2 and other coronaviruses in the environment and on common touch surfaces and the influence of climatic conditions: A review," *Transboundary and Emerging Diseases*, vol. 68, no. 2, pp. 296–312, 2021.

[13] J. Xu, C. Xu, R. Chen, Y. Yin, Z. Wang, K. Li, J. Shi, X. Chen, J. Huang, J. Hong, R. Yuan, Y. Liu, R. Liu, Y. Wang, X. Liu, and Z. Zhang, "Stability of sars-cov-2 on inanimate surfaces: A review," *Microbiological Research*, vol. 272, p. 127388, July 2023.

[14] N. E. Klepeis, W. C. Nelson, W. R. Ott, J. P. Robinson, A. M. Tsang, P. Switzer, J. V. Behar, S. C. Hern, and W. H. Engelmann, "The national human activity pattern survey (nhaps): A resource for assessing exposure to environmental pollutants," *Journal of Exposure Science & Environmental Epidemiology*, vol. 11, pp. 231–252, July 2001.

[15] Y. Li, G. M. Leung, J. W. Tang, X. Yang, C. Y. H. Chao, J. Z. Lin, J. W. Lu, P. V. Nielsen, J. Niu, H. Qian, A. C. Sleigh, H.-J. J. Su, J. Sundell, T. W. Wong, and P. L. Yuen, "Role of ventilation in airborne transmission of infectious agents in the built environment? a multidisciplinary systematic review," *Indoor Air*, vol. 17, pp. 2–18, Feb. 2007.

[16] S. Balachandar, S. Zaleski, A. Soldati, G. Ahmadi, and L. Bourouiba, "Host-to-host airborne transmission as a multiphase flow problem for science-based social distance guidelines," *International Journal of Multiphase Flow*, vol. 132, p. 103439, Nov. 2020.

[17] J. Liu and Y. Duan, "Saliva: A potential media for disease diagnostics and monitoring," *Oral Oncology*, vol. 48, pp. 569–577, July 2012.

[18] W. F. Wells, "On air-borne infections: Study ii. droplets and droplet nuclei," *American Journal of Epidemiology*, vol. 20, pp. 611–618, Nov. 1934.

[19] J. Gralton, E. Tovey, M.-L. McLaws, and W. D. Rawlinson, "The role of particle size in aerosolised pathogen transmission: A review," *Journal of Infection*, vol. 62, pp. 1–13, Jan. 2011.

[20] G. Johnson, L. Morawska, Z. Ristovski, M. Hargreaves, K. Mengersen, C. Chao, M. Wan, Y. Li, X. Xie, D. Katoshevski, and S. Corbett, "Modality of human expired aerosol size distributions," *Journal of Aerosol Science*, vol. 42, pp. 839–851, Dec. 2011.

[21] H. F. Eichenwald, "The "cloud baby": An example of bacterial-viral interaction," *Archives of Pediatrics & Adolescent Medicine*, vol. 100, p. 161, Aug. 1960.

[22] R. S. Papineni and F. S. Rosenthal, "The size distribution of droplets in the exhaled breath of healthy human subjects," *Journal of Aerosol Medicine*, vol. 10, pp. 105–116, Jan. 1997.

[23] P. Fabian, J. J. McDevitt, W. H. DeHaan, R. O. P. Fung, B. J. Cowling, K. H. Chan, G. M. Leung, and D. K. Milton, "Influenza virus in human exhaled breath: An observational study," *PLoS ONE*, vol. 3, p. e2691, July 2008.

[24] L. Morawska, G. Johnson, Z. Ristovski, M. Hargreaves, K. Mengersen, S. Corbett, C. Chao, Y. Li, and D. Katoshevski, "Size distribution and sites of origin of droplets expelled from the human respiratory tract during expiratory activities," *Journal of Aerosol Science*, vol. 40, pp. 256–269, Mar. 2009.

[25] H. Holmgren, E. Ljungström, A.-C. Almstrand, B. Bake, and A.-C. Olin, "Size distribution of exhaled particles in the range from 0.01 to 2.0μm," *Journal of Aerosol Science*, vol. 41, pp. 439–446, May 2010.

[26] J. P. Duguid, "The size and the duration of air-carriage of respiratory droplets and droplet-nuclei," *Epidemiology and Infection*, vol. 44, pp. 471–479, Sept. 1946.

[27] R. G. Loudon and R. M. Roberts, "Droplet expulsion from the respiratory tract," *American Review of Respiratory Disease*, vol. 95, no. 3, 1967.

[28] C. Chao, M. Wan, L. Morawska, G. Johnson, Z. Ristovski, M. Hargreaves, K. Mengersen, S. Corbett, Y. Li, X. Xie, and D. Katoshevski, "Characterization of expiration air jets and droplet size distributions immediately at the mouth opening," *Journal of Aerosol Science*, vol. 40, pp. 122–133, Feb. 2009.

[29] X. Xie, Y. Li, H. Sun, and L. Liu, "Exhaled droplets due to talking and coughing," *Journal of The Royal Society Interface*, vol. 6, Dec. 2009.

[30] S. Yang, G. W. M. Lee, C.-M. Chen, C.-C. Wu, and K.-P. Yu, "The size and concentration of droplets generated by coughing in human subjects," *Journal of Aerosol Medicine*, vol. 20, no. 4, pp. 484–494, 2007.

[31] F. E. Buckland and D. A. J. Tyrrell, "Experiments on the spread of colds: 1. laboratory studies on the dispersal of nasal secretion," *Journal of Hygiene*, vol. 62, pp. 365–377, Sept. 1964.

[32] A. Bahramian, M. Mohammadi, and G. Ahmadi, "Effect of indoor temperature on the velocity fields and airborne transmission of sneeze droplets: An experimental study and transient cfd modeling," *Science of The Total Environment*, vol. 858, p. 159444, Feb. 2023.

[33] R. Mittal, R. Ni, and J.-H. Seo, "The flow physics of covid-19," *Journal of Fluid Mechanics*, vol. 894, p. F2, July 2020.

[34] J. K. Gupta, C.-H. Lin, and Q. Chen, "Characterizing exhaled airflow from breathing and talking," *Indoor Air*, vol. 20, pp. 31–39, Feb. 2010.

[35] J. W. Tang, A. Nicolle, J. Pantelic, G. C. Koh, L. D. Wang, M. Amin, C. A. Klettner, D. K. W. Cheong, C. Sekhar, and K. W. Tham, "Airflow dynamics of coughing in healthy human volunteers by shadowgraph imaging: An aid to aerosol infection control," *PLoS ONE*, vol. 7, p. e34818, Apr. 2012.

[36] J. W. Tang, A. D. Nicolle, C. A. Klettner, J. Pantelic, L. Wang, A. B. Suhaimi, A. Y. L. Tan, G. W. X. Ong, R. Su, C. Sekhar, D. D. W. Cheong, and K. W. Tham, "Airflow dynamics of human jets: Sneezing and breathing - potential sources of infectious aerosols," *PLoS ONE*, vol. 8, p. e59970, Apr. 2013.

[37] C. Xu, P. V. Nielsen, G. Gong, L. Liu, and R. L. Jensen, "Measuring the exhaled breath of a manikin and human subjects," *Indoor Air*, vol. 25, no. 2, pp. 188–197, 2015.

[38] C. Xu, P. V. Nielsen, L. Liu, R. L. Jensen, and G. Gong, "Human exhalation characterization with the aid of schlieren imaging technique," *Building and Environment*, vol. 112, pp. 190–199, Feb. 2017.

[39] P. Fabian, J. Brain, E. A. Houseman, J. Gern, and D. K. Milton, "Origin of exhaled breath particles from healthy and human rhinovirus-infected subjects," *Journal of Aerosol Medicine and Pulmonary Drug Delivery*, vol. 24, pp. 137–147, June 2011.

[40] J. W. Tang, T. J. Liebner, B. A. Craven, and G. S. Settles, "A schlieren optical study of the human cough with and without wearing masks for aerosol infection control," *Journal of The Royal Society Interface*, vol. 6, Dec. 2009.

[41] S.-B. Kwon, J. Park, J. Jang, Y. Cho, D.-S. Park, C. Kim, G.-N. Bae, and A. Jang, "Study on the initial velocity distribution of exhaled air from coughing and speaking," *Chemosphere*, vol. 87, pp. 1260–1264, June 2012.

[42] A. Giovanni, T. Radulesco, G. Bouchet, A. Mattei, J. Révis, E. Bogdanski, and J. Michel, "Transmission of droplet-conveyed infectious agents such as sars-cov-2 by speech and vocal exercises during speech therapy: Preliminary experiment concerning airflow velocity," *European Archives of Oto-Rhino-Laryngology*, vol. 278, pp. 1687–1692, May 2021.

[43] Z. P. Tan, L. Silwal, S. P. Bhatt, and V. Raghav, "Experimental characterization of speech aerosol dispersion dynamics," *Scientific Reports*, vol. 11, p. 3953, Feb. 2021.

[44] M. Han, R. Ooka, H. Kikumoto, W. Oh, Y. Bu, and S. Hu, "Experimental measurements of airflow features and velocity distribution exhaled from sneeze and speech using particle image velocimetry," *Building and Environment*, vol. 205, p. 108293, Nov. 2021.

[45] S. Zhu, S. Kato, and J.-H. Yang, "Study on transport characteristics of saliva droplets produced by coughing in a calm indoor environment," *Building and Environment*, vol. 41, pp. 1691–1702, Dec. 2006.

[46] J. K. Gupta, C.-H. Lin, and Q. Chen, "Flow dynamics and characterization of a cough: Flow dynamics and characterization of a cough," *Indoor Air*, vol. 19, pp. 517–525, Dec. 2009.

[47] M. Han, R. Ooka, H. Kikumoto, W. Oh, Y. Bu, and S. Hu, "Measurements of exhaled airflow velocity through human coughs using particle image velocimetry," *Building and Environment*, vol. 202, p. 108020, Sept. 2021.

[48] M. VanSciver, S. Miller, and J. Hertzberg, "Particle image velocimetry of human cough," *Aerosol Science and Technology*, vol. 45, pp. 415–422, Feb. 2011.

[49] B. E. Scharfman, A. H. Techet, J. W. M. Bush, and L. Bourouiba, "Visualization of sneeze ejecta: Steps of fluid fragmentation leading to respiratory droplets," *Experiments in Fluids*, vol. 57, p. 24, Feb. 2016.

[50] H. Nishimura, S. Sakata, and A. Kaga, "A new methodology for studying dynamics of aerosol particles in sneeze and cough using a digital high-vision, high-speed video system and vector analyses," *PLoS ONE*, vol. 8, p. e80244, Nov. 2013.

[51] M. Fan, Z. Fu, J. Wang, Z. Wang, H. Suo, X. Kong, and H. Li, "A review of different ventilation modes on thermal comfort, air quality and virus spread control," *Building and Environment*, vol. 212, p. 108831, Mar. 2022.

[52] X. Li, Y. Shang, Y. Yan, L. Yang, and J. Tu, "Modelling of evaporation of cough droplets in inhomogeneous humidity fields using the multi-component eulerian-lagrangian approach," *Building and Environment*, vol. 128, pp. 68–76, Jan. 2018.

[53] G. Zeng, L. Chen, H. Yuan, A. Yamamoto, and S. Maruyama, "Evaporation flow characteristics of airborne sputum droplets with solid fraction: Effects of humidity field evolutions," *Physics of Fluids*, vol. 33, p. 123308, Dec. 2021.

[54] S. Zhang, Z. Lin, Z. Ai, F. Wang, Y. Cheng, and C. Huan, "Effects of operation parameters on performances of stratum ventilation for heating mode," *Building and Environment*, vol. 148, pp. 55–66, Jan. 2019.

[55] A. Bahramian and G. Ahmadi, "Effect of sneeze flow velocity profiles on the respiratory droplets dispersion in a confined space: An experimental and computational fluid dynamics study," *Physics of Fluids*, vol. 35, p. 063330, June 2023.

[56] S. Coldrick, A. Kelsey, M. J. Ivings, T. G. Foat, S. T. Parker, C. J. Noakes, A. Bennett, H. Rickard, and G. Moore, "Modeling and experimental study of dispersion and deposition of respiratory emissions with implications for disease transmission," *Indoor Air*, vol. 32, Feb. 2022.

[57] J. Tang, C. Noakes, P. Nielsen, I. Eames, A. Nicolle, Y. Li, and G. Settles, "Observing and quantifying airflows in the infection control of aerosol- and airborne-transmitted diseases: An overview of approaches," *Journal of Hospital Infection*, vol. 77, pp. 213–222, Mar. 2011.

[58] D. Rim and A. Novoselac, "Ventilation effectiveness as an indicator of occupant exposure to particles from indoor sources," *Building and Environment*, vol. 45, pp. 1214–1224, May 2010.

[59] C. C. Ooi, A. Suwardi, Z. L. Ou Yang, G. Xu, C. K. I. Tan, D. Daniel, H. Li, Z. Ge, F. Y. Leong, K. Marimuthu, O. T. Ng, S. B. Lim, P. Lim, W. S. Mak, W. C. D. Cheong, X. J. Loh, C. W. Kang, and K. H. Lim, "Risk assessment of airborne covid-19 exposure in social settings," *Physics of Fluids*, vol. 33, p. 087118, Aug. 2021.

[60] H. Wang, Z. Li, Y. Liu, L. Zhu, and Z. Zhou, "Experimental study of the dispersion of cough-generated droplets from a person going up- or downstairs," *AIP Advances*, vol. 12, p. 015002, Jan. 2022.

[61] Z. Zhang, T. Han, K. H. Yoo, J. Capecelatro, and K. Maki, "Disease transmission through expiratory aerosols on an urban bus," *Physics of Fluids*, vol. 33, no. 1, p. 015116, 2021.

[62] S. Burgmann and U. Janoske, "Transmission and reduction of aerosols in classrooms using air purifier systems," *Physics of Fluids*, vol. 33, p. 033321, Mar. 2021.

[63] X. Zhuang, Y. Xu, L. Zhang, X. Li, and J. Lu, "Experiment and numerical investigation of inhalable particles and indoor environment with ventilation system," *Energy and Buildings*, vol. 271, p. 112309, Sept. 2022.

[64] Y. Zhou and S. Ji, "Experimental and numerical study on the transport of droplet aerosols generated by occupants in a fever clinic," *Building and Environment*, vol. 187, p. 107402, Jan. 2021.

[65] S. Liu, M. Koupriyanov, D. Paskaruk, G. Fediuk, and Q. Chen, "Investigation of airborne particle exposure in an office with mixing and displacement ventilation," *Sustainable Cities and Society*, vol. 79, p. 103718, Apr. 2022.

[66] H. Li, Y. Lan, M. Liu, X. Kong, and M. Fan, "Experimental research on the cross-infection control performance of different ventilation strategies," *Building and Environment*, vol. 243, p. 110683, Sept. 2023.

[67] J. Xu, H. Guo, Y. Zhang, and X. Lyu, "Effectiveness of personalized air curtain in reducing exposure to airborne cough droplets," *Building and Environment*, vol. 208, p. 108586, Jan. 2022.

[68] Y. Wang, Z. Liu, H. Liu, M. Wu, J. He, and G. Cao, "Droplet aerosols transportation and deposition for three respiratory behaviors in a typical negative pressure isolation ward," *Building and Environment*, vol. 219, p. 109247, July 2022.

[69] K.-C. Chung and S.-P. Hsu, "Effect of ventilation pattern on room air and contaminant distribution," *Building and Environment*, p. 10, 2001.

[70] C. Gilkeson, M. Camargo-Valero, L. Pickin, and C. Noakes, "Measurement of ventilation and airborne infection risk in large naturally ventilated hospital wards," *Building and Environment*, vol. 65, pp. 35–48, July 2013.

[71] G. Cao, K. Sirén, and S. Kilpeläinen, "Modelling and experimental study of performance of the protected occupied zone ventilation," *Energy and Buildings*, vol. 68, pp. 515–531, Jan. 2014.

[72] E. Bjørn and P. V. Nielsen, "Dispersal of exhaled air and personal exposure in displacement ventilated rooms," *Indoor Air*, vol. 12, pp. 147–164, Sept. 2002.

[73] H. Qian, Y. Li, P. V. Nielsen, C. E. Hyldgaard, T. W. Wong, and A. T. Y. Chwang, "Dispersion of exhaled droplet nuclei in a two-bed hospital ward with three different ventilation systems," *Indoor Air*, vol. 16, pp. 111–128, Apr. 2006.

[74] I. Olmedo, P. V. Nielsen, M. Ruiz de Adana, R. L. Jensen, and P. Grzelecki, "Distribution of exhaled contaminants and personal exposure in a room using three different air distribution strategies: Distribution of exhaled contaminants," *Indoor Air*, vol. 22, pp. 64–76, Feb. 2012.

[75] J. Yang, S. C. Sekhar, K. W. D. Cheong, and B. Raphael, "Performance evaluation of a novel personalized ventilation-personalized exhaust system for airborne infection control," *Indoor Air*, vol. 25, pp. 176–187, Apr. 2015.

[76] K. W. D. Cheong and S. Y. Phua, "Development of ventilation design strategy for effective removal of pollutant in the isolation room of a hospital," *Building and Environment*, vol. 41, pp. 1161–1170, Sept. 2006.

[77] Y.-C. Tung, Y.-C. Shih, S.-C. Hu, and Y.-L. Chang, "Experimental performance investigation of ventilation schemes in a private bathroom," *Building and Environment*, vol. 45, pp. 243–251, Jan. 2010.

[78] Y. Lu, M. Oladokun, and Z. Lin, "Reducing the exposure risk in hospital wards by applying stratum ventilation system," *Building and Environment*, vol. 183, p. 107204, Oct. 2020.

[79] Z. Ai, C. M. Mak, N. Gao, and J. Niu, "Tracer gas is a suitable surrogate of exhaled droplet nuclei for studying airborne transmission in the built environment," *Building Simulation*, vol. 13, pp. 489–496, June 2020.

[80] M. Bivolarova, J. Ondráček, A. Melikov, and V. Ždímal, "A comparison between tracer gas and aerosol particles distribution indoors: The impact of ventilation rate, interaction of airflows, and presence of objects," *Indoor Air*, vol. 27, pp. 1201–1212, Nov. 2017.

[81] E. Rivas, J. L. Santiago, F. Martín, and A. Martilli, "Impact of natural ventilation on exposure to sars-cov 2 in indoor/semi-indoor terraces using co2 concentrations as a proxy," *Journal of Building Engineering*, vol. 46, p. 103725, Apr. 2022.

[82] Z. Zhang, X. Chen, S. Mazumdar, T. Zhang, and Q. Chen, "Experimental and numerical investigation of airflow and contaminant transport in an airliner cabin mockup," *Building and Environment*, vol. 44, pp. 85–94, Jan. 2009.

[83] Q. He, J. Niu, N. Gao, T. Zhu, and J. Wu, "Cfd study of exhaled droplet transmission between occupants under different ventilation strategies in a typical office room," *Building and Environment*, vol. 46, pp. 397–408, Feb. 2011.

[84] X. Li, J. Niu, and N. Gao, "Spatial distribution of human respiratory droplet residuals and exposure risk for the co-occupant under different ventilation methods," *HVAC&R Research*, vol. 17, no. 4, pp. 432–445, 2011.

[85] X. Li, J. Niu, and N. Gao, "Co-occupant's exposure to exhaled pollutants with two types of personalized ventilation strategies under mixing and displacement ventilation systems," *Indoor Air*, vol. 23, no. 2, pp. 162–171, 2013.

[86] D. Rim and A. Novoselac, "Transport of particulate and gaseous pollutants in the vicinity of a human body," *Building and Environment*, vol. 44, pp. 1840–1849, Sept. 2009.

[87] X. Tian, B. Li, Y. Ma, D. Liu, Y. Li, and Y. Cheng, "Experimental study of local thermal comfort and ventilation performance for mixing, displacement and stratum ventilation in an office," *Sustainable Cities and Society*, vol. 50, p. 101630, Oct. 2019.

[88] A. Ameen, M. Cehlin, U. Larsson, and T. Karimipanah, "Experimental investigation of the ventilation performance of different air distribution systems in an office environment—cooling mode," *Energies*, vol. 12, p. 1354, Apr. 2019.

[89] X. Kong, Y. Chang, M. Fan, and H. Li, "Analysis on the thermal performance of low-temperature radiant floor coupled with intermittent stratum ventilation (ltr-isv) for space heating," *Energy and Buildings*, vol. 278, p. 112623, Jan. 2023.

[90] X. Kong, Z. Wang, M. Fan, and H. Li, "Analysis on the energy efficiency, thermal performance and infection intervention characteristics of interactive cascade ventilation (icv)," *Journal of Building Engineering*, vol. 68, p. 106045, June 2023.

[91] H. Na, H. Kim, and T. Kim, "Dispersion of droplets due to the use of air purifiers during summer: Focus on the spread of covid-19," *Building and Environment*, vol. 234, p. 110136, Apr. 2023.

[92] J. Capecelatro and O. Desjardins, "An euler–lagrange strategy for simulating particle-laden flows," *Journal of Computational Physics*, vol. 238, pp. 1–31, Apr. 2013.

[93] M. E. Rosti, S. Olivieri, M. Cavaiola, A. Seminara, and A. Mazzino, "Fluid dynamics of covid-19 airborne infection suggests urgent data for a scientific design of social distancing," *Scientific Reports*, vol. 10, p. 22426, Dec. 2020.

[94] J. Wang, F. Dalla Barba, and F. Picano, "Direct numerical simulation of an evaporating turbulent diluted jet-spray at moderate reynolds number," *International Journal of Multiphase Flow*, vol. 137, p. 103567, Apr. 2021.

[95] K. L. Chong, C. S. Ng, N. Hori, R. Yang, R. Verzicco, and D. Lohse, "Extended lifetime of respiratory droplets in a turbulent vapor puff and its implications on airborne disease transmission," *Physical Review Letters*, vol. 126, p. 034502, Jan. 2021.

[96] M. E. Rosti, M. Cavaiola, S. Olivieri, A. Seminara, and A. Mazzino, "Turbulence role in the fate of virus-containing droplets in violent expiratory events," *Physical Review Research*, vol. 3, p. 013091, Jan. 2021.

[97] A. Fabregat, F. Gisbert, A. Vernet, S. Dutta, K. Mittal, and J. Pallarès, "Direct numerical simulation of the turbulent flow generated during a violent expiratory event," *Physics of Fluids*, vol. 33, p. 035122, Mar. 2021.

[98] A. Fabregat, F. Gisbert, A. Vernet, J. A. Ferré, K. Mittal, S. Dutta, and J. Pallarès, "Direct numerical simulation of turbulent dispersion of evaporative aerosol clouds produced by an intense expiratory event," *Physics of Fluids*, vol. 33, p. 033329, Mar. 2021.

[99] N. Sen, "Transmission and evaporation of cough droplets in an elevator: Numerical simulations of some possible scenarios," *Physics of Fluids*, vol. 33, p. 033311, Mar. 2021.

[100] K. Talaat, M. Abuhegazy, O. A. Mahfoze, O. Anderoglu, and S. V. Poroseva, "Simulation of aerosol transmission on a boeing 737 airplane with intervention measures for covid-19 mitigation," *Physics of Fluids*, vol. 33, p. 033312, Mar. 2021.

[101] F. Arpino, G. Grossi, G. Cortellessa, A. Mikszewski, L. Morawska, G. Buonanno, and L. Stabile, "Risk of sars-cov-2 in a car cabin assessed through 3d cfd simulations," *Indoor Air*, vol. 32, Mar. 2022.

[102] F. Arpino, G. Cortellessa, G. Grossi, and H. Nagano, "A eulerian-lagrangian approach for the non-isothermal and transient cfd analysis of the aerosol airborne dispersion in a car cabin," *Building and Environment*, vol. 209, p. 108648, Feb. 2022.

[103] R. He, W. Liu, J. Elson, R. Vogt, C. Maranville, and J. Hong, "Airborne transmission of covid-19 and mitigation using box fan air cleaners in a poorly ventilated classroom," *Physics of Fluids*, vol. 33, p. 057107, May 2021.

[104] H. Liu, S. He, L. Shen, and J. Hong, "Simulation-based study of covid-19 outbreak associated with air-conditioning in a restaurant," *Physics of Fluids*, vol. 33, p. 023301, Feb. 2021.

[105] Y. Yang, Y. Wang, C. Su, X. Liu, X. Yuan, and Z. Chen, "Numerical investigation on the droplet dispersion inside a bus and the infection risk prediction," *Applied Sciences*, vol. 12, p. 5909, June 2022.

[106] L. Huang, S. Riyadi, I. Utama, M. Li, P. Sun, and G. Thomas, "Covid-19 transmission inside a small passenger vessel: Risks and mitigation," *Ocean Engineering*, vol. 255, p. 111486, July 2022.

[107] T. Dbouk and D. Drikakis, "On coughing and airborne droplet transmission to humans," *Physics of Fluids*, vol. 32, p. 053310, May 2020.

[108] Y.-y. Li, J.-X. Wang, and X. Chen, "Can a toilet promote virus transmission? from a fluid dynamics perspective," *Physics of Fluids*, vol. 32, p. 065107, June 2020.

[109] Y. Feng, "Influence of wind and relative humidity on the social distancing effectiveness to prevent covid-19 airborne transmission: A numerical study," *Journal of Aerosol Science*, p. 19, 2020.

[110] Z. Li, X. Zhang, T. Wu, L. Zhu, J. Qin, and X. Yang, "Effects of slope and speed of escalator on the dispersion of cough-generated droplets from a passenger," *Physics of Fluids*, vol. 33, p. 041701, Apr. 2021.

[111] K. Zhong, X. Yang, and Y. Kang, "Effects of ventilation strategies and source locations on indoor particle deposition," *Building and Environment*, vol. 45, pp. 655–662, Mar. 2010.

[112] A. Makhoul, K. Ghali, N. Ghaddar, and W. Chakroun, "Investigation of particle transport in offices equipped with ceiling-mounted personalized ventilators," *Building and Environment*, vol. 63, pp. 97–107, May 2013.

[113] T. Li, E. A. Essah, Y. Wu, Y. Cheng, and C. Liao, "Numerical comparison of exhaled particle dispersion under different air distributions for winter heating," *Sustainable Cities and Society*, vol. 89, p. 104342, Feb. 2023.

[114] S. Xu, G. Zhang, X. Liu, and X. Li, "Cfd modelling of infection control in indoor environments: A focus on room-level air recirculation systems," *Energy and Buildings*, vol. 288, p. 113033, June 2023.

[115] L. Wang, X. Dai, J. Wei, Z. Ai, Y. Fan, L. Tang, T. Jin, and J. Ge, "Numerical comparison of the efficiency of mixing ventilation and impinging jet ventilation for exhaled particle removal in a model intensive care unit," *Building and Environment*, vol. 200, p. 107955, Aug. 2021.

[116] J. Ren, Y. Wang, Q. Liu, and Y. Liu, "Numerical study of three ventilation strategies in a prefabricated covid-19 inpatient ward," *Building and Environment*, vol. 188, p. 107467, Jan. 2021.

[117] H. Motamedi, M. Shirzadi, Y. Tominaga, and P. A. Mirzaei, "Cfd modeling of airborne pathogen transmission of covid-19 in confined spaces under different ventilation strategies," *Sustainable Cities and Society*, vol. 76, p. 103397, Jan. 2022.

[118] S. Liu and Z. Deng, "Transmission and infection risk of covid-19 when people coughing in an elevator," *Building and Environment*, vol. 238, p. 110343, June 2023.

[119] L. Borro, L. Mazzei, M. Raponi, P. Piscitelli, A. Miani, and A. Secinaro, "The role of air conditioning in the diffusion of sars-cov-2 in indoor environments: A first computational fluid dynamic model, based on investigations performed at the vatican state children's hospital," *Environmental Research*, vol. 193, p. 110343, Feb. 2021.

[120] X. Li and B. Feng, "Transmission of droplet aerosols in an elevator cabin: Effect of the ventilation mode," *Building and Environment*, vol. 236, p. 110261, May 2023.

[121] Y. Lu and Z. Lin, "Coughed droplet dispersion pattern in hospital ward under stratum ventilation," *Building and Environment*, vol. 208, p. 108602, Jan. 2022.

[122] Y. Zhang, G. Feng, Y. Bi, Y. Cai, Z. Zhang, and G. Cao, "Distribution of droplet aerosols generated by mouth coughing and nose breathing in an air-conditioned room," *Sustainable Cities and Society*, vol. 51, p. 101721, Nov. 2019.

[123] X. Li, Y. Yan, Y. Shang, and J. Tu, "An eulerian–eulerian model for particulate matter transport in indoor spaces," *Building and Environment*, vol. 86, pp. 191–202, Apr. 2015.

[124] R. Garg, C. Narayanan, and S. Subramaniam, "A numerically convergent lagrangian–eulerian simulation method for dispersed two-phase flows," *International Journal of Multiphase Flow*, vol. 35, pp. 376–388, Apr. 2009.

[125] H. Salman and M. Soteriou, "Lagrangian simulation of evaporating droplet sprays," *Physics of Fluids*, vol. 16, pp. 4601–4622, Dec. 2004.

[126] S. Bensaid, D. Marchisio, D. Fino, G. Saracco, and V. Specchia, "Modelling of diesel particulate filtration in wall-flow traps," *Chemical Engineering Journal*, vol. 154, pp. 211–218, Nov. 2009.

[127] F. Wang, T. T. Zhang, R. You, and Q. Chen, "Evaluation of infection probability of covid-19 in different types of airliner cabins," *Building and Environment*, vol. 234, p. 110159, Apr. 2023.

[128] S. Park, R. Mistrick, and D. Rim, "Performance of upper-room ultraviolet germicidal irradiation (uvgi) system in learning environments: Effects of ventilation rate, uv fluence rate, and uv radiating volume," *Sustainable Cities and Society*, vol. 85, p. 104048, Oct. 2022.

[129] Z. Zhang and Q. Chen, "Comparison of the eulerian and lagrangian methods for predicting particle transport in enclosed spaces," *Atmospheric Environment*, vol. 41, pp. 5236–5248, Aug. 2007.

[130] X. Shao, X. Wen, R. Paek, Y. Liu, Y. Jian, and W. Liu, "Use of recirculated air curtains inside ventilated rooms for the isolation of transient contaminant," *Energy and Buildings*, vol. 273, p. 112407, Oct. 2022.

[131] C. Ren, C. Xi, J. Wang, Z. Feng, F. Nasiri, S.-J. Cao, and F. Haghighat, "Mitigating covid-19 infection disease transmission in indoor environment using physical barriers," *Sustainable Cities and Society*, vol. 74, p. 103175, Nov. 2021.

[132] A. C. D'Alicandro and A. Mauro, "Effects of operating room layout and ventilation system on ultrafine particle transport and deposition," *Atmospheric Environment*, vol. 270, p. 118901, Feb. 2022.

[133] E. Belut, S. Lechêne, B. Trouette, S. Vincent, and G. Halim Atallah, "Flow and contaminant transfer at the interface of an aerodynamic containment barrier subjected to the wake of a moving obstacle," *Building and Environment*, p. 110465, May 2023.

[134] C. Ren, H.-C. Zhu, and S.-J. Cao, "Ventilation strategies for mitigation of infection disease transmission in an indoor environment: A case study in office," *Buildings*, vol. 12, p. 180, Feb. 2022.

[135] Z. Wang, E. R. Galea, A. Grandison, J. Ewer, and F. Jia, "A coupled computational fluid dynamics and wells-riley model to predict covid-19 infection probability for passengers on long-distance trains," *Safety Science*, vol. 147, p. 105572, Mar. 2022.

[136] I. H. Hatif, H. Mohamed Kamar, N. Kamsah, K. Y. Wong, and H. Tan, "Influence of office furniture on exposure risk to respiratory infection under mixing and displacement air distribution systems," *Building and Environment*, vol. 239, p. 110292, July 2023.

[137] F. Chen, S. C. Yu, and A. C. Lai, "Modeling particle distribution and deposition in indoor environments with a new drift–flux model," *Atmospheric Environment*, vol. 40, pp. 357–367, Jan. 2006.

[138] B. Zhao, C. Yang, X. Yang, and S. Liu, "Particle dispersion and deposition in ventilated rooms: Testing and evaluation of different eulerian and lagrangian models," *Building and Environment*, vol. 43, pp. 388–397, Apr. 2008.

[139] B. Zhao, C. Chen, and Z. Tan, "Modeling of ultrafine particle dispersion in indoor environments with an improved drift flux model," *Journal of Aerosol Science*, vol. 40, pp. 29–43, Jan. 2009.

[140] Z. Lin, J. Wang, T. Yao, and T. Chow, "Investigation into anti-airborne infection performance of stratum ventilation," *Building and Environment*, vol. 54, pp. 29–38, Aug. 2012.

[141] A. C. D'Alicandro and A. Mauro, "Air change per hour and inlet area: Effects on ultrafine particle concentration and thermal comfort in an operating room," *Journal of Aerosol Science*, vol. 171, p. 106183, June 2023.

[142] S. S. Diwan, S. Ravichandran, R. Govindarajan, and R. Narasimha, "Understanding transmission dynamics of covid-19-type infections by direct numerical simulations of cough/sneeze flows," *Transactions of the Indian National Academy of Engineering*, vol. 5, pp. 255–261, June 2020.

[143] R. Singhal, S. Ravichandran, and S. S. Diwan, "Direct numerical simulation of a moist cough flow using eulerian approximation for liquid droplets," *International Journal of Computational Fluid Dynamics*, vol. 35, pp. 778–797, Oct. 2021.

[144] R. Singhal, S. Ravichandran, R. Govindarajan, and S. S. Diwan, "Virus transmission by aerosol transport during short conversations," *Flow*, vol. 2, p. E13, 2022.

[145] Y. Yan, X. Li, and K. Ito, "Numerical investigation of indoor particulate contaminant transport using the eulerian-eulerian and eulerian-lagrangian two-phase flow models," *Experimental and Computational Multiphase Flow*, vol. 2, pp. 31–40, Mar. 2020.

[146] G. Pei, M. Taylor, and D. Rim, "Human exposure to respiratory aerosols in a ventilated room: Effects of ventilation condition, emission mode, and social distancing," *Sustainable Cities and Society*, vol. 73, p. 103090, Oct. 2021.

[147] D. L. Marchisio and R. O. Fox, *Computational Models for Polydisperse Particulate and Multiphase Systems*. Cambridge Series in Chemical Engineering, Cambridge: Cambridge University Press, 2013.

[148] R. Lehnigk, W. Bainbridge, Y. Liao, D. Lucas, T. Niemi, J. Peltola, and F. Schlegel, "An open-source population balance modeling framework for the simulation of polydisperse multiphase flows," *AIChE Journal*, vol. 68, Mar. 2022.

[149] J. Heylmun, B. Kong, A. Passalacqua, and R. Fox, "A quadrature-based moment method for polydisperse bubbly flows," *Computer Physics Communications*, vol. 244, pp. 187–204, Nov. 2019.

[150] C. T. Crowe, J. D. Schwarzkopf, M. Sommerfeld, and Y. Tsuji, *Multiphase Flows with Droplets and Particles*. Boca Raton: CRC Press, 2nd ed., 2012.

[151] C. Chen and B. Zhao, "Some questions on dispersion of human exhaled droplets in ventilation room: Answers from numerical investigation," *Indoor Air*, vol. 20, pp. 95–111, Apr. 2010.

[152] L. Zhang and Y. Li, "Dispersion of coughed droplets in a fully-occupied high-speed rail cabin," *Building and Environment*, vol. 47, pp. 58–66, Jan. 2012.

[153] B. Zhao, Y. Zhang, X. Li, X. Yang, and D. Huang, "Comparison of indoor aerosol particle concentration and deposition in different ventilated rooms by numerical method," *Building and Environment*, vol. 39, pp. 1–8, Jan. 2004.

[154] A. Li and G. Ahmadi, "Dispersion and Deposition of Spherical Particles from Point Sources in a Turbulent Channel Flow," *Aerosol Science and Technology*, vol. 16, pp. 209–226, Jan. 1992.

[155] X. Yang, C. Ou, H. Yang, L. Liu, T. Song, M. Kang, H. Lin, and J. Hang, "Transmission of pathogen-laden expiratory droplets in a coach bus," *Journal of Hazardous Materials*, vol. 397, p. 122609, Oct. 2020.

[156] L. Schiller and A. Naumann, "A drag coefficient correlation," *Zeitschrift des Vereins deutscher Ingenieure*, vol. 77, no. 12, pp. 318–320, 1933.

[157] N. Frössling, "On the vaporization of a falling drop," *Gerlands Beiträge zur Geophysik*, vol. 52, pp. 170–216, 1938.

[158] O. C. Bridgeman and E. W. Aldrich, "Vapor pressure tables for water," *Journal of Heat Transfer*, vol. 86, pp. 279–286, May 1964.

[159] W. Ranz and W. Marshall, "Evaporation from drops. part i," *Chemical Engineering Progress*, vol. 48, pp. 141–146, 1952.

[160] W. Ranz and W. Marshall, "Evaporation from drops. part ii," *Chemical Engineering Progress*, vol. 48, pp. 173–180, 1952.

[161] A. Kumar and S. Hartland, "Correlations for prediction of mass transfer coefficients in single drop systems and liquid–liquid extraction columns," *Chemical Engineering Research and Design*, vol. 77, pp. 372–384, July 1999.

[162] OpenFOAM-Foundation, "Openfoam 8 released." https://openfoam.org/release/8/, July 2020.

[163] V. Yakhot, S. A. Orszag, S. Thangam, T. B. Gatski, and C. G. Speziale, "Development of turbulence models for shear flows by a double expansion technique," *Physics of Fluids A: Fluid Dynamics*, vol. 4, pp. 1510–1520, July 1992.

[164] Q. Chen, "Comparison of different k -ε models for indoor air flow computations," *Numerical Heat Transfer, Part B: Fundamentals*, vol. 28, pp. 353–369, Oct. 1995.

[165] N. Gao and J. Niu, "Transient cfd simulation of the respiration process and inter-person exposure assessment," *Building and Environment*, vol. 41, pp. 1214–1222, Sept. 2006.

[166] B. E. Yuce and E. Pulat, "Forced, natural and mixed convection benchmark studies for indoor thermal environments," *International Communications in Heat and Mass Transfer*, vol. 92, pp. 1–14, Mar. 2018.

[167] N. Serra, "Revisiting rans turbulence modelling used in built-environment cfd simulations," *Building and Environment*, vol. 237, p. 110333, June 2023.

[168] T. Wang, O. Han, A. Li, H. Yin, J. Li, Y. Ma, and Y. Hou, "Study on the air distribution characteristics of equipartition-ring column attachment ventilation mode," *Building and Environment*, vol. 234, p. 110179, Apr. 2023.

[169] A. C. D'Alicandro and A. Mauro, "Experimental and numerical analysis of CO_2 transport inside a university classroom: Effects of turbulent models," *Journal of Building Performance Simulation*, vol. 16, pp. 434–459, July 2023.

[170] L. Anghel, C.-G. Popovici, C. Stătescu, R. Sascău, M. Verdeș, V. Ciocan, I.-L. Șerban, M. A. Mărănducă, S.-V. Hudișteanu, and F.-E. Țurcanu, "Impact of hvac-systems on the dispersion of infectious aerosols in a cardiac intensive care unit," *International Journal of Environmental Research and Public Health*, vol. 17, p. 6582, Sept. 2020.

[171] J. Posner, C. Buchanan, and D. Dunn-Rankin, "Measurement and prediction of indoor air flow in a model room," *Energy and Buildings*, vol. 35, pp. 515–526, June 2003.

[172] P. V. Nielsen, "Fifty years of cfd for room air distribution," *Building and Environment*, vol. 91, pp. 78–90, Sept. 2015.

[173] J. Wang, M. Alipour, G. Soligo, A. Roccon, M. De Paoli, F. Picano, and A. Soldati, "Short-range exposure to airborne virus transmission and current guidelines," *Proceedings of the National Academy of Sciences*, vol. 118, p. e2105279118, Sept. 2021.

[174] S. Elghobashi, "On predicting particle-laden turbulent flows," *Applied Scientific Research*, vol. 52, pp. 309–329, June 1994.

[175] H. Zhang, F. Wang, Y. Wang, and H. Wang, "Cfd simulation of cooking particle distribution and motion," *Procedia Engineering*, vol. 205, pp. 1800–1806, 2017.

[176] E. Krepper, D. Lucas, T. Frank, H.-M. Prasser, and P. J. Zwart, "The inhomogeneous musig model for the simulation of polydispersed flows," *Nuclear Engineering and Design*, vol. 238, pp. 1690–1702, July 2008.

[177] J. C. Wheeler, "Modified moments and gaussian quadratures," *Rocky Mountain Journal of Mathematics*, vol. 4, June 1974.

[178] C. Yuan and R. Fox, "Conditional quadrature method of moments for kinetic equations," *Journal of Computational Physics*, vol. 230, pp. 8216–8246, Sept. 2011.

[179] C. Yuan, F. Laurent, and R. Fox, "An extended quadrature method of moments for population balance equations," *Journal of Aerosol Science*, vol. 51, pp. 1–23, Sept. 2012.

[180] ESI-OpenCFD, "Esi opencfd release openfoam® v2106." https://www.openfoam.com/news/main-news/openfoam-v2106, June 2021.

[181] A. Passalacqua, J. Heylmun, M. Icardi, E. Madadi, P. Bachant, X. Hu, and J. Weaver, "Openqbmm/openqbmm: Openqbmm 7.0.0 for openfoam v2106." Zenodo, June 2021.

[182] M. Shiea, A. Buffo, M. Vanni, and D. L. Marchisio, "A novel finite-volume tvd scheme to overcome non-realizability problem in quadrature-based moment methods," *Journal of Computational Physics*, vol. 409, p. 109337, May 2020.

[183] A. Passalacqua and R. Fox, "Implementation of an iterative solution procedure for multi-fluid gas–particle flow models on unstructured grids," *Powder Technology*, vol. 213, pp. 174–187, Nov. 2011.

[184] J. Cheng, Q. Li, C. Yang, Y. Zhang, and Z. Mao, "Cfd-pbe simulation of a bubble column in openfoam," *Chinese Journal of Chemical Engineering*, vol. 26, pp. 1773–1784, Sept. 2018.

[185] P. K. Sweby, "High resolution schemes using flux limiters for hyperbolic conservation laws," *SIAM Journal on Numerical Analysis*, vol. 21, pp. 995–1011, Oct. 1984.

[186] S. Chaudhuri, S. Basu, P. Kabi, V. R. Unni, and A. Saha, "Modeling the role of respiratory droplets in covid-19 type pandemics," *Physics of Fluids*, vol. 32, p. 063309, June 2020.

[187] F. Dalla Barba, J. Wang, and F. Picano, "Revisiting d 2-law for the evaporation of dilute droplets," *Physics of Fluids*, vol. 33, p. 051701, May 2021.

[188] S. Basu, P. Kabi, S. Chaudhuri, and A. Saha, "Insights on drying and precipitation dynamics of respiratory droplets from the perspective of covid-19," *Physics of Fluids*, vol. 32, p. 123317, Dec. 2020.

[189] M. Stiti, G. Castanet, A. Corber, M. Alden, and E. Berrocal, "Transition from saliva droplets to solid aerosols in the context of covid-19 spreading," *Environmental Research*, vol. 204, p. 112072, Mar. 2022.

[190] C. Lieber, S. Melekidis, R. Koch, and H.-J. Bauer, "Insights into the evaporation characteristics of saliva droplets and aerosols: Levitation experiments and numerical modeling," *Journal of Aerosol Science*, vol. 154, p. 105760, May 2021.

[191] G. Faeth, "Current status of droplet and liquid combustion," in *Energy and Combustion Science*, pp. 149–182, Elsevier, 1979.

[192] J. Redrow, S. Mao, I. Celik, J. A. Posada, and Z.-g. Feng, "Modeling the evaporation and dispersion of airborne sputum droplets expelled from a human cough," *Building and Environment*, vol. 46, pp. 2042–2051, Oct. 2011.

[193] J. Wei and Y. Li, "Enhanced spread of expiratory droplets by turbulence in a cough jet," *Building and Environment*, vol. 93, pp. 86–96, Nov. 2015.

[194] H. Li, F. Y. Leong, G. Xu, Z. Ge, C. W. Kang, and K. H. Lim, "Dispersion of evaporating cough droplets in tropical outdoor environment," *Physics of Fluids*, vol. 32, p. 113301, Nov. 2020.

[195] Y. Yan, X. Li, and J. Tu, "Thermal effect of human body on cough droplets evaporation and dispersion in an enclosed space," *Building and Environment*, vol. 148, pp. 96–106, Jan. 2019.

[196] D. Mirikar, S. Palanivel, and V. Arumuru, "Droplet fate, efficacy of face mask, and transmission of virus-laden droplets inside a conference room," *Physics of Fluids*, vol. 33, p. 065108, June 2021.

[197] Y. Yan, X. Fang, X. Li, Y. Tao, P. Yan, and J. Tu, "Evaporation flow characteristics of respiratory droplets: Dynamic property under multifarious ambient conditions," *Building and Environment*, vol. 221, p. 109272, Aug. 2022.

[198] T. T. Zhang, K. Lee, and Q. Y. Chen, "A simplified approach to describe complex diffusers in displacement ventilation for cfd simulations," *Indoor Air*, vol. 19, pp. 255–267, June 2009.

[199] M.-F. King, C. J. Noakes, and P. A. Sleigh, "Modeling environmental contamination in hospital single- and four-bed rooms," *Indoor Air*, vol. 25, pp. 694–707, Dec. 2015.

[200] D. T. Pritchard and J. A. Currie, "Diffusion of coefficients of carbon dioxide, nitrous oxide, ethylene and ethane in air and their measurement," *Journal of Soil Science*, vol. 33, pp. 175–184, June 1982.

[201] W. Massman, "A review of the molecular diffusivities of h2o, co2, ch4, co, o3, so2, nh3, n2o, no, and no2 in air, o2 and n2 near stp," *Atmospheric Environment*, vol. 32, pp. 1111–1127, Mar. 1998.

[202] Y. Cheng and Z. Lin, "Experimental study of airflow characteristics of stratum ventilation in a multi-occupant room with comparison to mixing ventilation and displacement ventilation," *Indoor Air*, vol. 25, pp. 662–671, Dec. 2015.

[203] Y. Feng, D. Li, D. Marchisio, M. Vanni, and A. Buffo, "A computational fluid dynamics—population balance equation approach for evaporating cough droplets transport," *International Journal of Multiphase Flow*, vol. 165, p. 104500, Apr. 2023.

[204] S. Balachandar and J. K. Eaton, "Turbulent dispersed multiphase flow," *Annual Review of Fluid Mechanics*, vol. 42, pp. 111–133, Jan. 2010.

Appendix A

Derivation of the diameter change rate

For a single droplet, the mass transfer rate $\dot{m} = \mathrm{d}m/\mathrm{d}t$ can be related to the diameter change rate $G_{\mathrm{d}} = \mathrm{d}d/\mathrm{d}t$ using the following equation:

$$\dot{m} = \frac{\mathrm{d}m}{\mathrm{d}t} = \frac{\mathrm{d}}{\mathrm{d}t}\left(\frac{\pi}{6}\rho_{\mathrm{d}}d^3\right) = \frac{\pi}{2}\rho_{\mathrm{d}}d^2\frac{\mathrm{d}d}{\mathrm{d}t} = \frac{\pi}{2}\rho_{\mathrm{d}}d^2 G_{\mathrm{d}}, \tag{A.1}$$

Therefore, the diameter change rate for the pth quadrature node, $G_{\mathrm{d},p}$, can be calculated as:

$$G_{\mathrm{d},p} = \frac{2}{\pi\rho_{\mathrm{d}}d_p^2}\dot{m}_{\mathrm{d},p}, \tag{A.2}$$

where d_p is the diameter of the pth quadrature node, $\dot{m}_{\mathrm{d},p}$ is the mass transfer rate for a single droplet represented by the pth quadrature node and can be obtained from the TFM.

For the QMOM mono-solver in Section 2.4.2, the Sauter mean diameter d_{d} representing the DSD is used to calculate the mass transfer rate per unit volume, $\dot{m}_{\mathrm{d}}$, using Eq. (2.18). Therefore, $\dot{m}_{\mathrm{d}}$ represents the overall evaporation of the droplets. In order to calculate $G_{\mathrm{d},p}$, $\dot{m}_{\mathrm{d}}$ must be reallocated to the quadrature nodes to obtain $\dot{m}_{\mathrm{d},p}$.

According to Eq. (2.18), the mass transfer rate of water per unit volume for the pth quadrature node, $\dot{m}_p$, can be written as:

$$\dot{m}_p = \rho_c k_{\mathrm{d},p}(Y_{\mathrm{f},\mathrm{d}} - Y_{\mathrm{H}_2\mathrm{O}}), \tag{A.3}$$

where $k_{d,p}$ is the volumetric mass transfer coefficient of the pth quadrature node and it can be written as:

$$k_{d,p} = \frac{6\alpha_{d,p}\mathrm{Sh}D_c}{d_p^2},$$ (A.4)

where $\alpha_{d,p} = \alpha_d w_p d_p^3 / M_3 = \pi w_p d_p^3 / 6$ is the volume fraction of the pth quadrature node, w_p is the number concentration (or weight) of the pth quadrature node, and d_p is the diameter (or abscissa) of the pth quadrature node.

Substituting Eq. (A.4) into Eq. (A.3), we have

$$\dot{m}_p = \pi w_p d_p \rho_c \mathrm{Sh}D_c(Y_{f,d} - Y_{H_2O}),$$ (A.5)

and

$$\dot{m}_d = \sum_p \dot{m}_p = \pi M_1 \rho_c \mathrm{Sh}D_c(Y_{f,d} - Y_{H_2O}),$$ (A.6)

Therefore,

$$\dot{m}_p = \frac{w_p d_p}{M_1}\dot{m}_d.$$ (A.7)

For a single droplet represented by the pth quadrature node, the mass transfer rate, $\dot{m}_{d,p}$, can be written as:

$$\dot{m}_{d,p} = \frac{\dot{m}_p}{w_p} = \frac{d_p}{M_1}\dot{m}_d,$$ (A.8)

Substituting Eq. (A.8) into Eq. (A.2), we have the diameter change rate, $G_{d,p}$:

$$G_{d,p} = \frac{2}{\pi\rho_d d_p M_1}\dot{m}_d,$$ (A.9)

which is Eq. (2.61) in Section 2.4.2.

For the QMOM poly-solver in Section 2.4.3, the quadrature node diameters, d_p, are used in the calculation of interfacial models. Therefore, $\dot{m}_p$ are obtained from the TFM by Eq. (A.3), and the diameter change rate can be calculated as:

$$G_{d,p} = \frac{2}{\pi\rho_d w_p d_p^2}\dot{m}_p,$$ (A.10)

which is Eq. (2.72) in Section 2.4.3.

Appendix B

Algorithm for PBE with a single velocity

Eq. (2.59) is solved by a time-splitting method as follows:

1. Use the initial M_3 and M_2 (at time t) to calculate the disperse phase diameter (Sauter mean diameter) d_d as in Eq. (2.62), with which update the interfacial models. Then, solve the TFM from t to $t + \Delta t$ to obtain the disperse phase velocity $\mathbf{U}_d$ and the interfacial mass transfer rate $\dot{m}$;

2. Use $\mathbf{U}_d$ obtained from TFM to integrate the moment equations containing only the advection part from t to $t + \Delta t$:

$$\frac{\partial M_k}{\partial t} + \nabla \cdot (\mathbf{U}_d M_k) = 0, \tag{B.1}$$

and update the quadrature, w_p and d_p;

3. Use $\dot{m}$ obtained from TFM to calculate $G_{d,p}$ and update the abscissas as:

$$d_p(t + \Delta t) = d_p(t) - \frac{2}{\rho_d \pi d_p M_1} \dot{m} \Delta t. \tag{B.2}$$

If $d_p(t + \Delta t) < d_{\min}$, let $d_p(t + \Delta t) = d_{\min}$ to limit the minimum diameter of the droplets and $k_c = 0$ to make $\dot{m}$ be consistent in TFM abd PBE. Finally, update the moments using the weights and the updated abscissas and return to step (1) for the next time step.

Appendix C

Algorithm for PBE with multiple velocities

Eq. (2.69) and Eq. (2.70) are also solved by a time-splitting method as in the work of Heylmun et al. [149]:

1. Use M_k and $\mathcal{U}_k$ to find w_p, d_p and $\mathbf{U}_p$. And calculate the relative velocity as $\mathbf{V}_p = \mathbf{U}_p - \mathbf{U}_d$;

2. Solve the relative transport equation to obtain M_k^* and $\mathcal{U}_k^*$ as:

$$\frac{\partial M_k}{\partial t} + \nabla \cdot \mathcal{V}_k = 0, \tag{C.1}$$

$$\frac{\partial \mathcal{U}_k}{\partial t} + \nabla \cdot \mathcal{P}_{k,r} = 0. \tag{C.2}$$

3. Use M_k^* and $\mathcal{U}_k^*$ to update the quadrature node volume fraction and diameter as $\alpha_{d,p} = (\alpha_d w_p d_p^3)/M_3$ and $d_{d,p} = d_p$. Then, solve the TFM to update the average disperse phase velocity $\mathbf{U}_d$ and the interfacial mass transfer rate of the pth node $\dot{m}_p$;

4. Correct the flux to make α_d consistent with $\frac{\pi}{6} M_3$ by solving the following equation of ψ

$$\frac{6\alpha_d/\pi - M_3^*}{\Delta t} + \nabla \cdot (M_3^* \mathbf{U}_d) + \nabla \cdot (M_3^* \nabla \psi) = 0, \tag{C.3}$$

then, the average velocity is corrected as $\mathbf{U}_d^* = \mathbf{U}_d + \nabla \psi$;

5. Use $\mathbf{U}_d^*$ to solve the average transport equation as

$$\frac{\partial M_k}{\partial t} + \nabla \cdot (M_k \mathbf{U}_d^*) = 0, \tag{C.4}$$

$$\frac{\partial \mathscr{U}_k}{\partial t} + \nabla \cdot (\mathbf{U}_d^* \otimes \mathscr{U}_k) = 0, \tag{C.5}$$

and updated w_p, d_p and $\mathbf{U}_p$;

6. Use $\dot{m}_p$ obtained from TFM to update the size abscissas d_p as

$$d_p(t + \Delta t) = d_p(t) - \frac{2}{\rho_d \pi w_p d_p^2} \dot{m}_p \Delta t, \tag{C.6}$$

If $d_p(t + \Delta t) < d_{\min}$, then let $d_p(t + \Delta t) = d_{\min}$ and $k_c = 0$. Update the velocity abscissas $\mathbf{U}_p$ by solving the following equations:

$$\alpha_{d,p} \rho_d \frac{\partial \mathbf{U}_p}{\partial t} = \alpha_{d,p} \rho_d \mathbf{g} + \mathbf{M}_{d,p} - \dot{m}_p \mathbf{U}_p, \tag{C.7}$$

where $\mathbf{M}_{d,p}$ is the forces acted on the pth node, such as drag force;

7. After updating $\mathbf{U}_p$, re-compute $\mathscr{U}_k$, and the mass averaged $\mathbf{U}_d$ as

$$\mathbf{U}_d = \frac{\sum_{p=0}^{N-1} \left(w_p d_p^3 \mathbf{U}_p \right)}{M_3}, \tag{C.8}$$

and return to step (1) with the updated M_k and $\mathscr{U}_k$ for the next time step.

Appendix D

Thermal physical properties

The thermal physical properties are of great importance in the simulation of droplet evaporation. For the present evaporation model, the following thermal physical variables are important: density, absolute enthalpy, sensible internal energy, heat capacity, dynamic viscosity, and conductivity. Fortunately, OpenFOAM provides numerous thermal physical property models that can provide accurate descriptions of the properties of the substances.

For the disperse phase, the pure water droplets, the constant thermal physical properties for pure substance are adopted as: the density $\rho_d = 1000$ kg m^{-3}, the heat capacity at constant volume $C_{v,d} = 4195$ J kg^{-1} K^{-1}, the chemical enthalpy $H_{c,d} = -1.5879 \times 10^7$ J kg^{-1}, the dynamic viscosity $\mu_d = 8.9266 \times 10^{-4}$ kg m^{-1} s^{-1} and the Prandtl number Pr $= 6.14$.

Then, the absolute enthalpy is

$$H_{a,d} = C_{v,d}(T_d - T^*) + H_{c,d} + p/\rho_d \tag{D.1}$$

where $T^* = 298.15$ K is the reference temperature; the sensible internal energy is $E_d = C_{v,d}(T_d - T^*)$; and the conductivity is $\kappa_d = C_{p,d}\mu_d/\text{Pr}$.

For the continuous phase, the thermal physical models for a two-component mixture (water vapor and air) are adopted. For each component, the absolute enthalpy and sensible internal energy are calculated by polynomials of temperature fitting

NIST-JANAF thermochemical tables as:

$$H_a = R\left(\frac{a_4}{5}T^5 + \frac{a_3}{4}T^4 + \frac{a_2}{3}T^3 + \frac{a_1}{2}T^2 + a_0 T + a_5\right), \qquad \text{(D.2)}$$

$$E = H_a - H_a^* - p/\rho_c, \qquad \text{(D.3)}$$

where R is the specific gas constant, a_i are the coefficients and listed in Table D.1, and $H_{a,}^*$ is the reference enthalpy equal to the absolute enthalpy at T^* (298.15 K). Consequently, C_p and C_v can be obtained as:

$$C_p = R\left(a_4 T^4 + a_3 T^3 + a_2 T^2 + a_1 T + a_0\right), \qquad \text{(D.4)}$$

$$C_v = C_p - R. \qquad \text{(D.5)}$$

The viscosity and conductivity are specified by Sutherland's law as:

$$\mu = \frac{A_s\sqrt{T}}{1 + T_s/T}, \qquad \text{(D.6)}$$

$$\kappa = \mu C_v(1.32 + 1.77 R/C_v), \qquad \text{(D.7)}$$

where $A_s = 1.458 \times 10^{-6}$ and $T_s = 110.4$ for both components.

Finally, the variable ϕ (i.e., E, H, μ, ...) for the mixture is calculated by the species mass fraction Y_i and variable ϕ_i as $\phi = \sum_i^2 Y_i \phi_i$. Additionally, the molar mass for air is $W_{air} = 28.96 \text{ kg kmol}^{-1}$, for water vapor is $M_{water} = 18.02 \text{ kg kmol}^{-1}$ and for the mixture is $\bar{M} = 1/(\sum_i^2 Y_i/M_i)$. The density of the mixture is calculated by the perfect gas equation.

Table D.1 Coefficients for thermal properties of water vapor and air.

Specie	Water vapor	Air
a_0	4.19864	3.09589
a_1	-2.0364×10^{-3}	1.22835×10^{-3}
a_2	6.52040×10^{-6}	-4.14267×10^{-7}
a_3	-5.48797×10^{-9}	6.56910×10^{-11}
a_4	1.77198×10^{-12}	-3.87021×10^{-15}
a_5	-3.02937×10^4	-9.83191×10^2

Appendix E

Grid consistency examination

E.1   Grid for three-dimensional chamber

For the three-dimensional chamber, the grid convergence was examined using three grids having 364640 (coarse), 831220 (middle), and 1912700 (fine) cube cells, respectively. At each step, the grid was refined in the three directions with a factor of approximately 1.3, so the total factor is about 2.3. The case of sneeze jet front evolution in Section 3.3 was adopted for the grid convergence examination.

The results are shown in Figure E.1. It can be seen that differences in the results of the three grids were small. However, the result of the coarse grid showed a step-function-like behavior after $t = 0.6$ s. For example, the moving distance of the jet front kept 1.28 m from 0.9 s to 1.0 s and then increased to 1.33 m and kept constant from 1.05 s to 1.15 s. This was because, after $t = 0.6$ s, the velocity of the exhaled jet (or puff) was low. The coarse grid made it difficult to capture the slow movement. However, the middle grid and the fine grid, showing a continuous increment, can better capture such a slow movement. Considering the computational costs and accuracy, the middle grid of 831220 cells was adopted for the simulations in this study.
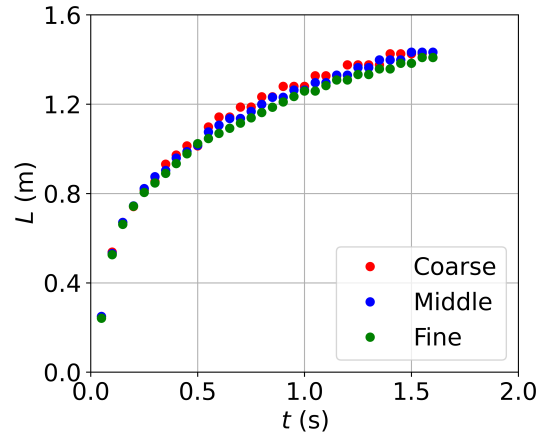
Fig. E.1 The results of grid convergence examination for the three-dimensional chamber.

E.2   The office with DV, SV and MV

For the small office equipped with DV, MV, and SV [87], the grid convergence was examined using three grids having 258232 (coarse), 553632 (medium), and 1222930 (fine) cube cells, respectively. The setup of MV was adopted as a test case and the results at the sampling line 4 of Figure 4.1b were shown in Figure E.2. It can be seen that the results of the medium grid and the fine grid were very close. Considering the computational costs and accuracy, the medium grid having 553632 cells was adopted for the simulations in this study.
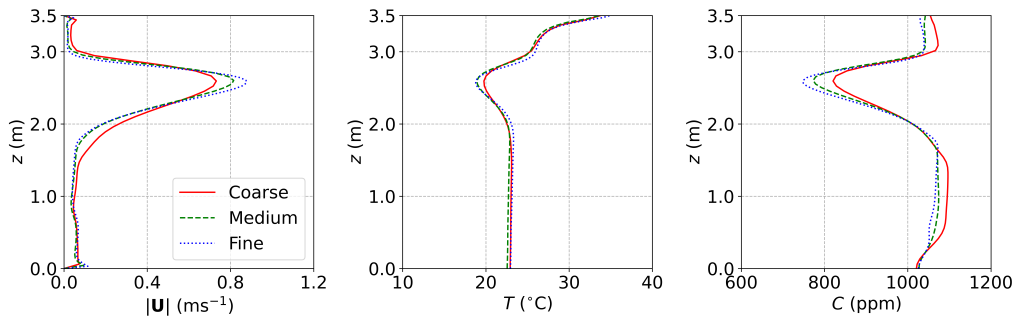

Fig. E.2 The results of grid convergence examination for the small office under MV (velocity, temperature and concentration profiles along sampling line 4 of Figure 4.1b). Red solid lines: coarse grid; green dashed lines: medium grid; blue dash-dotted lines: fine grid.

E.3   The office with DV and MV

For the office equipped with DV and MV [65], the grid convergence was examined using three grids having 964947 (coarse), 1965986 (medium), and 4571857 (fine) cube cells, respectively. The setups of MV were adopted. The results are shown in Figure E.3. It can be seen that the results of the medium grid and the fine grid were very close. Considering the computational costs and accuracy, the medium grid having 1965986 cells was adopted for the simulations in this study.
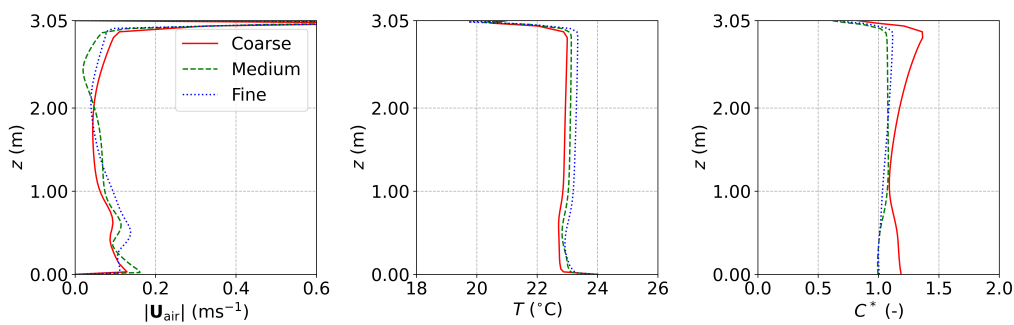

Fig. E.3 The results of grid convergence examination for the office under MV (velocity, temperature and concentration profiles along sampling line 6 of Figure 4.6b). Red solid lines: coarse grid; green dashed lines: medium grid; blue dash-dotted lines: fine grid.

E.4   The negative pressure isolation ward

For the negative pressure isolation ward equipped with MV [68], the grid convergence was examined using three grids having 627326 (coarse), 1143714 (medium), and 2280912 (fine) cube cells, respectively. The velocity profiles predicted using the three grids are shown in Figure E.4. It can be seen that the results of the medium grid and the fine grid along line 1 and line 2 of Figure 4.11b were very close. Considering the computational costs and accuracy, the medium grid having 1143714 cells was adopted for the simulations in this study.
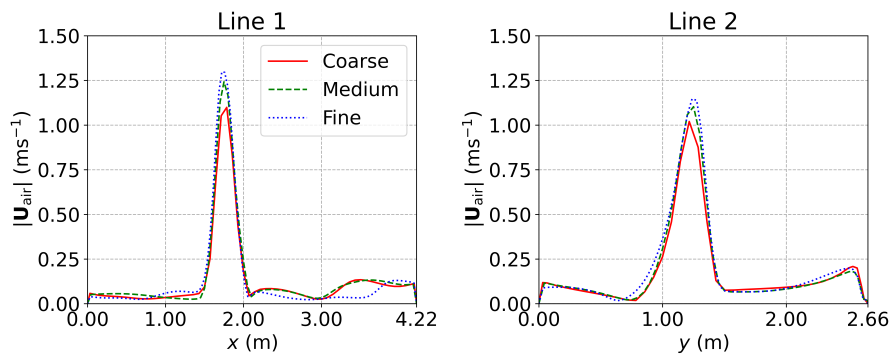
Fig. E.4 The results of grid convergence examination for the negative pressure isolation ward with MV. Red solid lines: coarse grid; green dashed lines: medium grid; blue dash-dotted lines: fine grid.